Modeling fluid flow in fault zones: two different-scale cases from Majella Mountain and East Pacific Rise

Dottorato di Ricerca in Scienze della Terra

XXX Ciclo

Candidato

Valentina Romano

ID number 1169355

Advisor

Sabina Bigi

Co-Advisors

Maurizio Battaglia

Patricia Gregg

Modeling fluid flow in fault zones: two different-scale cases from Majella Mountain and East Pacific Rise
PhD Thesis Sapienza – University of Rome

Author's email: valentina.romano@uniroma1.it

Acknowledgements

Well, I hardly know where to begin…

The past three years represented for me many things: hard work, exploration, adaptability, change. My PhD experience was unique, since I had the opportunity to work with incredible international scientists. A great part of my research was in fact conducted at the University of Illinois at Urbana-Champaign (UIUC), thanks to the great opportunity that Sapienza University of Rome gives to its students in terms of international mobility. I met amazing people from all over the World, in a constant cultural and personal enrichment, I dove to the bottom of the Pacific Ocean, I saw beautiful Midwestern sunsets and I lived so many new experiences I could have never imagined.

I want to thank you my advisors: Sabina Bigi, Maurizio Battaglia and Patricia Gregg for their incredible support and guidance in this professional and personal grow path. Your experience, patience, suggestions and moral encouragement made this dissertation possible.

I would like to acknowledge prof. Albert J. Valocchi from the Civil Engineering Department of UIUC and Jeffrey Hyman and Satish Karra from Los Alamos National Laboratory for their precious guidance and support in the numerical modeling of fluid flow in a fault zone.

I want to thank you my colleagues and friends in the Geology and Civil Engineering Departments for their precious help and discussions.

I want to thank my dad Nino and all my family, thank you for your immense love, that crossed oceans and lands to reach my heart, making me feel warm even at thousands of kilometers from home. I would not be the person I am without all of you.

Thank you, Riccardo, for sharing everyday with me all the chapters of this incredible journey. You lived my happiness, my bad moments, supporting me and always encouraging me in doing my best and believe in myself. You were totally part of this.

This page was intentionally left blank.

Abstract

A quantitative assessment of how rock discontinuities (i.e., fractures and faults) control the migration of geofluids is critical in several areas of geological and environmental sciences.

In this project I concentrated my attention to two problems at the extreme range of the spectrum of fluids properties, in two different geological settings: the flow of CO_2 from a natural reservoir and the melt migration in mid-ocean transform fracture zones.

The specific targets of my studies were:
-a fault zone exposed in the Roman Valley Quarry (Lettomanoppello, Italy);
-the fracture zone of the Siqueiros Transform Fault (East Pacific Rise);

The thesis is structured starting from a general overview of the two study cases and then describing in detail the methods used and the results achieved for each scenario.

To model the migration of CO_2 in a fault zone, I created a new pipeline that starts from the field data and then uses open source software and new developed codes to model the fluid flow in a fault zone considering all its components: core and damage zones.

I selected the Roman Valley Quarry as study site because of the great exposure of the inner structure of two oblique slip normal faults. Besides, the massive presence of fluid migration in the form of tar in the fracture systems makes this site a good natural analogue for studies of fluid flow in fractured media.

The work on the fault zone of Roman Valley Quarry can be divided in three main parts:

1. Collection of quantitative information on the fractures/fault distribution;
2. Application of state-of-art modelling techniques to infer the hydraulic properties of the fractured reservoir from field data;
3. Numerical modeling of flow of CO_2 in the fractured reservoir;

I modeled the data collected in the field to infer the hydraulic properties of the fractured reservoir (i.e. the Bolognano Formation). I employed a hybrid numerical technique, modeling

the damage zones as a fractured medium and the core as a continuum medium. This allowed me to:

1. characterize the hydraulic differences observed in the field between the southern part and the northern part of the fault;
2. characterize the hydraulic parameters of the footwall and hangingwall damage zones;
3. use these values to model the fluid flow in the whole fault zone, coupling damage zones and core.

I built Discrete Fracture Networks (DFN) models using both commercial (Move®) and open source software (*dfnWorks*, developed by Los Alamos National Laboratory). Move® has been used to model the hydraulic differences found in the field between the northern and southern sector of the fault. *dfnWorks* has been used to infer the hydraulic parameters of the fracture systems of the damage zones of the fault. These parameters have then been used to upscale the properties of the fractures to an equivalent continuum medium, in order to simulate the fluid flow in the entire fault zone, coupling the core and the damage zones.

The numerical model of CO_2 flow in the fault zone was developed using the open source software PFLOTRAN. To better reproduce a real-life case study, I simulated the injection of CO_2 into the footwall of the Roman Valley Quarry fault. Hydrostatic initial conditions have been imposed, according to the pressure distribution in the domain. An injection mass rate has been imposed at the location of the well to simulate the injection of CO_2. First, I run a number of simulations to test the workflow and verify the consistency of the numerical results. Once I obtained a stable numerical framework, I run several numerical experiments.

Results from numerical experiments show that the distribution of the CO_2 in the domain appears mainly controlled by the permeability distribution in the damage zone of the fault. The CO_2 in fact accumulates in the high permeability fault footwall, where the injection happens and reaches the maximum values of the pressure and saturation close to the core of the fault, that is characterized by a low permeability. Although developed and calibrated for the specific site of the Roman Valley Quarry fault, the methodology developed in this study can be extended to different geological contests.

Although not originally part of my PhD proposal, the involvement on the Off-Axis Seamounts Investigations at Siqueiros (OASIS) project was a unique opportunity to learn how to collect, process and employ geophysical data to characterize and model fluid flow (in this case, magmatic melts) near a fault zone.

The OASIS (Off-Axis Seamount Investigations at Siqueiros) expedition is a multidisciplinary effort to systematically investigate the 8˚20’N Seamount Chain to better understand the melting and transport processes in the southern portion of the 9˚-10˚N segment of the East Pacific Rise (EPR). The 8˚20’N Seamount Chain extends ~160 km west from its initiation, ~15km northwest of the EPR-Siqueiros ridge transform intersection (RTI). To investigate the emplacement of the 8˚20’N Seamounts, shipboard EM-122 multibeam, BGM-3 gravity, and towed magnetometer data were collected using the *R/V Atlantis* in November 2016. Multibeam data show that the seamount chain is characterized by the emplacement of discrete seamounts in the distal portion of the chain, while east of 105˚20’ W, the chain is a nearly-continuous volcanic ridge comprised of small cones and coalesced edifices with some evidence for rift zones, craters and calderas on the larger constructs. Isostatic anomalies, calculated along several profiles crossing the main edifices of the seamount chain, indicate that the seamounts formed within 100 km of the EPR ridge axis. Excess crustal thickness variations of 0.5 to 1 km, derived from the Residual Mantle Bouguer Anomaly, suggest an increase in melt flux eastward along the chain. Consistently high emplacement volumes are observed east of -105 ˚20’ W, ~130 km from the ridge axis corresponding with lithosphere younger than 2 Myr. Inverted three-dimensional magnetization data indicate that the seamounts have recorded a series of magnetic reversals along the chain, which correlate to reversals recorded in the surrounding seafloor upon which the seamounts were built. However, reversals along the eastern portion of the chain appear skewed to the west indicating that seamount formation is likely long-lived. The geophysical observations indicate that the overall seamount chain is age progressive, and suggest a coeval volcanism in a region 15-100km from the EPR. The seamounts do not follow absolute plate motions, but are located consistently 15-20 km north of the Siqueiros fracture zone, which further suggests that their formation is linked to the location and tectonic evolution of the Siqueiros-EPR ridge-transform intersection. These findings have implications for the location/origin of the melt region feeding the EPR as well as how melt is transported near a fracture zone. In fact, the seamounts chain does not follow an hotspot reference frame, but instead runs parallel to the fracture zone, at a constant distance. This observation is unusual, compared to the other seamounts in the region. Evidences of plate

direction rotation in variation of the main trend of the chain can be observed. They can be attributed to events of plate rotations that characterized the evolution of the Siqueiros Transform Fault as according to Pockanly et al., (1997): the seamount chain may have formed with the first event of plate reorganization from 3.5 Ma, with the inset of the volcanism close to the RTI. We could think about a melt migration model that takes into account the tectonic evolution of the area, pointing out the role of a stress concentration in the vicinity of the RTI as triggering mechanism for the volcanism.

Riassunto

La valutazione quantitativa di come discontinuita' quali fratture e faglie controllino la migrazione di geofluidi e' critica in diverse aree delle geoscienze.

In questo progetto di ricerca ho concentrato la mia attenzione su due problemi ai limiti estremi delle proprieta' dei fluidi ed in contesti geologici molto diversi: il flusso di CO_2 in una zona di faglia e la migrazione di magma in una zona di fratturazione di una faglia trasforme, lungo una dorsale oceanica.

Gli obiettivi specifici del mio studio sono stati:

-una zona di faglia esposta nella Cava della Valle Romana (Lettomanoppello, Italia);

-la zona di fratturazione della faglia trasforme di Siqueiros (East Pacific Rise);

La tesi e' strutturata partendo da una panoramica generale dei due casi di studio, passando poi alla descrizione di dettaglio dei metodi adottati e dei risulati raggiunti per ciascun scenario.

Per modellare la migrazione di CO_2 in una zona di faglia, ho creato un nuovo workflow, che partendo dai dati di campagna, utilizza software open source e nuovi codici per modellare la circolazione di fluidi in una zona di faglia, considerandone tutte le componenti: core e damage zones.

La Cava della Valle Romana e' stata selezionata come sito di studio per l'ottima esposizione della struttura interna di due zone di faglia normali oblique, nella Formazione Bolognano. Inoltre, la massiccia presenza di flusso di catrame nei sistemi di fratture rende questo sito un ottimo analogo per studi di flusso in mezzi fratturati.

Il lavoro sulla zona di faglia della Cava Romana può essere suddiviso in tre parti:

1. Raccolta di informazioni quantitative sulla distribuzione delle fratture/faglie;
2. Applicazione di tecniche di modellazione conosciute per caratterizzare le proprietà idrauliche dei sistemi di fratture
3. Modellazione numerica di flusso di CO_2 alla scala della faglia

Ho modellato i dati raccolti in campagna per poter caratterizzare le proprieta’ idrauliche del reservoir fratturato (Formazione Bolognano). Ho adottato tecniche ibride di modellazione numerica, modellando le damage zones della faglia come un mezzo discreto ed i cores come un continuo. Questo ha consentito di:

1. Caratterizzare le differenze idrauliche osservate in campagna tra il settore meridionale e quello settentrionale della faglia;
2. Caratterizzare i parametri idraulici delle damage zones di hangingwall e footwall della faglia;
3. Usare questi valori per modellare il flusso alla scala della faglia, accoppiando le damage zones ed il core.

Ho costruito dei modelli di tipo Discrete Fracture Networks (DFN) utilizzando sia il software commerciale Move, che un software open source chiamato *dfnWorks* e sviluppato dai Los Alamos National Laboratory (LANL). Il software Move e’ stato utilizzato per modellare le differenze in termini di proprieta’ idrauliche tra il settore meridionale e quello settentrionale della faglia, come riscontrato dalle osservazioni di campagna. *dfnWorks* e’ stato utilizzato per la caratterizzazione delle proprieta’ idrauliche dei sistemi di fratture delle damage zones della faglia. Questi parametri sono stati poi utilizzati per l’upscaling a continuo equivalente, allo scopo di modellare la circolazione di fluidi nell’intera zona di faglia, accoppiando il core e le damage zones. La modellazione numerica di flusso di CO_2 in zona di faglia e’ stata sviluppata con il sfotware open source PFLOTRAN. Per riprodurre reali scenari di studio, e’ stata simulata l’iniezione di CO_2 nel footwall della faglia della Cava della Valle Romana. Sono state applicate condizioni iniziali idrostatiche, secondo la distribuzione delle pressioni nel dominio. In corrispondenza del pozzo di iniezione e’ stato invece imposto un tasso di iniezione per la CO_2. Il primo passo e’ stato quello di testare la procedura e la robustezza del metodo. Una volta ottenuto un impianto numerico stabile, ho realizzato diverse simulazioni.

I risultati delle simulazioni numeriche mostrano come la distribuzione della CO_2 nel dominio appaia controllata dalla distribuzione delle permeabilita' nella damage zone della faglia. La CO_2 infatti tende ad accumularsi nel footwall della faglia, dove avviene l'iniezione, caratterizzato da un'alta permeabilita'. Qui vengono raggiunti i massimi valori di pressione e saturazione, in particolare nella zona in prossimita' del core della faglia, caratterizzato da bassi valori della permeabilita'. Sebbene sviluppata e calibrata per il sito specifico della Cava della Valle Romana, la metodologia sviluppata puo' essere estesa a differenti contesti geologici.

Anche se non originariamente parte del mio progetto di dottorato, il coinvogimento nel progetto Off-Axis Seamounts Investigations at Siqueiros (OASIS) ha rappresentato una occasione unica per poter imparare tecniche di raccolta, analisi ed utilizzo di dati geofisici al fine di modellare la circolazione di fluidi (in questo caso fusi magmatici) in prossimita' di una zona di faglia.

La spedizione OASIS (Off-Axis Seamounts Investigations at Siqueiros) fa parte di un progetto multidisciplinare per studiare la catena di seamount localizzata 8˚20'N e comprendere i processi di fusione e trasporto nella porzione meridionale del segmento 9˚-10˚N dell'East Pacific Rise (EPR). La catena di seamounts 8˚20'N si estende per circa 160 km dalla sua origine, circa 15 km a Nord-Ovest della zona di intersezione tra l'EPR e la faglia trasforme di Siqueiros. Per studiare le modalita' di messa in posto dei vulcani, sono stati acquisiti dati batimetrici, con il multibeam, EM-122, dati gravimetrici, con un gravimetro BGM-3 e dati magnetometrici a bordo della nave da ricerca *Atlantis*, nel Novembre 2016. I dati batimetrici mostrano come la catena di vulcani sia caratterizzata da edifici discreti nelle porzioni distali della catena, mentre ad est della longitudine 105˚20' W, questi presentano una morfologia simile a quella di una dorsale continua, formata da piccoli cono ed edifici coalescenti, con alcune evidenze di zone di dorsale, crateri e caldere sulle strutture maggiori.
Anomalie isostatiche, calcolate lungo diversi profili che attraversano gli edifici principali della catena, mostrano che i seamounts si sono formati entro 100 km circa dall'EPR. Variazioni nello spessore crostale da 0.5 km ad 1 km, ricavate dalle Anomalie di Bouguer Residue, indicano un incremento nel flusso di magma muovendosi verso Est lungo la catena. Parallelamente, la messa in posto di grossi volumi viene osservata ad est di -105 ˚20' W, ~130 km dall'asse della dorsale, corrispondente ad litosfera piu' giovane di 2 Ma. L'inversione di dati magnetometrici

indica come i seamounts abbiano registrato una serie di inversioni magnetiche, che trovano correlazione con le inversioni del fondale oceanico su cui si trovano. Tuttavia, le inversioni nella porzione orientale della catena appaiono distorte, indicando che probabilmente la formazione dei seamounts sia durevole. Le osservazioni geofisiche indicano che nel complesso la catena di vulcani mostra una progressione in tempo, con vulcanismo coevo nella regione compresa tra 15 e 100 km dall'EPR.

I vulcani non seguono un sistema di riferimento assoluto, ma sono localizzate a circa 15-20 km dalla zona di fratturazione della Trasforme di Siqueiros, il che suggerisce ulteriormente come la loro formazione sia legata alla localizzazione ed evoluzione tettonica dell'intersezione tra la Trasforme di Siqueiros e l'EPR.

Queste scoperte hanno profonde implicazioni sulla localizzazione ed origine del magma che alimenta l'EPR, cosi come sulle modalita' di trasporto del magma nei pressi di una zona di fratturazione. Infatti, la catena di vulcani non segue un sistema di riferimento di un punto caldo, ma invece corre parallelamente alla zona di fratturazione, ad una distanza costante. Questa osservazione e'piuttosto inusuale, se confrontata con altri seamounts che caratterizzano l'area. Variazioni della direzione principale lungo la catena sono correlabili con rotazioni della direzione della placca Pacifica. Infatti, secondo Pockanly et al., (1997), rotazioni di placca hanno caratterizzato l'evoluzione della Faglia Trasforme di Siqueiros: la catena di seamounts potrebbe essersi formata durante il primo evento di riorganizzazione delle placche, avvenuto circa 3.5 Ma fa, con l'instaurarsi del vulcanismo vicino alla intersezione faglia-dorsale.

Si puo' ipotizzare un modello di migrazione di magma che consideri l'evoluzione tettonica dell'area, mettendo in risalto come uno dei meccansimi di innesco del vucanismo possa essere la concentrazione dello stress intorno alla zona di intersezione faglia-dorsale.

Table of Contents

1.INTRODUCTION

1.1 Research activity

The rock masses in the Earth's crust consist of two major components: the intact rock matrix and discontinuities. These discontinuities may include faults, joints, dykes, fracture zones, bedding planes and other types of weakness surfaces or interfaces that can have a significant effect on the strength, deformability, and permeability of fractured rocks quantitative assessment of how rock discontinuities (i.e., fractures and faults) control the migration of geofluids is critical in several areas of geological and environmental sciences. I want to introduce the topics developed during my PhD thesis using the title of a work of 1986 by Herbert E. Huppert: "The intrusion of fluid mechanics into geology". In the last decades in fact there have been major development in the application of fluid mechanics into geological sciences, spanning from Hydrogeology to Volcanology, Geophysics and Geodynamics. All these applications depend mainly on the physical properties of the fluid and the geological context under consideration.

In this project I concentrated my attention to two problems at the extreme range of the spectrum of fluids properties, in two different geological settings: the flow of CO_2 from a natural reservoir and melt migration in mid-ocean transform fracture zones.

The specific targets of my studies were:
-a fault zone exposed in the Roman Valley Quarry (Lettomanoppello, Italy);
-the fracture zone of the Siqueiros Transform Fault (east Pacific Rise);

My research activity was strongly influenced by the work made at the University of Illinois at Urbana-Champaign (UIUC), where I spent 18 months as visiting scholar, from January 2016 to June 2017. My time at UIUC was split between the Department of Civil and Environmental Engineering, under the supervision of prof. Albert J. Valocchi and the Department of Geology, under the supervision of prof. Patricia Gregg.

With Prof. Valocchi's group I worked on the numerical model of fluid flow in a fault zone. My work was applied to the fault zone of the Bolognano Formation exposed in the Roman Valley Quarry, in the town of Lettomanoppello (PE), Majella Mountain. This fault zone represents a good natural analogue to study the flow of fluids in a fault, because of the massive presence of tar migrating in the fracture systems. The aim was to create a suitable pipeline applicable to different geological contexts through the appropriate calibration of the geometric and petrophysics parameters of fractures and host rock. I also collaborated with the group of Computational Earth Science at Los Alamos National Laboratories (LANL), authors of the software *dfnWorks* that I used to perform the simulations. I went to LANL twice for the setup of the model and to test all the workflow, fusing the field data and the conceptual model of the fault developed during the first year.

With Prof. Gregg's group I had the opportunity to work on the Off-Axis Seamount Investigations at Siqueiros (OASIS) project, whose aim is to investigate a chain of seamounts located 8˚20'N, along the fracture zone of the Siqueiros Fracture Zone, East Pacific Rise (EPR). I worked on the conceptual model of melt migration and extraction along the fracture zone, in order to understand a possible mechanism for the formation of the seamount chain. In November 2016 I took part to a 30 days expedition on board of the *R/V* Atlantis, to collect bathymetric, gravimetric, magnetic and samples along the 8˚20'N seamount chain. After the cruise I performed the analysis of the geophysical data, in order to constrain the timing of formation of the seamounts, critical information to model how melt is transported in the vicinity of a fracture zone. The results of these analyses will be submitted to an important scientific journal in the next months, (Romano et al., 2017, in prep). Although the involvement on the OASIS project was not originally part of my PhD proposal, it gave me a unique opportunity to learn how to collect, process and employ geophysical data to characterize and model fluid flow (in this case, magmatic melts) near a fault zone.

1.2 Modeling of the fluid flow of CO_2 in a fault zone.

Research conducted over the last 20 years indicates that geological storage of anthropogenic CO_2, together with other approaches, can significantly contribute to the reduction of this gas concentration in the atmosphere (up to 14% according to IPCC, 2005 and IPCC, 2007). In a geological CO_2 storage site, the main migration pathways in case of leakage would be compromised boreholes or gas permeable faults or fractures. Faults comprise zones of crushed, sheared, and fractured rock that can influence the storage capacity of a reservoir. The way faults impact on fluid flow depends on multiple factors, including permeability and relative permeability of fault rocks and the rock hosting the fault, the pressure and temperature conditions of the reservoir and fluids, the composition of the fluid and the fracture geometry. These parameters and the resulting fluid flow rates may change between faults or along the same fault, as well as from one CO_2 storage site to another, promoting and or retarding fluid flow (Nicol et al., 2017). A detailed understanding of gas migration in fault systems is one of the fundamental steps to select the best possible location for CO_2 storage (Rutqvist, Birkholzer, Cappa, & Tsang, 2007; Annunziatellis et al., 2008)

The integration of field data and numerical modeling was the focus of a growing attention in the past years, because of the strong potential to combine detailed observations of the investigated system, in this case a fault zone, with the power of the numerical simulation (Gilmour et al.,1986; Walsh et al., 2003; Caine et al., 1996; Bigi et al., 2013; Panza et al., 2017), providing a more accurate, better constrained, quantitative model.

1.2.1 Hydraulics of fractured media

Rocks have two major components: the intact rock matrix and discontinuities. Discontinuities, at different scales, include fault zones, joints, dykes, fracture zones, bedding planes and other types of weakness surfaces or interfaces. Geological structures, such as faults, dykes or fracture zones may extend from tens to hundreds of meters to tens or hundreds of kilometers. The discontinuities at microscopic scale are distributed more randomly in rock matrices. The discontinuities whose dimensions lie between the above two extreme cases are usually joints, bedding planes or, foliations, and usually range from centimeters to tens of meters. These discontinuities are often characterized by a clustered orientation and are organized in sets, cutting the rock masses into blocks of complicated shapes. The presence of these discontinuities makes the rock masses largely discontinuous, inhomogeneous, anisotropic and non-elastic (DIANE; Hudson and Harrison, 2005) and has a significant effect on the strength, deformability and permeability. Rock discontinuities can act as hydraulic conductors, providing either pathways for fluid flow or barriers that prevent flow across them.

Over the last few decades, a number of studies have focused on the role of discontinuities (i.e., fractures and faults) in fluid migration, as well as entrapment (Nelson, 2001; Chester & Logan, 1986; Aydin & Schultz, 1990; McGrath & Davison, 1995; Caine et al., 1996; Childs et al., 1996; Peacock, 2002; Walsh et al., 2003; Faulkner et al., 2011; Gudmundsson et al., 2010 and references therein, Smith et al., 2013). Understanding the impact of these structures on fluid flow and storage is tricky, due to their complexity, since each structure has its own geometry, spacing, distribution, connectivity, and hydraulic properties.

According to Caine et al., (1996) the primary architecture of brittle fault zones in low porosity rocks, is composed by: fault core, damage zone and host rock (Figure 1). The fault core is the structural, lithologic and morphologic portion of a fault zone where most of the displacement is accommodated. The fault core is the result of highly localized strain and intense shearing that accommodates most of the displacement within the fault zone, and generally consists of a number of recurring slip surfaces and fault rocks such as gouges, cataclasites, and breccias (Sibson, 1977; Bruhn et al., 1994; Cello et al., 2001; Childs et al., 1996; Billi et al., 2003; Agosta, 2008; Wibberley et al., 2008; Bastesen and Braathen, 2010). Grain size reduction and/or mineral precipitation usually make the fault core a low porosity and low permeability zone compared to the host rock. The damage zones bound the fault core and present relatively low strain and deformation compared to the core. A network of subsidiary structures characterizes the damage zone, (e.g. small faults, veins, fractures, cleavages, and folds), that cause a strong heterogeneity and anisotropy in the rock mass (Caine et al., 1996), usually enhancing its permeability. The fault core and damage zones are surrounded by wall rock, containing background deformation and without fault-related permeability structures: the hydraulic and mechanic parameters reflect those of the intact host rock. The distribution of core and damage zone is the primary control on a fault barrier-conduit behavior. Faults are dynamic systems. Because mechanical, geochemical and hydrologic properties vary with such factors as lithology, temperature, pressure and deformation rate, the effect of a given fault on fluid flow can vary in both space and time (Sibson, 1990; Knipe et al., 1998). Caine et al. (1996), recognize four end member architectural styles in an outcrop, associated with a characteristic permeability structure: localized conduits, distributed conduits, localized barriers, and combined conduit-barriers (Figure 1).

These end members represent individual faults or a sequence in the evolution of a single fault with increasing displacement.

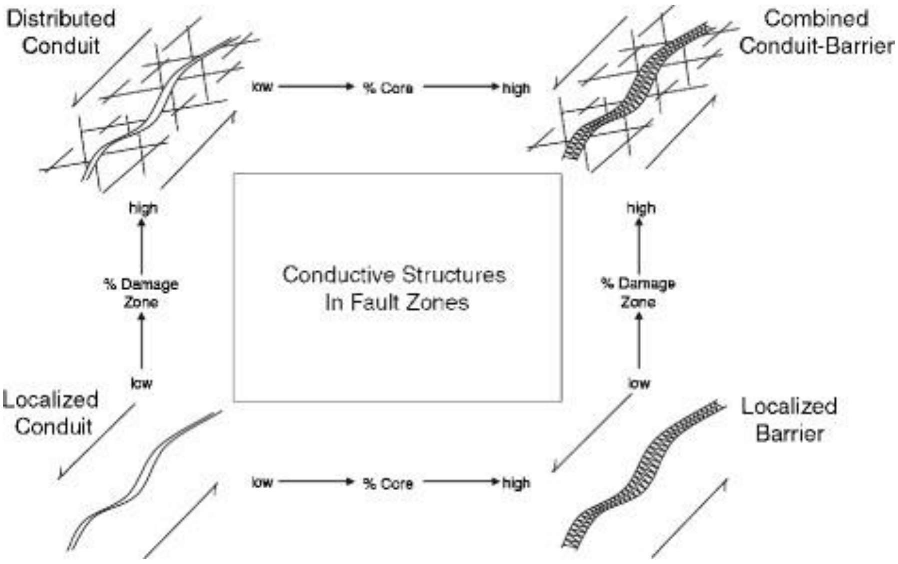

Figure 1. Conceptual model for fault-related fluid flow (modified after Caine et al., 1996).

(Aydin, 2000) proposed a classification of fractures/fault systems based on the mode of formation, finding three main classes: dilatant-mode (fractures/joints, veins, dikes), contraction/compaction-mode (fracture/pressure solution seams and compaction bands), shear-mode (fractures/faults). Important differences exist from one type to another in terms of geometry, distribution, and flow properties. All these structural elements may have different effects on subsurface flow. Joints, as opening mode fractures (Pollard & Aydin, 1988), form conduit for fluid flow. On the contrary, pressure solution seams (Fletcher and Pollard, 1981), as closing-mode fractures, contain impermeable clay reach material acting as a barrier to fluid flow, but they may channel fluids when sheared (Graham Wall et al., 2006). Compaction bands are characterized by lower values of porosity with respect to the surrounding porous host rock, acting usually as barrier to fluids (Tondi et al., 2006). Shear bands can act as barrier or conduits depending on their mechanical processes (Aydin et al., 2006). Faults have complex architectures that may enhance and/or contrast fluid migration with four possible behaviors: transmitting faults, sealing faults, vertically transmitting and laterally sealing faults, faults sealing or transmitting intermittently.

Figure 2 shows an idealized fault architecture with the corresponding permeability structure, showing the control exerted by the density of the deformation bands: *kf* is the permeability of the rock, *kr* is the permeability of the wall rock of the slip plane, *kd* is the permeability of the deformation bands, T is the thickness of the block, t is the thickness of the fault core and d is the total thickness of the damage zone (see also Antonellini & Aydin, (1994) for details).

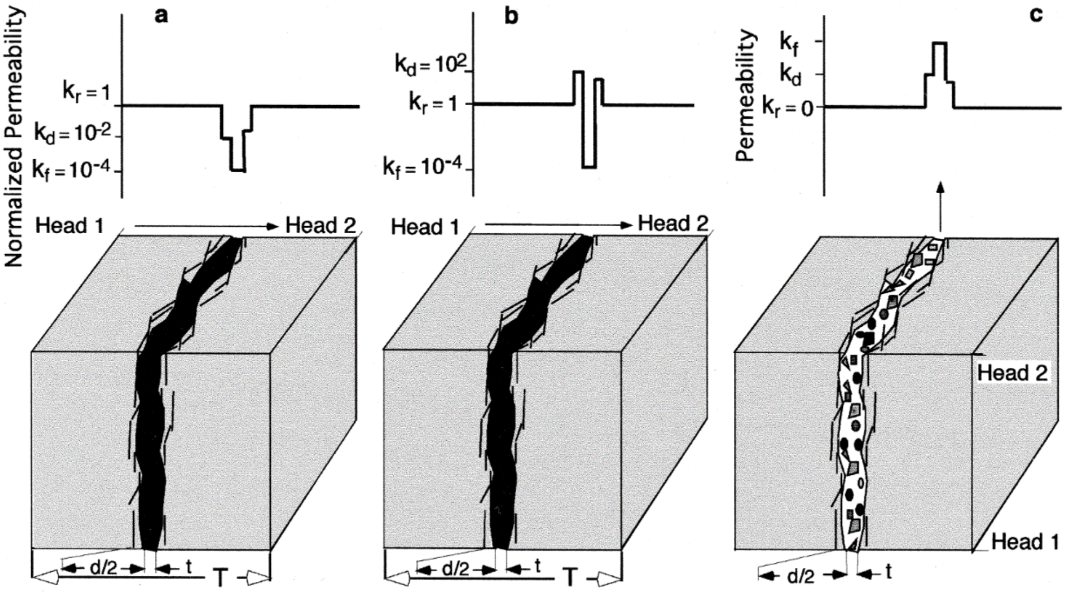

Figure 2. (a) A deformation-band fault zone with reduced permeability (k_f), normalized to that of the host rock, in a direction perpendicular to the fault. (b) A fault developed by shearing across a joint zone. Fault rock formed by this process is similar to that of the deformation band but it is surrounded by a damage zone, more permeable than the parent rock. (c) A brecciated fault zone filled with hydrocarbon. The permeability (k_f) depends on the porosity of the zone and the ratio of the fault thickness to particle radius. (from Aydin, 2000).

Fault zone permeability is controlled by many interdependent factors including among others: fault architecture and the types of rocks present in a given location, mechanical strength and permeability of the host rock lithology, fracture aperture size and connectivity, fluid composition pressure and gradients, extent of preexisting mineralization and the orientation and magnitude of normal and shear stress (IEAGHG report 2016).

The characterization of faults/fractures involves the answer to the following three key questions:

1. How can they be identified, located and characterized?
2. How do flow and transport occur in these systems?
3. How can we forecast their hydraulic behavior?

There are different methods for locating and characterize fault/fracture through a combination of geological mapping (outcrop or borehole data), geomechanical analysis and geophysical and hydrogeological measurements. Starting from the collection and interpretation of field data, it is possible to construct a conceptual model for fluid migration that describes the main hydro-geological features controlling the flow and transport behavior of interest. The conceptual model is a schematization of the real system that is the basis for the mathematical calculations. The level of detail of a conceptual model varies with the purpose for which the model was developed, for example for fluid flow or solute transport; the latter case would require a refined level of detail, because of the high sensitivity to small scale fracture heterogeneities.

The typical conceptual model of fault zones, with core and damage zones, has provided the framework for laboratory measurements and numerical modeling. Rocks from the core are typically characterized by two types of gouge: granular materials composed of broken, irregular clasts and gouges that contain some portion of phyllosilicate material. Fault zones rich in phyllosilicates material, tend to have lower permeabilities than quartz and/or framework silicate-rich gouges. In evaluating the sealing potential of a fault, analysis of reservoir/carrier beds against other reservoir beds is critical. In the oil industry, faults which are three-dimensional volumes, are approximated in modelling applications as planar membranes onto which predictions of the most important fault-related flow properties are mapped. These methods involve the construction of fault surface projection maps (or Allan Diagrams; (Downey, 1984; Allan, 1989) for each fault of interest. Allan diagrams illustrate simultaneously the stratigraphy on both sides of a fault and therefore highlight potential juxtaposition seals and cross-fault flow paths. However, faults are not single surfaces, but often comprise multiple slip surfaces. As described in Manzocchi et al., (2010), flow modelling in the oil industry is typically concerned with volumes on the oil-field to basin scales, and it is not possible to explicitly represent all of the internal complexity of fault zones in models at this scale. Instead, the approach must be to represent those aspects of a fault which are thought to be critical to determining flow and which can be represented in a model at the scale of interest. It is therefore necessary to define fault proxy-properties which are based on simplified conceptual models of a fault zone that can be used to infer the distribution of relevant physical properties and can be calculated as continuously varying fields on the Allan diagrams. The most commonly applied proxy-property is the Shale Gouge Ratio (SGR; Yielding et al., 1997), a ratio or percentage of shale in a silicilastic fault zone, which simply assumes that any one point on the fault has a composition identical to the average composition of the sequence past which that point has slipped. The correlation between capillary threshold pressure and the clay content of laboratory samples (e.g. Fisher and Knipe, 1998; Childs et al., 2002; Sperrevik et al., 2002), coupled with the assumption that SGR is a good proxy for clay content in fault rock, provides the basis for the most commonly applied fault seal prediction methods (e.g. Yielding et al.1997; Rutqvist et al., 2007, Jeanne, et al., 2014; Niu et al., 2017).

Compared to core, the permeability of fault damage zones is governed by the host rock permeability and the presence of both macro-scale high permeability fracture networks and low permeability deformation and compaction bands. Both fractures and deformation bands have been shown to decrease in frequency with increasing distance from the fault core. The permeability of the host rock within the damage zone is controlled by the frequency and orientation of the fractures.

There are several numerical approaches that can be used in the modeling of fractured systems, as described in the next part, taken from (Painter et al., 2012). Flow and transport in fractured rocks is not adequately described by uniform or non-uniform isotropic continuum representations (Neuman, 2005) and alternative methods to classical continuum representation have been developed. These alternative approaches can be grouped into three general classes: discrete fracture network representations, complex continua representations and hybrid representations. Discrete Fracture network (DFN) models describe the rock mass as an interconnected network of explicitly represented fractures. Networks of fractures are stochastically generated using a stochastic model derived from site data. A computational mesh is placed on each fracture plane usually ensuring that the mesh on each of a pair of intersecting fractures matches along the intersection. Groundwater flow equations are then solved using this computational mesh. Complex continua representations generalize a simple effective continuum representation to account for various flow and transport phenomena. Dual continuum models (Barenblatt et al., 1960; Warren & Root, 1963) represent fractured porous rock as two overlapping and interacting continua. In its most general form (e.g. Duguid & Lee, 1977), known as the dual permeability model, flow and transport takes place in both the fracture and matrix continua while accounting for fluid and solute migration between the two continua in response to pressure and concentration differences. Commonly, flow in the matrix system is neglected relative to flow in the fracture system. In this case, the matrix acts as a non-conductive reservoir for fluid and/or solute storage and the fracture system provides the fluid migration pathways. In this variant, usually referred to as the dual porosity model, fluid and solute flux are proportional to the pressure and concentration differences between the two continua at a given location and time. The dual continuum class of models has also been generalized (Pruess & Narasimhan, 1985; Zyvoloski et al., 2008) to better represent gradients internal to the matrix blocks. Regardless of how the matrix/fracture interactions are represented, multiple continuum models originally conceptualized the fracture flow system as having a representative elementary volume (REV) that establishes a spatial scale above which the flow properties become approximately independent of scale. For natural fracture patterns, which often have a broad distribution of fracture lengths, the existence of a classical REV scale may be questionable. Neuman proposed a stochastic continuum approach that does not require an REV (Neuman 1987, 2005). In his approach, an effective permeability tensor and other required flow/transport properties are assigned to each grid block in a conventional continuum conceptualization. However, the properties vary from grid cell to grid cell according to a stochastic model. Moreover, the stochastic model is dependent on the size of the grid block. Thus, a different stochastic model is required if the spatial discretization is changed. The stochastic continuum model may be combined with any of the dual or multiple continua ideas to represent fracture/matrix interactions.

Hybrid methods use DFN models but also continuum representations for practical computational reasons (e.g. to reduce the overall size of the computational mesh). Hybrid methods fall into two subclasses: nested and upscaled. In nested models, explicit DFN models are used along transport pathways or in other regions where high spatial resolution is required and continuum representations are used in regions that are of less interest. This approach allows for a DFN representation of transport in and near expected transport pathways while still modeling a sufficiently large region to honor natural hydraulic boundary conditions. In upscaled models, explicit DFN representations are constructed and stochastically generated. However, the flow problem is not solved on the full DFN. Instead, the DFN is used to establish, grid block by grid block, equivalent permeability tensors for use in a continuum model. Jackson et al., (2000), Svensson, (2001) and Botros et al. (2008) provide examples of upscaling algorithms for the permeability tensors.

As described in Faulkner et al. (2010), very few studies have measured bulk fault zone permeability directly using boreholes. However, many secondary data sources allow estimation of along-fault permeability. Talwani et al. (1999) estimated the permeability of a shallow fault zone using sinusoidal pressure oscillations in boreholes from lake level fluctuations. Their analysis shows fault zone permeability, in faults that are subject to reservoir-induced seismicity, are between 1.1×10^{-15} and 1.78×10^{-15} m^2. Tadokoro et al., (2001) estimated along-strike fault (damage) zone permeabilities around $1–10 \times 10^{-15}$ m^2 from the migration rates of induced seismicity during borehole injection experiments in the Nojima fault zone following the Kobe 1995 earthquake. At deeper levels, Shapiro et al., 1997 found crustal permeability to be $\sim 10^{-16}$ m^2 in the KTB borehole in the depth interval 7.5–9 km. A compilation of fault zone permeabilities derived from reservoir-induced seismicity data can be found in Talwani et al., (2007) Using the same techniques of migrating patterns of seismicity, but at deeper levels in the brittle crust, Miller et al., (2004) estimated fault zone permeability to be 4×10^{-11} m^2 immediately following the M6 Colfiorito earthquake sequence of 1997 in central Italy. Noir et al., (1997) inferred a higher fault zone permeability of 10^{-8} m^2 for the Dobi earthquake sequence in Afar in 1989.

Estimates of the bulk fault zone permeability are mostly derived from numerical models that simulate flow through the fault zone (Brown & Bruhn, 1998; Jourde et al., 2002; Matthäi & Belayneh, 2004; Odlin et al., 2004; Lunn et al., 2008). Detailed field measurements provide fine-scale descriptions of the fault zone (Jourde et al., 2002). Due to the limitations on the number of grid cells that can be included in reservoir-scale flow models, major faults are often either represented by zones only one cell thick or incorporated in the properties of the boundary between two cells. In these models, the bulk, or up-scaled, hydraulic properties of the fault and its damage zone are required. Some type of averaging or upscaling procedure is thus required before these fine scale fault zone characterizations can be used for large scale modeling. Upscaling is required whenever permeability data measured at one scale are to be used in analyses conducted over much larger scales.

The limitations in the resolution of seismic data remain such that, although major faults are detected, there is little or no information on the nature of their damage zones. Thus, one of the main methods of investigating the hydraulic properties of major fault damage zones is through the study of field analogues and the use of flow simulations in which models of the fault damage zone architecture are included explicitly.

The approach used in the present study integrates:

(a) geological field works;

(b) quantitative analysis of the distribution of the tectonic structures influencing the fluid flow, like faults/fractures;

(c) numerical modeling;

The study targets on a fault zone exposed in the Roman Valley Quarry (Majella Mountain, Italy), cutting the carbonatic Bolognano Formation, considered a natural analogue for fractured geofluid reservoirs. Worldwide, more than 50% of the natural reservoir (i.e., mineral and hydrothermal waters, geothermal fluids, oil, and gas and for storage purposes), consists of carbonate rocks (Schlumberger Ltd., 2007). Studies of fault zones in carbonate rocks have historically lagged those in cataclastic rocks. However, over the last decade, many more investigations of fault zones and fluid flow in carbonates have emerged e.g. (Agosta et al., 2010; Kim et al., 2010; Antonellini et al., 2014).

I used fine-scale information derived from field investigations to characterize the fluid flow of CO_2 in the bulk fault zone to study the its behavior to the potential injection of CO_2. The conceptual model was based on a fault damage zone considered a discrete medium and a core considered a continuum medium. Both DFN methods and hybrid techniques were employed, using commercial software (Move®) and open source softwares (*dfnWorks*, PFLOTRAN). Move® was used to model the hydraulic differences found in the field between the northern and southern sector of the fault. *dfnWorks* was used to infer the hydraulic parameters of the fracture systems of the damage zones of the fault. These parameters were then used to upscale the properties of the fractures to an equivalent continuum medium, in order to simulate the fluid flow in the entire fault zone, coupling the core and the damage zones. The injection of a multiphase fluid (CO_2+water) was simulated in the footwall of the fault, using PFLOTRAN.

Depending on the aim of the model, previous works on multiphase fluid flow simulation in fault zones, treated the fault as planar objects imbedded in a three dimensional space (Jha and Juanes, 2014), as impermeable elements imposing no flux boundary conditions at the fault location (Orsini et al., 2014), as objects with different thicknesses and properties, without distinguish the core and the damage zone (e.g. Rutqvist et al., 2007; Cappa & Rutqvist, 2011), as simplified one dimensional Pruess & García, (2002) or two dimensional problems (Keating et al., 2014; Lu et al., 2012) considering the fault with a constant permeability.

This study lies in the context of dimensional numerical modeling of fluid flow in fault zone in carbonate rocks, providing a new methodology to characterize the hydraulic behavior of a fault in all its components. The advantage was the use of open source software, both for the DFN modeling of the damage zones and the flow simulation in the equivalent continuum, with a wide control on the input parameters and flow conditions. The model besides, is three dimensional, providing a more complex scenario to study the contribution to the migration of CO_2 of all the components of a fault zone, using the DFN to appropriately characterize the hydraulic properties of the fracture network of the damage zones and then reducing the geometric complexity of flow patterns in fractured rock mass to a continuum domain, easier to implement from a mathematical point of view at the scale of the fault.

Although applied to carbonate rocks, the proposed methodology can be extended to other geological scenario, by the appropriate calibration of the geometric and petrophysics parameters of fractures and host rock, to understand the conditions under which faults promote fluid flow from a reservoir and mitigate the risk of CO_2 migration via faults.

1.3 Melt migration

Mid Ocean Ridges (MOR) form along divergent plate margins and can be considered a manifestation of mantle dynamics, providing a window to study Earth's interior processes. MOR extend for more than 50,000 km across the ocean floor and can be divided into four categories of MOR, according to their spreading rate: fast-, intermediate-, slow- and ultraslow-Plate divergence at MOR drives mantle flow, mantle melting and the formation of new oceanic crust at a rate of ~3.3 km^2yr^{-1} (Parsons, 1981; White, 1992). The oceanic crust covers about two-thirds of the surface of the planet, releasing approximately 75% of the total heat flux from the interior of the Earth (ca. 32 of 43 TW). Crustal thickness is one of the most important features, providing the strongest constraints on melt generation and extraction (Forsyth, 1992; Bai et al., 2017). Gregg et al., (2007) found a correlation between the gravity signatures at transform faults and the spreading rates of the associated ridges, showing how crustal thickness variations between ridges and transform faults are spreading-rate dependent. In fact, at intermediate and fast-spreading ridges, the transform faults are associated with thicker crust with a negative residual mantle Bouguer anomaly signature along the transform faults, while at slow-spreading ridges, transform faults are associated to thinner crust. The thickness of the lithosphere, often approximated as depth corresponding to 600 °C isotherm, increases progressively from the ridge axis toward off-axis regions. The more the crust is far from the ridge the colder and the older it is, according to the half-space cooling model (Turcotte & Schubert, 2000). MOR are not continuous features, but are offset at nearly right angles by numerous transform faults, 50 km to 350 km long, that constitute plate boundaries (Menard, 1967; Menard & Fisher, 1958). At each end of the transform there are two aseismic limbs, called fracture zones, extending hundreds of kilometers, that represent the fossil trace of the fault; they are not plate boundaries, since both sides belong to the same plate (Figure 3). Near the transform faults and their fracture zones systematic changes in seafloor depth, crustal structure and crustal geochemistry are observed: thus indicating that transform faults strongly influence the thermal structure, mantle flow, melting and crystallization at mid ocean ridges (Fox, P.J., and Gallo, 1984; Morgan and Forsyth, 1988; Parmentier and Forsyth, 1985, Lin et al. 1990; Kuo and Forsyth, 1988; Tolstoy et al. 1993; Gregg et al. 2007; Gregg et al. 2012).

Beneath the mid ocean ridges, magma is produced over a volume of mantle that can extend to more than 100 km on either side of the ridge axis (Prince and Forsyth, 1988). Over the past decades, numerous geological, geophysical, and geochemical studies provided new constraints between mantle/melt dynamics and observed features like seafloor bathymetry, crustal thickness and basalt geochemistry (Macdonald et al., 1992; Mckenzie, 1984; Klein & Langmuir, 1987; White et al., 1992; Melt Seismic Team, 1998; Gregg et al., 2012; (Gale et al., 2013; Carbotte et al., 2016).

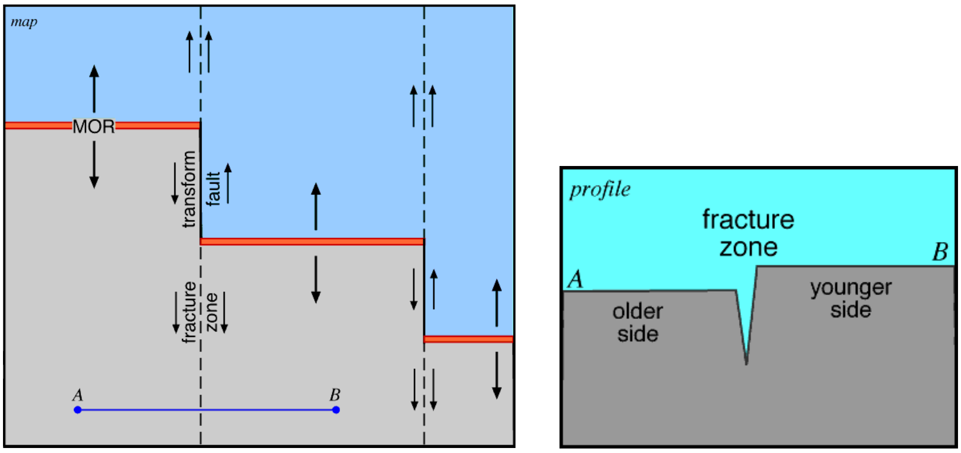

Figure 3. Left: MOR dissected by transform faults. Fracture zones exist as bathymetric features extending many hundreds of kilometers from the MOR. Right: section of the seafloor along the profile in the left figure. Because of the offset of the midocean ridge spreading centers, the crust on one side of a fracture zone will be older and therefore colder, more contracted, and deeper than the crust on the other side. The boundary between them is often a deep canyon. These are places where deeper levels of the oceanic crust are exposed.

The process of melt generation and extraction at mid ocean ridges has been a subject of considerable research over the past decades and it is usually explained on a plate scale as a three steps process: (a) melting starts where the mantle reaches its pressure-dependent solidus temperature owing to the adiabatic decompression; (b) the formed melts travels through the mantle (most through channelized flow) and then (c) focus toward the ridge axis (Gregg et al. 2012; Hebert & Montési, 2011; Hebert & Montesi, 2010). The extension of the region of partial melting underneath MOR varies according to the spreading rate, controlling crustal thickness variations, spreading centers morphology and major elelemnt compositions. At fast spreading ridges, such as the southern East Pacific Rise, the melt region is potentially hundreds of kilometers wide and approximately 100 km deep (MELT Seismic Team, 1998) with a high extent of melting. At very slow spreading ridges, the melt region may be 20 times narrower (Montési & Behn, 2007) with lower extent of melting. Despite the width of the partial melting region, neo-volcanic activity at surface is confined within a narrow zone (<2km, Macdonald et al., 1982; Standish & Sims, 2010). Several mechanisms have been proposed to explain the focusing of the melts toward the ridge axis, over distances up to hundreds of kilometers. They include the formation of a permeability barrier along the base of the sloping thermal boundary layer (Hebert and Montési, 2011; Sparks and Parmentier, 1991; Spiegelman, 1993; Sparks & Parmentier, 1993;(Magde, L.S., 1997) Magde et al., 1997), focusing as a result of anisotropic permeability (Phipps Morgan et al. 1987; Daines and Kohlstedt, 1997; Katz et al. 2006) and pressure effects caused by mantle corner flow (Phipps Morgan et al. 1987; Spiegelman and McKenzie, 1987). In permeability barrier models, the partial crystallization of melt rising into the lithosphere on either side of a ridge may create a barrier that impedes vertical melt flow. The melts will migrate toward the ridge axis along this barrier at the base of the thermal lithosphere, following a high porosity channel. The channel may generate self-consistently (e.g. Katz, 2010) or may follow an approximate parametrization (Hebert and Montesi, 2010). The melts are then extracted inside a so-called Melt Extraction Zone (MEZ), whose depth is poorly constrained, through structural features intersecting the permeability barrier. The MEZ may be present at both ridge and transform segments of oceanic spreading centers (Herbert and Montesì, 2011). As described in Gregg et al., (2012), there is a critical issue in geodynamics because of the non-uniqueness of the set of parameters fitting a given solution. Mantle potential temperature, melt migration pathways, variations in mantle source composition can all affect the predicted model output. Therefore, constraining geodynamic models with compositional petrologic models significantly limits the range of model parameters that can reproduce all physical observations (Cordery & Morgan, 1993; Cordery & Morgan, 1992; Shen & Forsyth, 1995; Gregg et al., 2009). For example, variations in the observed FeO, MgO and Na_2O content along with geophysical observations (e.g. crustal thickness variation) provide important constraints on geodynamic models. Shaw et al., 2010) combined geodynamic models with petrologic models to test the melt region and melt focusing for the ultraslow spreading Gakkel Ridge. They started from a passive flow thermal structure for an ultraslow spreading ridge, with full spreading rate 10 mm yr^{-1}, with a temperature-dependent visco-plastic rheology and stress-dependent viscosity, assuming a mantle potential temperature of 1350 °C. Melting is calculated from the resulting thermal structure using the model of (Kinzler & Grove, 1992a, Kinzler & Grove, 1992b), (Figure 4).

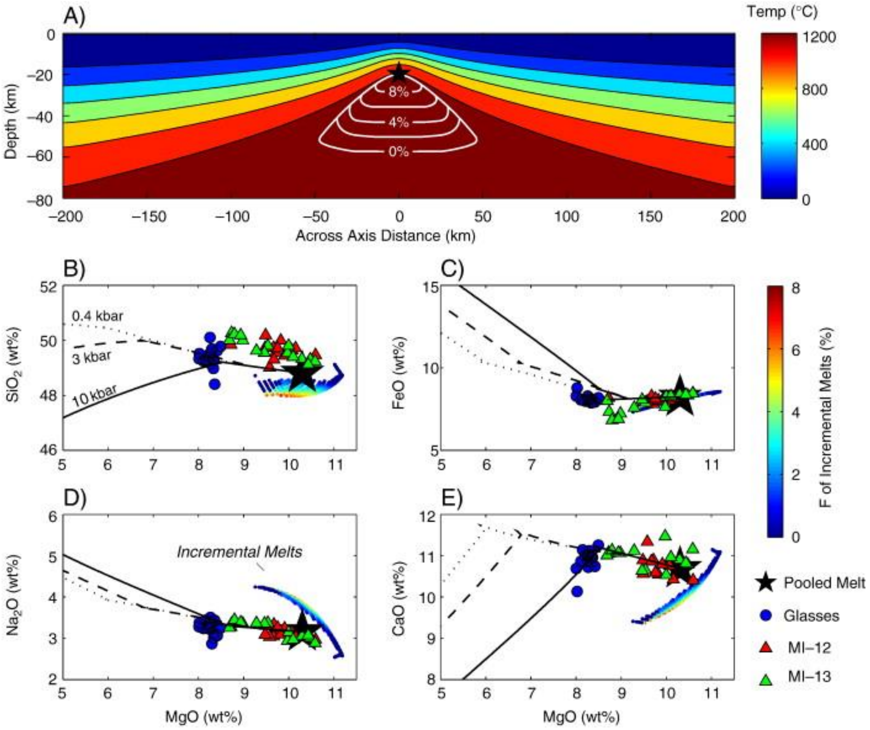

Figure 4. A) Passive mantle flow thermal structure. White lines denote melt region calculated from resultant thermal model using Kinzler and Grove (1992a,b, 1993), with percentages indicating the extend of melting. The black star shows the depth of the pooled melt calculation. B) SiO_2, C) FeO, D) Na2O and E) CaO versus MgO for Gakkel glasses (blue circles) and melt inclusions (red and green triangles). Black lines show crystallization paths calculated from Yang et al., (1996) at [ressure corresponding to the seafloor (~0.4 kbar), the maximum saturation pressure recorded in the melt inclusions (3 kbar; dashed) and the mean pressure of melting (10 kbar; solid). (Modified after Shaw et al., 2010).

While the classic conceptualization of the melt-generation region beneath a mid-ocean ridge is a two-dimensional triangle, along-strike variations in ridge structure require a three-dimensional approach. Ridge segmentation is likely to affect the shape and size of the melting region and the migration pathways that melts take to the spreading center (Figure 5). Sophisticated models that combine our knowledge of the geochemical and thermodynamic processes of melt generation with the physics of mantle flow and thermal evolution are needed to address the complexity of melt migration in specific geological examples (from Gregg et al., 2012).

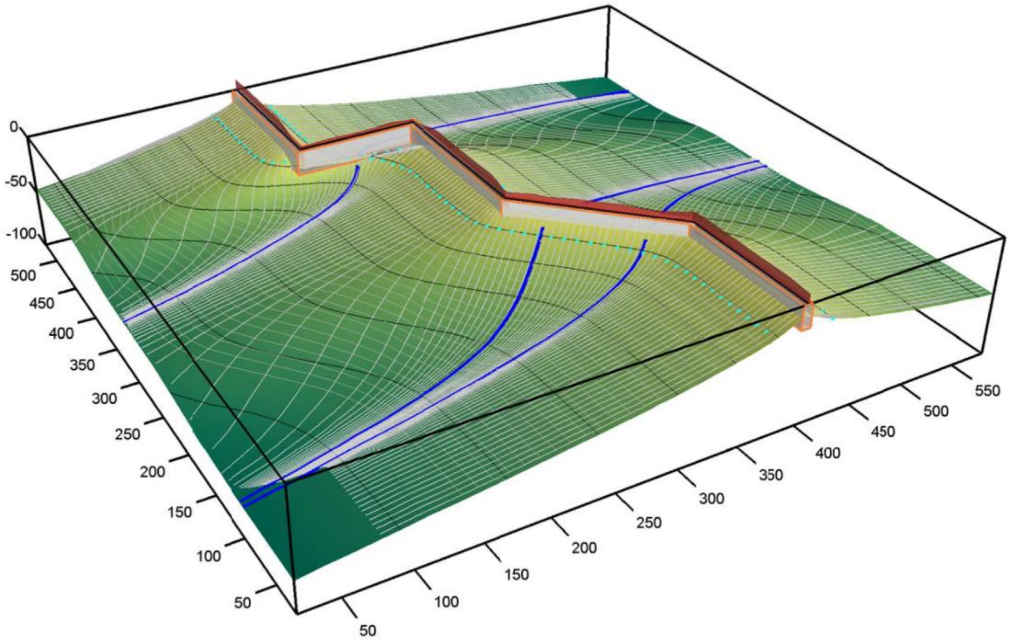

Figure 5. Permeability barrier and melt migration for a generic mid-ocean ridge model with three spreading segments offset by one transform fault and one oblique segment. Three-dimensional rendition of the barrier (green surface with black depth contours), melt trajectories are in white. The orange box represents the melt extraction zone. The height of the red surface along the plate boundary is proportional to the accreted crustal thickness. All the other elements in the figure are part of the numerical modeling used in Bai et al., (2017). (Modified after Bai et al., 2017).

However, observations available to test these hypotheses are predominately located on the narrow ridge axis. Geochemical analyses of lavas collected from near-axis seamount chains provide a unique opportunity to probe the three-dimensional mantle melt region feeding crustal accretion at an adjacent ridge segment (S. Allan, 1989; Batiza & Niu, 1992; Batiza & Vanko, 1984; Fornari et al., 1988a; Fornari et al., 1988b; Niu & Batiza, 1997; Perfit et al., 2012). The

Off-Axis Seamount Investigations at Siqueiros (OASIS) is a multidisciplinary effort to systematically investigate the 8°20’ N Seamounts Chain to better understand the melting processes near the 9° N segment of the East Pacific Rise (EPR). This project utilizes petrologic and geochemical analyses of samples collected by the DSV Alvin and via a dredging campaign in conjunction with morphological and geophysical data analyses to develop new, integrated models for upper lithosphere structure, deformation, and melt distribution at a fast-spreading center. This chain of seamount has never been investigated before so extensively. The goal is to test specific hypotheses for the dynamics of off-axis melting, using an interdisciplinary approach where spatially and temporally related geophysical and geochemical data analyses inform each other and are linked by geodynamic modeling. Constraining the timing of seamount emplacement is critical for linking compositional observations with geodynamic models of mantle melt generation and migration.

1.4 Site selection and geological background

1.4.1 Fluid flow of CO_2: Roman Valley Quarry fault zone

We selected the Roman Valley Quarry (Majella Mountain) as study site because of the excellent exposure of the inner structure of two oblique slip normal faults. Besides, the massive presence of fluid migration in the form of tar in the fracture systems makes this site a good natural analogue for studies of fluid flow in fractured media. Natural analogues provide the best opportunity to study migration mechanisms, as they incorporate such issues as scale, long-time system evolution and interacting variables that cannot be adequately addressed with laboratory studies or computer models (Annunziatellis et al., 2008). Majella Mountain is thought to be a possible analogue for the oil-producing subsurface structures discovered few years ago in southern Italy (Lampert et al., 1997). The presence of tar in the fracture systems exposed in the Roman Valley Quarry provided a unique opportunity to study a site where the migration is visible in outcrop, allowing a direct connection to the tectonic structures. The Roman Valley Quarry is located near the town of Lettomanoppello (PE), in the northern sector of Majella Mountain, central Appennines. The Majella Mountain is an asymmetric arc shaped anticline, located 40 km westwards of the Adriatic coast. The stratigraphic succession in the area is constituted by Upper Triassic-Upper Miocene carbonates and Messinian evaporites, followed by Lower Pliocene siliciclastic turbiditic deposits (Figure 6; Donzelli, 1969; Patacca et al., 2008; Vecsei, 1991; Vecsei et al., 1998; Eberli et al., 1993; Bernoulli et al., 1996; Casabianca et al., 2002; Rusciadelli et al., 2005; Figure 6). To the north, the fold axial trace trends NW-SE and bends in a NNE-SSW direction to the south, with the fold axis plunging gently and progressive toward the north and also toward the east and the west. Moving from the south to the north, the dip of the strata progressively decreases, from 30° to 10° in the Lettomanoppello area, where the younger deposits crop out. The growth of the Majella anticline started in Early to Late Pliocene times with its incorporation in the Appennines fold and thrust belt, followed by Late Pleistocene-Holocene by active extensional faulting (Patacca et al., 2008). The thrust plane outcrops in the Pretoro-Rapino areas, on the eastern limb of the anticline, placing the Majella anticline on the Lower Pliocene siliciclastic turbidites deposits. The western limb of the anticline is truncated by the Caramanico normal fault, characterized by a strong offset variation along strike, with a maximum throw of ~4km, whose timing of activity is still not well constrained (Sciasciani et al., 2002; Ghisetti & Vezzani, 2002; Pizzi et al., 2010). In the northern sector the main fault systems consist of normal faults and strike-slip faults. The main normal faults trend NW-SE and N-S and are linked to the final extensional tectonic phase, after the deposition of the Lower Pliocene Cellino Formation (Casnedi, 1983; Ghisetti e Vezzani, 2002) and before the deposition of the Lower Pleistocene Mutignano Formation. Marchegiani et al., (2006) performed a systematic study on the fault and fracture systems exposed in the Majella Mountain, to assess the dimensional, spatial and scaling properties of fault and fractures in carbonate rocks. The results of their study pointed out how the examined fracture populations belong to three main sets, with the oldest one trending roughly E-W, whereas the youngest sets are oriented NW-SE and NE-SW. Fracture apertures cluster around a NNW-SSE trend, parallel to the present maximum horizontal component of the stress field. In response to the actual stress field, they found also reactivated structures E-E and NW-SE trending. The distribution of the length of fault and fractures show a power law distribution, with a negative exponent equal to -1.88. According to the authors, this value may indicate a low degree of maturity of the analyzed faults and fractures. Fractures in the protolith show a quite regular spacing, mostly related to the bed thickness, while fault related-fractures show a general increase in frequency.

In the Roman Valley Quarry carbonate beds belonging to the Bolognano Formation crop out, dipping 10° to 25° to NE. The Bolognano Formation of Oligo-Miocene age represents the most recent stratigraphic unit of the Majella carbonate succession (Vecsei and Sanders, 1999) and was deposited on an isolated, gently dipping, homoclinal carbonate ramp under tropical conditions (Rustichelli et al., 2012). The Bolognano Formation comprises three members (Donzelli,1997):

- *Lower member*: medium to coarse grained carbonate grainstones, including calcirudite and marl-rich levels (~100 m thick);
- *Middle member*: carbonate mudstones and calcareous marls (~55 m thick);
- *Upper member*: fine-to-medium grained carbonate grainstones topped by a ~10m thick level with coarse grains (~100 m thick);

In the Roman Valley Quarry the lower member and the lower portion of the middle member crop out. The primary porosity (ϕ) of the Bolognano Formation is high, with a value ranging from 5% up to 30 % (Agosta, 2009). The area of Lettomanoppello is characterized by the presence of tar in the Oligo-Miocene deposits. The Roman Valley Quarry was an active mining site, since roman times, for the extraction of tar, traditionally used for wood waterproofing, fuel and other domestic uses. Agosta et al., (2009) recognized in the quarry three main structural domains characterized by the presence of tar: fault core, damage zones and porous carbonate beds. The faults play an important role in the migration of the tar, constituting the main pathways of subsurface fluid flow. During their ascent (from an unknown depth), hydrocarbons migrated also in the porous carbonate beds surrounding the faults. The authors performed a structural analysis of the structural elements associated to the pre-faulting deformation and of those related to the faulting.

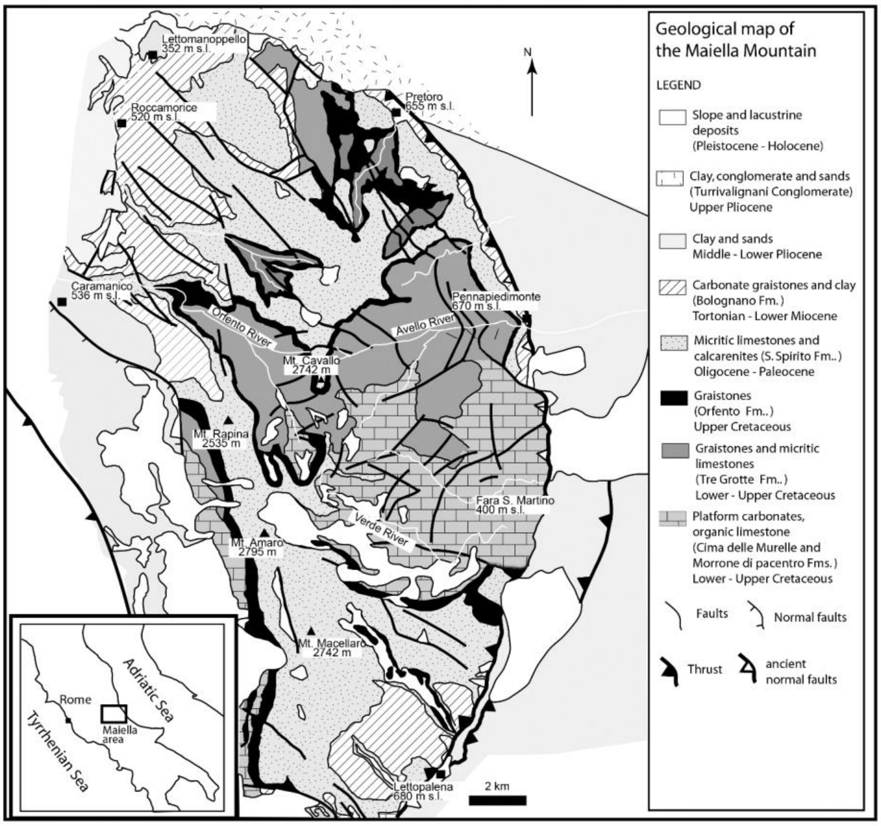

Figure 6. Geological map of Majella Mountain, (modified after Masini et al., 2011).

They distinguish the fractures as mode I (joints), anti-mode I (pressure solution seams), shared joints, sheared pressure solution seams, deformation bands. Faults are classified based on their total length and offset: incipient (length < 1m, offset <few cm), small (1m<length<10s m, a few cm<offset<10 cm), medium (10s m<length<100m, 10s cm <offset<about 1m) and large faults (length >100s m, offset>few m). Based on the structural analysis, the authors propose a three stages conceptual model of fault nucleation and development. Far from the faults, four main sets of pressure solution seams and one set of deformation bands characterize the background deformation. In the initial fault stage, incipient faults are characterized by shearing of pre-existing pressure-solution seams and formation of two main sets of tail pressure solution seams. With the ongoing faulting, exhumation, and growth of the Majella anticline (intermediate fault stage), opening-mode failure become the main deformation mechanism, with the formation of tail joints and veins within the evolving oblique normal faults. In this phase, there was the linkage of isolated slip surfaces, enhancing the degree of carbonate deformation. In the mature stage these structures evolved in larger faults, by strain localization around major slip surfaces, with brecciation and cataclastic deformation of the fault cores. Conversely, the carbonate damage zone surrounding the carbonate damage zones were affected by predominantly opening model failure and dilation of the favorably oriented pre-existing structures, as well as development of small and medium faults.

In the Roman Valley Quarry, two oblique-slip normal large fault zones are exposed characterized by 40 m (SW fault) and 10 m (NE fault) of throw respectively (Figure 7) and left lateral component of movement. According to Agosta et al., (2010), the SW fault dips 75˚ N and is characterized by two main slip planes ~N 290˚ and ~N 300˚. The NE fault presents instead several smaller segments oriented ~N270˚ to ~N315˚, dipping 60˚ to 80˚ either N or S. These two faults are consistent with most of the hydrocarbon flow postdating the faulting activity. Fault cataclastic rocks form seals for cross-fault fluid flow, since they do not show the presence of tar, while breccias and fault damage zones form conduit for fluid flow. For their internal structure, the SW fault show a combined conduit-barrier behavior, due to the presence of cataclastic rocks in the core, while the NE fault zone form a distributed conduit to fluid flow, for the discontinuous presence of cataclastic fault rocks and breccias.

Agosta et al., (2010) investigated the role played by fractures on fluid migration in the Roman Valley Quarry, studying the relationship among individual fracture characteristics (length, spacing, orientation, connectivity, and distance from slip surfaces) and tar residues. In particular in the fault damage zones, the interconnected fractures provided high values of secondary porosity (up to 1.1%, with a mean value of 0.45%) and are characterized by a pronounced anisotropy. They did not find differences in terms of length and spacing values between for both tar-free and tar-rich fractures. The fault related fracture sets show power law spacing and length distribution. The carbonate host rock is made up instead of a quite isotropic fracture array comprised of isolated and coupled fractures, in which individual fractures sets have negative exponential distributions. These characteristics make the fracture arrays in the damage zone enhancing the fluid flow, with respect to the fractures in the host rock that have fluid storage properties.

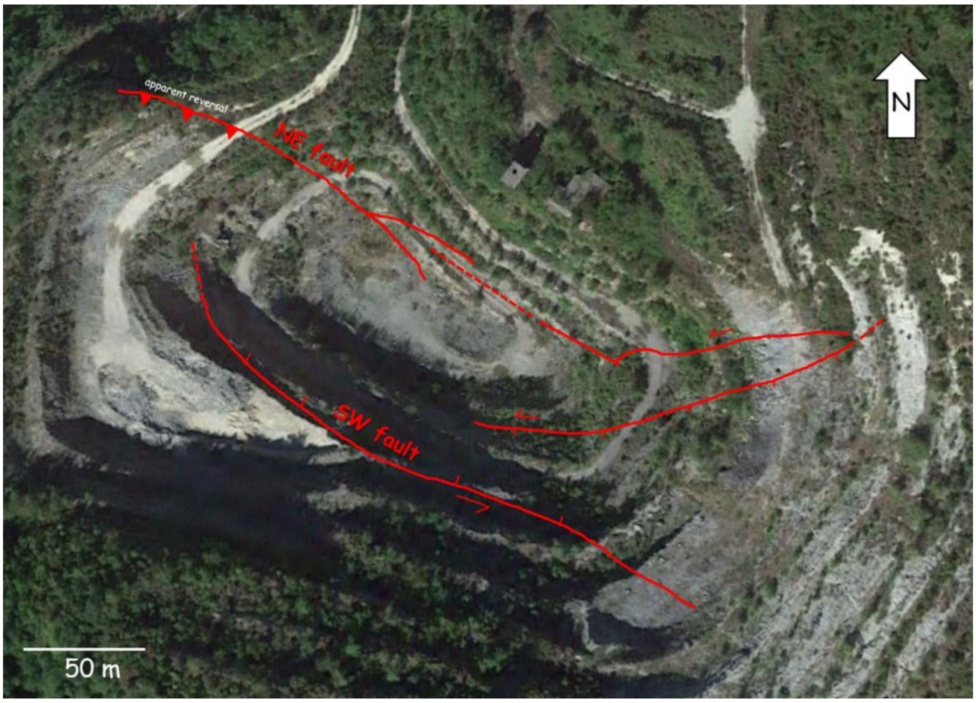

Figure 7. Aerial view of the Roman Valley Quarry with the three fault traces in red.

1.4.2 Melt migration: the 8°20’ N Seamount Chain.

The 9°-10° N ridge segment of the East Pacific Rise (EPR), is one of the most extensively studied MOR segments of the global ridge system (White et al. 2006). The focus of this study is a chain of near-axis seamounts, located at 8°20’ N, which extends 160 km (~3.6 Ma lithosphere) westward from their initiation ~15 km northwest of the EPR-Siqueiros ridge-transform intersection (RTI). (Figure 8)

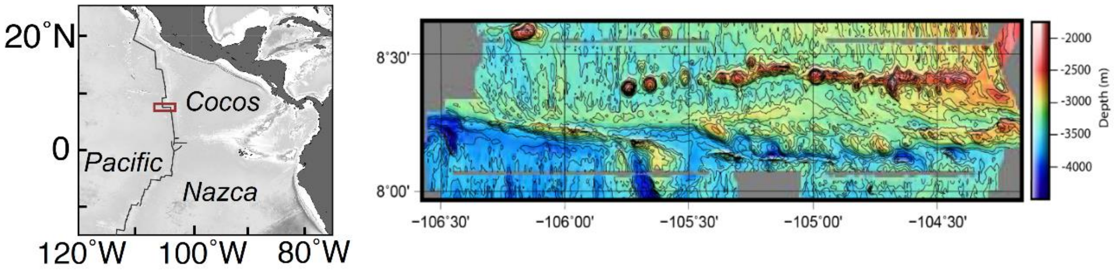

Figure 8. Location of the study area northwest of the Siqueiros transform fault flanking the East Pacific Rise (EPR). To the right a detail of the 8°20’N seamounts chain from EM122 multibeam data collected by the R/V Atlantis during the 2016 OASIS Expedition.

The full spreading rate increases form 111 mm/yr at Clipperton transform fault to 120 mm/yr to Siqueiros (Klitgord and Mammerickx, 1982). The first order segment of the ridge is magmatically active and is partitioned in two segments by a second order discontinuity, the 9˚03' N Overlapping Spreading Centers (OSC) (Macdonald et al. 1992).

An extensive magnetic data analysis was performed by (Carbotte and Macdonald, 1992) in order to establish the evolution of the region in the past 2.4 Myr. According to the authors, the OSC has evolved in width from 2 km to 8 km in the past 1 Myr, leaving a *v-shaped* discordant zone that indicates a southward migration at an average rate of 42 km/yr since *anomaly 2 time*. The growth of the OSC may be causally related to the 3˚-6˚ counterclockwise rotation of the Pacific-Cocos plate, inferred from the orientation of the magnetic isochrones. Along the crest of the EPR a magnetization high is observed as well as at the RTI and the OSC. Madsen et al. (1990) made three dimensional analyses of gravity data for the 9˚N region and they found that the anomalies are consistent with the presence of a low-density crustal magma chamber at the rise axis as a narrow, small body surrounded by a wider region of cooling crustal rocks. Wang et al. (1996) studied the gravity and crustal structure of the 9˚N EPR segment, showing very little along axis variation in the Mantle Bouguer Anomaly, while the subcrustal gravity anomalies present a strong gradient, with a gravity low around 9˚50' N. This gravity signature could be attributed to an enhanced focusing of upwelling mantle at that location.

Kent et al. (1993) found an asymmetric pattern of melt beneath the 9˚03' N OSC due to a gradual, en-echelon accommodation of melt supply across the OSC offset relative to the neo-volcanic zone. Barth and Mutter, (1996) used the seafloor-to-Moho reflection travel time as a valid proxy for oceanic crustal thickness. According to the authors the segment between the Clipperton transform fault and the 9˚03' N OSC presents the thinnest crust near 9˚50 N (5 km) and locally beneath the 9˚03' N OSC (4.7 km), while the thickest crust was found between 9˚10' N and 9˚20' N, just north of the 9˚03' N OSC. The authors hypothesize that this variation in the crustal thickness can be associated to the presence of a diapiric upwelling center beneath the EPR near 9˚40' N and 9˚50' N, in accordance to the low gravimetric signature observed by Wang et al. (1996) for this area. Canales et al. (2003) calculated a 2D crustal thickness and velocity structure of 15-300 kyr old crust in the 9˚ N area. They found that the mean crustal thickness is 6.7-6.8 km and the total range of crustal thickness variation is 2-2.5 km. The thickest crust is beneath the Lamont seamounts (~9km) and in the *v-shaped* area north of the 9˚03' N OSC (7.3-7.8km) (Allan et al., 1988; Barone and Ryan, 1990; Fornari et al., 1988c).

The thinnest crust (<6km) is found close to the Clipperton and Siqueiros fracture zones, while the area beneath the 9˚03’ N is not anomalously thin. The authors suggest the crustal thickness variation along the northern segment can be attributed to the southward migration and evolution of the 9˚03’ N over the past 0.5 My, rather than to the presence of a large diapir at 9˚50’ N.

Other important features observed in the area are the intra-transform spreading centers (ITCs), that often characterize the segmentation of oceanic transform faults along fast spreading ridges (e.g., Siqueiros, Quebrada, Discovery, Gofar, and Garrett transform systems), (Fox and Gallo, 1984; Menard, 1967; Menard and Atwater, 1969; Searle, 1984; Fornari et al., 1989; Hekinian et al., 1992; Hékinian et al., 1995; Perfit et al., 1996; Nagle et al., 2007). According to the magnetic data their onset within the Siqueiros transform domain has developed since the Brunhes anomaly (0.73 M.yr.), probably due to the change in spreading direction (Carbotte and Macdonald, 1992). Pockalny et al., (1997) show the results of a tectonic reconstruction for the 9˚N region, founding a series of counterclockwise changes in the spreading direction about 3.5 Ma, 2.5 Ma, 1.5 Ma and 0.5 Ma. The plate reorganization could be the cause of a series of extensional events in the Siqueiros Transform Faults and could be responsible for the formation of the ITSCs and flexural transverse ridges. Even if they do not address the 8˚20’N seamount formation to the changes in plate motion, they suggest that a relationship must exist between the seamounts chain and the western Siqueiros RTI. Gregg et al. (2007) found negative residual mantle Bouguer anomalies within several transform faults for spreading full rates >~50 mm/y, indicating a mass deficit within these settings. One of the potentially important mechanism invoked is crustal thickening, due to the strong correlation between the observed RMBA and the topographic highs in the area. Gregg et al. (2009) modeled melting, fractional crystallization and melt extraction at segmented oceanic transform faults (with application to the Siqueiros Transform System), explaining the observed gravity-derived crustal thickness variations with a melt migration in the transform domain from a wide region of the mantle surrounding it. The observed negative Residual Bouguer Anomalies and its explanation through melt migration towards the transform faults region suggest that not all magma is focused to the ridge axis, but part of it may feed off-axis magmatism.

Near axis seamounts in the 9˚-10˚ N region are numerous and have a continuum of trends ranging from relative motion parallel to absolute motion parallel, (Macdonald et al. 1992; Allan et al. 1994; Batiza and Vanko, 1984; Niu & Batiza, 1991, 1993; Scheirer & Macdonald, 1995). In comparison, the 8˚20’ N seamounts do not follow a hot spot reference frame trend, in fact the chain runs parallel to the Siqueiros fracture zone, at an average distance of 15-20 km. The overall strike of the seamounts chain is 269˚, more closely associated with the relative motion trend (264˚) or the trace of the western fracture zone close to the RTI, with some changes in the trend at ~1.8 and 0.8 Ma (Pockalny et al. 1997). The seamount chain is characterized by discrete edifices in the oldest part of the chain, while east of 105˚30’ W, the chain is a nearly continuous volcanic ridge, comprised of small cones and coalesced edifices with some evidences for rift zones, craters and calderas on the larger constructs. According to Macdonald et al. (1992) and Scheirer et Macdonald, (1995) the uniform high reflectivity on the side scan sonar record, should not indicate a progression in age along the chain, but rather a line of active volcanism. These observations motivate two end-member models for the how the chain formed: (1) the seamounts formed near the ridge axis along with the oceanic lithosphere they were emplaced upon and were rafted off with the plate; (2) the seamounts formed at a later time and represent more recent volcanism, younger than their underlying lithosphere.

1.5 Thesis overview

The thesis describes the work done on two different geological scenarios: the fault zone exposed in the Roman Valley Quarry and the 8˚20’ N seamount Chain, along the fracture zone of the Siqueiros Fracture Zone, in the East Pacific Rise. The study of the fluid flow of CO_2 in the fault zone spans from Chapter 2 to Chapter 7, from the data collection to the numerical modeling. The study on the 8˚20’N seamount chain is reported in Chapter 8, since it represents the main content of the paper in preparation: “Formation and evolution of the near axis 8˚20’ N Seamount Chain” (Romano et al., 2017 in prep.). The workflow can be summarized as follow:

- Chapter 2 describes the collection and analysis of the data acquired in the field work activity for the study of the fault zone of the Roman Valley Quarry (Majella Mountain);
- Chapter 3 describes how the fracture modeling has been approached, in order to characterize the hydraulic parameters of the fracture systems, using both commercial and open source software.
- Chapter 4 describes the modeling of fluid flow at the scale of the fault, combining the results of Chapter 3 on the fractures of damage zone of the fault with literature data on core and host rock, with a hybrid numerical approach. The equations governing the numerical simulation, along with the parameters used are described.
- In Chapter 5 the first results of the numerical simulation are presented, testing the proposed workflow to model the fluid flow in the bulk fault zone with the “Discussio
- In Chapter 6 and Chapter 7 “Discussions” and “Conclusions” are presented respectively.
- Chapter 8 describes all the geophysical analysis and interpretation conducted on the data acquired during the OASIS expedition, along with the discussions and the conclusions about the possible mechanism and timing of emplacement of the 8˚20’N seamount chain.

2. FIELD DATA

2.1 Data collection

One of the major issues in numerical modeling of fluid flow in fractured media is the representation of the fracture systems as geometrical models; this requires quantitative description of the locations, orientations, sizes, shapes, and aperture of all the fractures. These parameters, especially locations, shapes, orientations, and dimensions are typically three dimensional but almost all the information and data collection are usually obtained through one or two-dimensional measurements. The main techniques employed in the field are borehole logging of fracture orientation or scanline and window mappings of surface outcrops. From these two-dimensional information, we can extrapolate the three-dimensional properties of fracture systems.

The characterization of the fracture systems in the NE fault zone of the Roman Valley Quarry was performed using the scanline approach, along 21 lines uniformly distributed along the fault profile, on the vertical outcrops and on the quarry pavements; the map showing the position of the scanlines is in the *Appendix*. In the scanline of a section of the outcrop, a tape with length marks is fixed onto the exposure in a chosen direction (Figure 9). The following parameters are acquired only for the fractures intersecting the tape.

- *Distance*: the distance to the fracture’s intersection with the tape (measured from the starting end of the tape).
- *Orientation*: dip direction angle (α) (with respect to the North) and dip angle (β) (measured from a horizontal plane).
- *Trace length*: length of the fracture trace, used to estimate the size distribution.
- *Aperture*: the distance between two fracture surfaces.
- *Filling*: if it is present, specify the nature of the filling (e.g. calcite, tar, other).
- *Termination*: specify if the fracture terminates against another fracture, into the matrix or other.

For the fractures on the pavement of the quarry, only the distance was acquired, because of the limited exposure of the fractures.

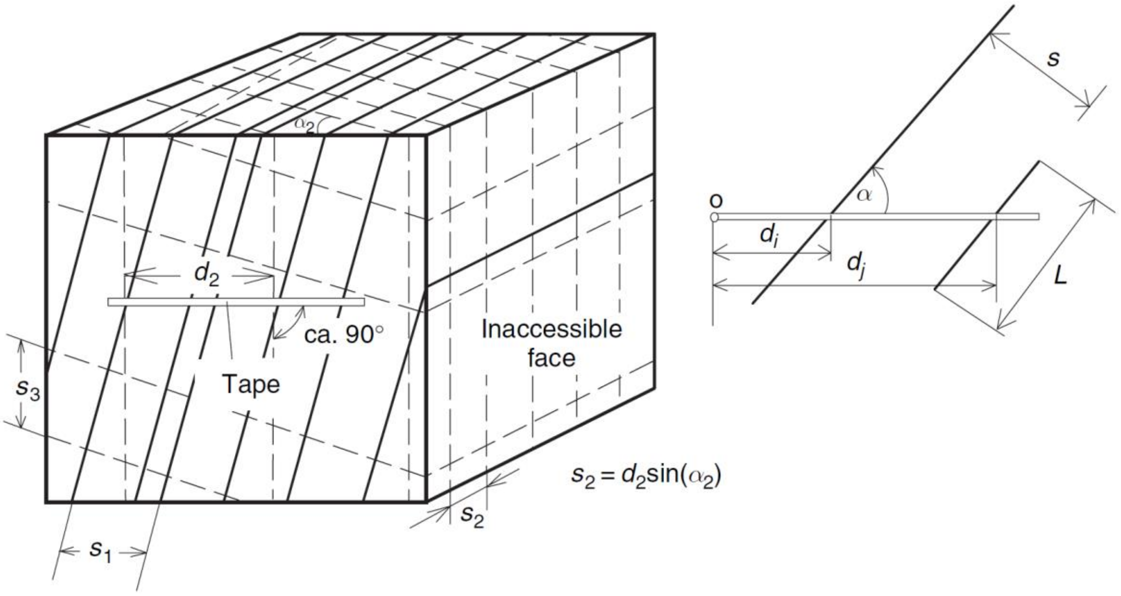

Figure 9. Sets of fractures and measurement of spacing by the scanline method (ISRM, 1978); α is the angle between a fracture trace and the tape; d, the distance between the intersection of a fracture with the tape and the origin of the tape; L, the trace length of a fracture.

2.2 Data analysis

A large degree of uncertainties is associated with the geometric properties of the fractures and this has a strong influence on the choice of the best numerical method to represent the fractured domain. Because of their fractal geometry, fractures are usually organized in sets, i.e. groups of fractures with similar orientation that reflect the lithology properties and the state of stress of the rock mass. Most of the parameters of a fracture set can be related to another and can be represented by a specific *Probability Density Function* (PDF). The statistical analysis of the data collected in the Roman Valley Quarry was performed using the commercial software Move®. The scan lines were carried out both at the fault hanging wall (HW) and footwall (FW) of the fault, to take the well-known strain asymmetry between both fault blocks of dip-slip faults into account. All the parameters acquired in the fieldwork along the scan lines are described in this chapter and are reported in the *Appendix*.

2.2.1 Orientation

The acquisition of the orientation of the fractures along a scanline can introduce some bias because of the angle between the sampling line and the normal to the fracture plane, δ. To reduce this bias, a correction factor w (Terzaghi, 1965) must be applied to all the orientation data:

$$w = 1/cos\delta \tag{1}$$

The direction angle (α) and dip angle (β) of a fracture can be represented on a hemispheric projection by a single point, called *pole* or *normal point*. From the amount of clustering of the poles, sets of fractures can be identified, according to the number of fractures falling into a user defined finite solid angle ψ around the pole. Once the fracture sets were identified, the Mean Resultant Orientation (MRO) for the dip direction and the dip angle are calculated for each set, along with their PDF. Usually the von Mises-Fisher's distribution is employed to describe the orientation distribution. The von Mises-Fisher distribution is characterized by the following parameters:

- MRO (Dip, Dip Azimuth)
- Dispersion $\boldsymbol{k}$
- Cone of confidence (angle α(1-p))

The dispersion can be approximated by:

$$\boldsymbol{k} = \frac{(n-1)}{(n-R)} \tag{2}$$

where R is the length of the resultant vector, (i.e. the magnitude of the vector sum of all pole vectors in the set) and n is the number of observations. This approximation is sufficiently accurate if $\boldsymbol{k}$ is greater than 10. Fisher et al., (1887) gives a test concerning model parameters which is valid also for small sample sizes.

The cone of confidence, within which the unknown true mean lies at a confidence level (1-p), is given by:

$$\alpha = \alpha\, cos\left(1 - \frac{n-R}{R}\right)\left\{\left[\frac{1}{P}\right]^{\frac{1}{n-1}} - 1\right\} \tag{3}$$

The standard choice for the probability confidence level (1-p) is 0.95 and the confidence limit is usually denoted α_{95}.

The analysis on the orientation of the fracture was performed with Move®. Fracture orientations acquired in the fieldwork were divided between the hanging wall and the footwall of the fault. According to the criteria exposed above, for both fault hanging wall and footwall damage zones, four sets of fractures are recognized; the stereographic projection for each set are reported in Figure 10 and the relative specific features are reported in Table 1.

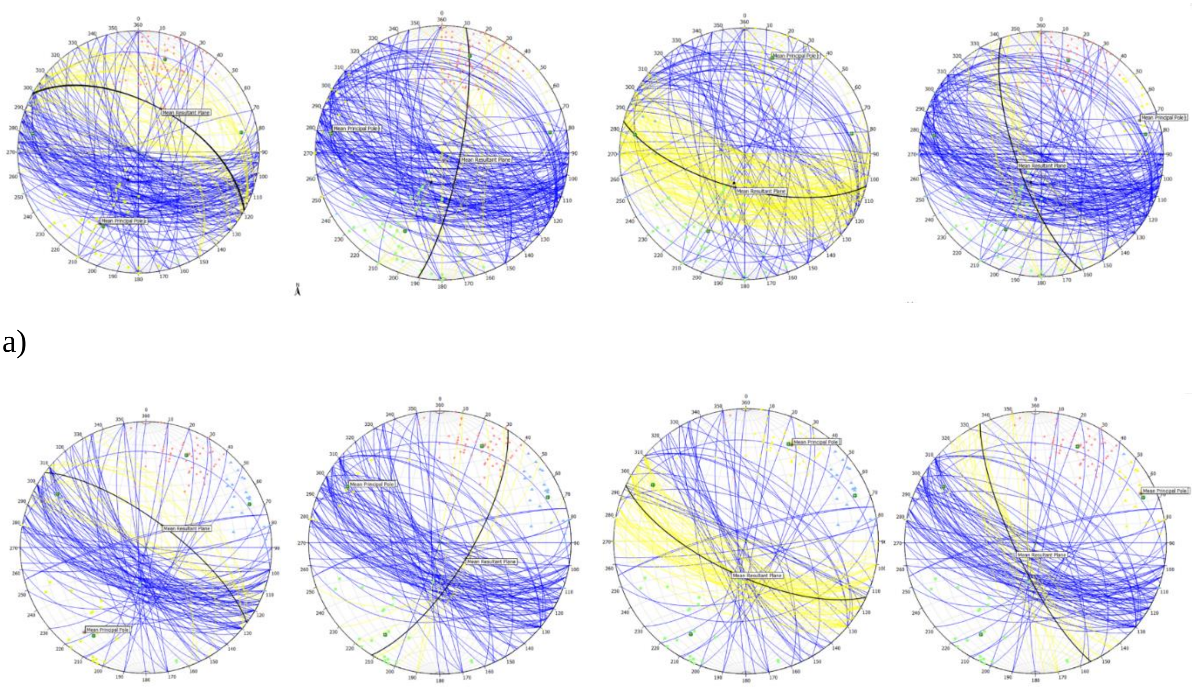

a)

b)

Figure 10. Stereographic projections of the fracture systems in the footwall (a) and hanging wall (b) damage zones: fracture plane projections are represented in blue; the planes in yellow point out the fractures belonging to the same set, whose MRO plane is drawn in black. The colored points are the pole projections of the planes of the different sets.

*Table 1. Parameters for each fracture set obtained by statistics analysis of the fracture orientation: Fisher's dispersion **k** and MRO (see text for explanation) are shown for both the footwall and hanging wall damage zones.*

Fault Footwall				
Data statistics	Set 1	Set 2	Set 3	Set 4
Dispersion ***k***	9.19	14.84	18.70	24.17
MRO	57.16/29.12	78.25/100.85	67.26/194.97	73.14/250.97
Fault Hanging wall				
Data statistics	Set 1	Set 2	Set 3	Set 4
Dispersion ***k***	14.95	13.98	28.20	33.61
MRO	72.25/36.59	71.4/121.25	69.05/204.93	77.04/244.99

2.2.2 Aperture

The aperture is one of the most difficult fracture properties to measure, because of the intrinsic limitations in sample size and its measurement. There are three different types of aperture that we can define/measure: geometrical, mechanical, and hydraulic. All apertures depend on the applied stress, surface roughness, infilling materials, fracture size and it is clear how it is a challenge to measure the true aperture of a fracture. The aperture of the fracture systems in the Roman Valley Quarry was acquired using a caliber, measuring the distance between the fracture walls. The values found are in accordance with literature data (Agosta et al., 2010), with values in the order of 10^{-1} mm, but in some cases, up to few mm, because of alteration. The Cubic Law (4) describing the flow into a single fracture characterized with smooth surfaces (parallel plate model) separated by an aperture b, is a particular solution of the Navier-Stokes equation (Witherspoon et al., 1980). The permeability of a fracture is directly related to its aperture, (Eq.5).

$$Q = \frac{-\rho g}{12\mu} b^3 \nabla h \tag{4}$$

$$K = \frac{b^2}{12} \tag{5}$$

where ρ is the fluid density, g is the acceleration of gravity, μ is the dynamic viscosity of the fluid, h is the hydraulic head.

2.2.3 *Filling*

All over the Roman Valley Quarry there are evidences of tar migration, whose presence can be used to distinguish zones of the fault with higher permeability. Tar is present both in the fracture systems and in the breccias and cohesive cataclastic rocks.

In the southern portion of the fault, most of the fractures filled with tar are oriented parallel to the main fault plane; the cores in this portion of the fault is very well developed with a strong presence of tar in the fault rocks. In the northern part, the tar is more distributed. There, the fractures filled with tar are also perpendicular to the main fault plane, probably because of the closer presence of the SW fault, enhancing the degree of fracturing and deformation in the damage zone. The fault cores are less developed, with a small amount of tar present in the fault rocks compared to the southern part of the fault.

2.2.4 *Size and trace length*

The size of the fracture is an important parameter that strongly influences the connectivity of the fracture and hence its permeability and deformability. Over an outcrop exposure, the only information that we can acquire about the size of the fractures is their trace length. The size of the fractures can be inferred from the trace length and assuming a shape, usually circular, elliptical or rectangular (Robertson, 1970; Einstein and Baecher, 1983; Long and Witherspoon, 1985; Rasmussen et al., 1985).

Table 2. Range of lengths for each fracture system of the hanging wall and footwall damage zone

Footwall				
Diameter (m)	Set 1	Set 2	Set 3	Set 4
Maximum	0.05	0.14	0.04	0.14
Minimum	3.50	0.95	3.00	2.80
Hanging wall				
Diameter (m)	Set 1	Set 2	Set 3	Set 4
Maximum	0.16	0.24	0.04	0.12
Minimum	2.80	0.60	3.50	2.80

The length of each fracture set was measured in outcrop as from the scan line (see tables in the *Appendix*). Assuming a circular shape for the fractures, the sum of the length values (up and down) corresponds to their diameter. Table 2 shows the maximum and minimum values for each set for both the maximum and minimum values for each set for the damage zones of the fault hanging wall and footwall.

The Probability Density Function (PDF) generally used to represent the length distribution in a fracture system are the log-normal distribution, the power law distribution or the exponential distribution. In this case, the PDF for the size and trace length of the fractures is the power law:

$$p(l) = Cl^{-D} \qquad \text{for } l \in [l_{\text{min}}\ l_{\text{max}}] \tag{6}$$

where l is the fracture length, D is the length exponent, $l_{\text{min}}\ l_{\text{max}}$ is the range of the modeled fracture size (in this case the diameter of the fractures), C is a constant. In the figure below, you can see one of the PDF for the footwall damage zone (Figure 11).

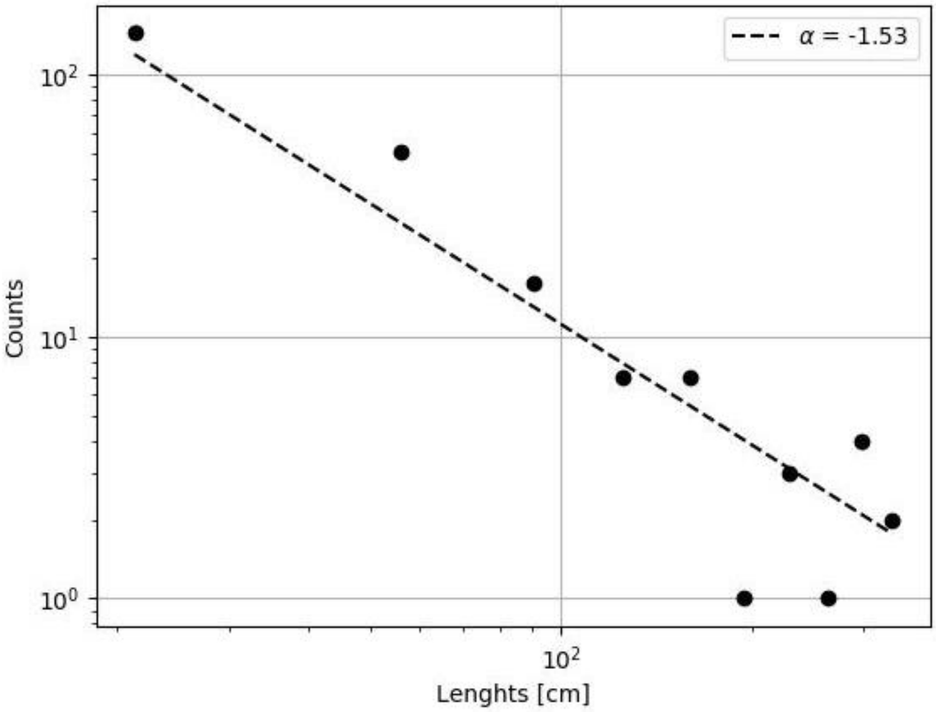

Figure 11. Log-log power law distribution for the fracture lengths of the footwall damage zone.

2.2.5 Fracture intensity

There are many ways of defining fracture intensity: e.g., fracture frequency, fracture density, fracture intensity, or fracture porosity. They are all subject to high degree of bias and are highly directional.

The frequency of fractures λ is usually expressed in terms of the mean number of fractures per unit length (1D), per unit area (2D) or per unit volume (3D). The reciprocal of the linear frequency λ is the spacing s=1/ λ.

Figure 12 shows an example of the trend of the spacing along one of the scan lines: the areas where the spacing is zero represent the part of the scanline that intercept the cores of the planes characterizing the fault. The three peaks characterized by 60 cm of spacing can be considered, as an example, as belonging to the same family of fractures. The spacing *s* was used as a proxy to distinguish areas along the fault profile, characterized by similar values, and hence similar frequencies.

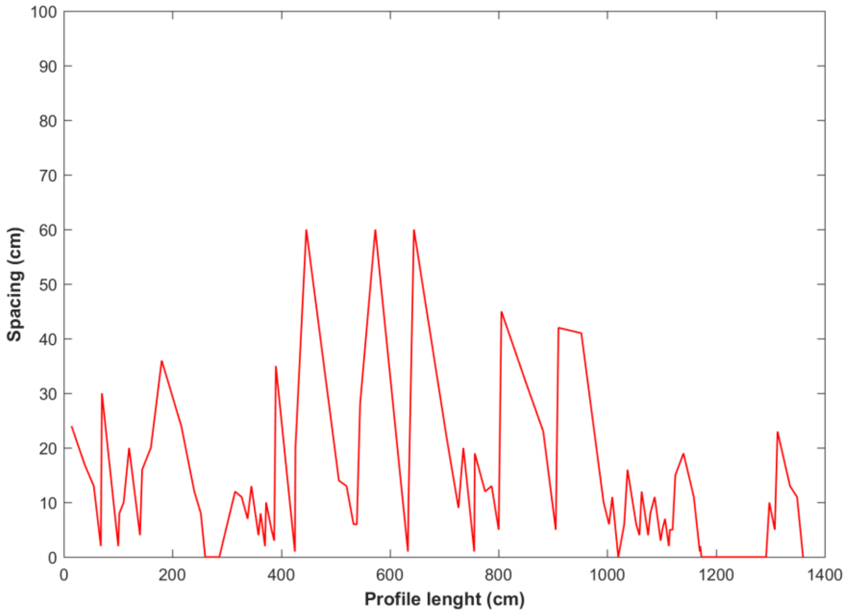

Figure 12. Spacing trend along scanline 3 (see text for explanation).

Figure 13 illustrates the relationship between the dimension in which we are performing the measurement and the dimension of the sample, expressed in terms of fracture density, intensity, and porosity.

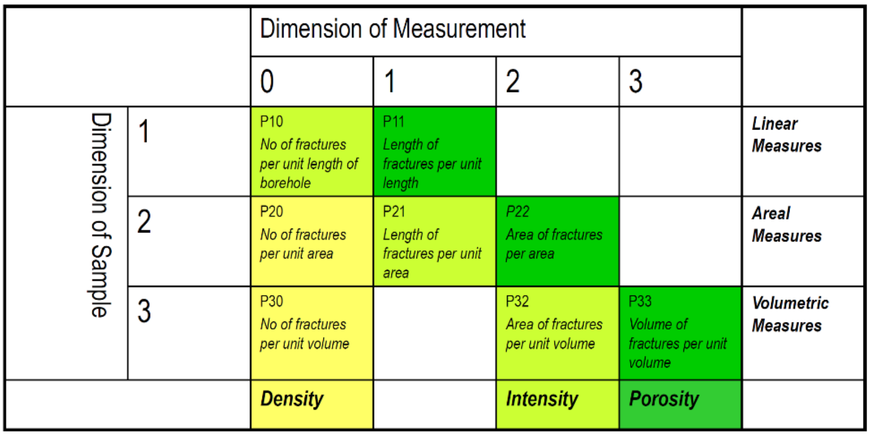

		Dimension of Measurement				
		0	1	2	3	
Dimension of Sample	1	P10 *No of fractures per unit length of borehole*	P11 *Length of fractures per unit length*			***Linear Measures***
	2	P20 *No of fractures per unit area*	P21 *Length of fractures per unit area*	P22 *Area of fractures per area*		***Areal Measures***
	3	P30 *No of fractures per unit volume*		P32 *Area of fractures per unit volume*	P33 *Volume of fractures per unit volume*	***Volumetric Measures***
		Density		***Intensity***	***Porosity***	

Figure 13. Relationship between the dimension of the measurement and that of the sample. (from Golder., 2008).

The P32 is a true non-directional rock mass property. Although it cannot be directly measured, it can be inferred from the P21 or the P10 based on linear correlations (Dershowitz & La Pointe, 1994; Dershowitz & Fidelibus, 1999):

$$P32= C31*P10 \text{ and } P32= C32*P21 \tag{7}$$

where C31 and C32 are constants of proportionality depending on the fracture geometric parameters and the orientation of the sampling window or scan line. Starting from the value of the P10 and considering a unit volume for the hanging wall and footwall damage zones, the calculated P32 are respectively 8 and 6, pointing out the high degree of fracturing in the damage zones.

2.3 Modeling of the southern and northern sectors of the fault

Based on the field observation of tar distribution and the properties of the fracture systems, a first numerical analysis was performed to characterize the hydraulic differences between the northern and southern part of the fault zone. The spacing of the fractures was calculated for each scanline, both for the vertical outcrops and for the pavement, and used as a proxy to see regions along the fault profile characterized by similar values. By comparing the trend of the spacing of the fractures along the fault profile, different surfaces were created with the software Move®, to identify rock volumes characterized by the same fracture intensity, and distinguish also the damage zones from the core of the fault. Figure 14 shows the surfaces separating the different volumes along the fault profile.

The dimension of the volumes follows the real dimension of the fault exposed in the quarry: three volumes were constructed for the northern part of the fault (Figure 15) and two volumes for the southern one (Figure 16). These volumes were used as model domains for the numerical simulation, to study the distribution of the permeability along the fault profile. The surfaces were corrected and simplified, because the software cannot converge for small volumes (0.1 m^3) characterized by rough wall surfaces.

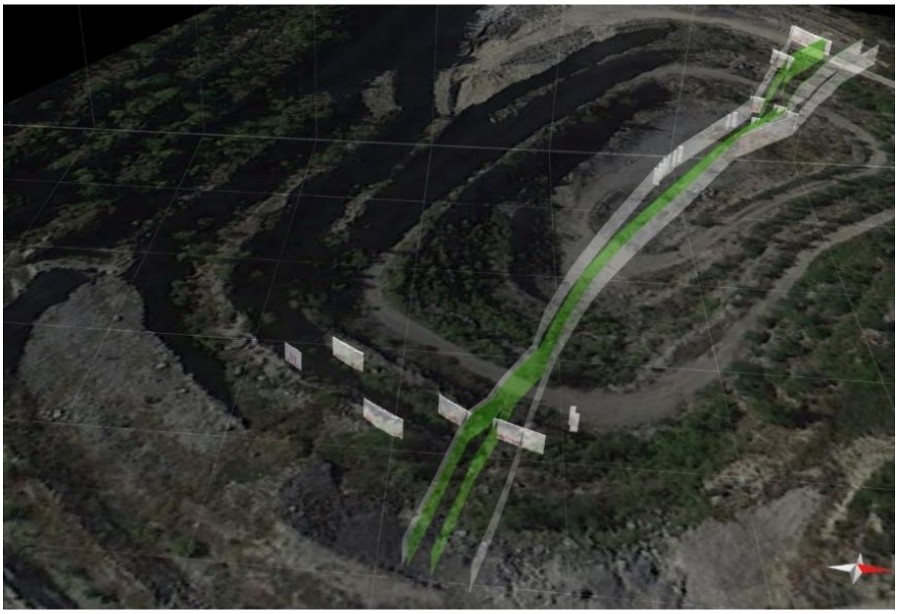

Figure 14. Surfaces separating areas characterized by similar values of the fracture spacing along the fault profile. The vertical white surfaces are the traces of the scanlines with the graphs of the spacing superimposed. This representation helped in the process of tracing of the surfaces.

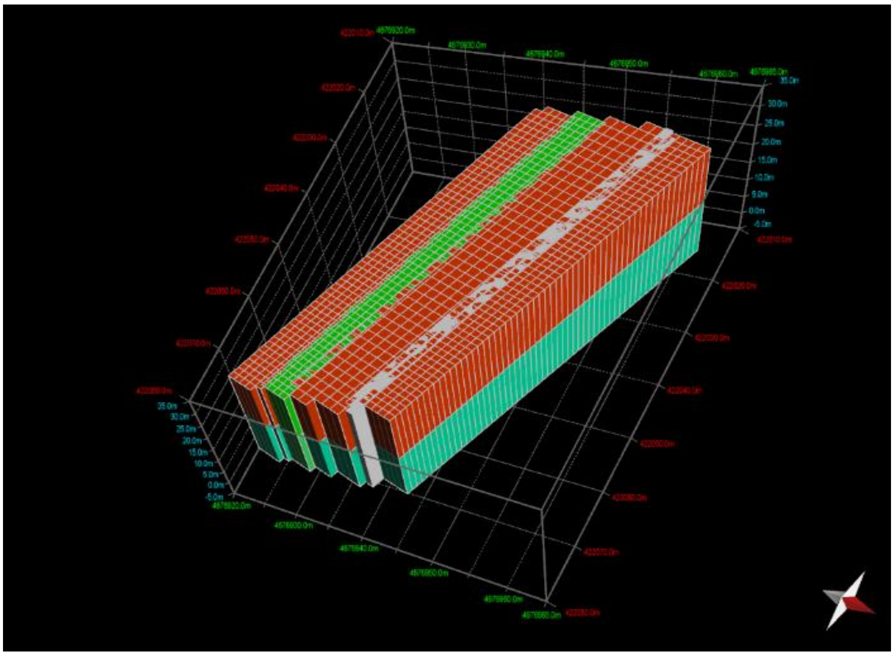

Figure 15. Volumes of the northern portion of the fault, cores are in green and gray (see text for explanation).

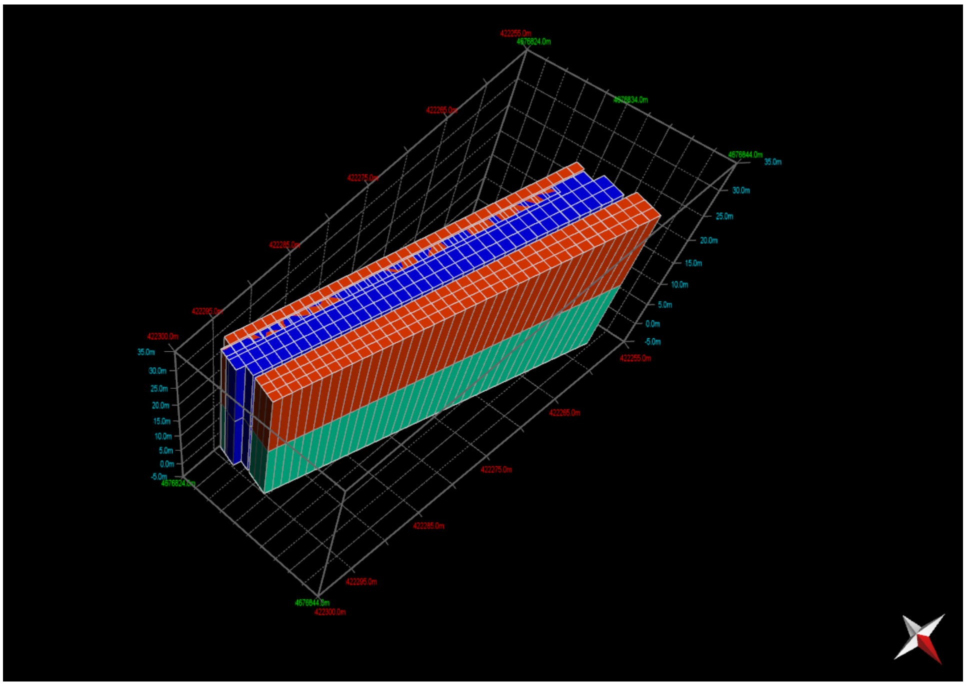

Figure 16. Volumes of the southern portion of the fault, the core is in blue (see text for explanation).

3. Fracture modeling

The macroscopic properties of a fracture network consist of geometrical, topological properties (connectivity and percolating character), and transport properties (permeability) (Sisavath et al., 2003). One of the main challenges in modeling fracture networks is the geometrical representation of complex three-dimensional (3D) discontinuity systems. Since direct observation of detailed 3D structure of fracture networks is not possible, their description must rely on extrapolation from 1D/2D data (Lei et al., 2017). The connectivity of a fracture system determines the flow patterns in a fractured rock mass. Fluids flow through the connected fractures when the so-called percolation threshold is reached: i.e., permeability become higher of that of the rock matrix (Berkowitz and Balberg, 1993); isolated fractures don't contribute to the flow. Fractures act as channels and flow through the rock mass is controlled by the location, orientation and characteristics of individual fractures or fracture sets.

In numerical modeling of fractured rock masses, using a continuous or discrete approach to reproduce the fracture system depends on different parameters, such as the conceptual model, the problem size, the computational capacity. It is often useful in practice to use both techniques, with a discrete representation for the near-field part of a problem and a continuum representation for the far field. In this way the advantages of both discrete and continuum approaches can be exploited at appropriate scales.

The modeling of the fractures of the damage zone of the Roman Valley Quarry fault were performed using a discrete approach, treating the fractures as individual components of the system. These numerical methods for discrete systems are the discrete element methods (DEM), which includes all numerical methods that model the problem domain as an assemblage of independent units. The topological information is explicitly represented and is used in the simulation of flow and transport. The first step in the DEM approach is to set up the geometrical model, describing the geometry of the connected fractures; the flow solution inside the fractures can be achieved using special numerical and analytical methods.

The Discrete Fracture Networks (DFN) method is a specific technique within DEM, for modeling flow and transport in fractured rocks. This technique was introduced in the late 1970's for both 2D and 3D problems (Long et al., 1982; Andersson et al., 1984; Endo et al., 1984; Robinson & Tester, 1984; Smith & Schwartz, 1984; Andersson & Dverstorp, 1987;

Dershowitz & Einstein, 1987). The DFN approach can be defined as: "*analysis and modeling which explicitly incorporates the geometry and properties of discrete features as a central component controlling flow and transport*" (Dershowitz, 2004).

The DFN method is based on the representation of fracture geometry through stochastic simulations, using probability density function of geometric parameters of the fractures (e.g. density, orientation, size aperture or transmissivity) formulated accordingly to field measurements, in addition to assumption about fracture shapes. The fracture network of the reservoir is then simulated using a random number generation according to the parameter distribution function. The network obtained is not the real one, it represents only one of the possible configurations (*realization*), that have a statistical partial equivalence. To have a statistical significance, multiple realizations of the fracture systems must be calculated, to obtain a spectrum of solutions, whose collective behavior can be considered a good representation of the real system.

The quality of the fracture network generated is strictly related to the quality of the field data and hence its adequacy and reliability is difficult to be evaluated. Despite this limitation, DFN methods are an excellent tool to model fluid flow and transport, since they capture phenomena that are difficult to represent in conventional equivalent continuum approaches. However, these methods are computationally demanding and require cares in constructing computational meshes.

For the study area, the fracture systems mapped in the field were modeled by considering the following goals:

- Model the hydraulic differences observed in the field between the southern part and the northern part of the fault;
- Characterize the hydraulic parameters of the fault footwall and hanging wall damage zones and use these parameters to model the fluid flow in the whole fault zone, coupling damage zones and core.

3.1 Modeling of both northern and southern sectors of the fault

The first numerical model of fracture properties was developed using Move® and it is based on the field data of the fault domain described in Chapter 2, distinguishing the northern and southern portion of the fault zone. Different volumes were built, enclosed in surfaces that separate regions characterized by a different fracture frequency. For each volume a DFN was constructed using the Fracture Modeling module in Move®, which generated stochastic DFN for a Geocellular Volume based on user-defined input parameters. In the geocellular method, the rock volume is discretized into volumetric cells and each cell is linked to appropriate properties. In a geocellular DFN model, the fractures and their properties are generated directly form that cell-based information. The input parameters used to create the DFN include:

- Fracture length
- Orientation
- Aperture
- Aspect ratio
- Fracture intensity (P32)

Random number generators are used to generate the fracture length distribution according to the Power Law probability density function (see 2.2.4 *Size and trace length*). Each length generator uses a method called "average_length_squares" which calculates the average length squared for each fracture. The *Total Area of Fractures* (A_{TOT}) required to give the prescribed P32 is defined as:

$$\mathbf{A_{TOT}=P_{32}V} \tag{8}$$

where V is the volume of the cell in meters. The *Number of Fractures* (N_f) to generate is therefore:

$$\mathbf{N_f = A_{TOT}/A} \tag{9}$$

Where A is the average length squared of the fractures.

Once the DFN was built, a permeability calculation was performed. The permeability tensor calculation is based on the geometric methodology of Oda (1985). This approach can infer the equivalent porosity properties for each grid cell, based directly on the geometry and properties of the fractures within those cells, using the Darcy’s law and assuming a laminar flow between parallel plates.

The equation to calculate the **permeability** is:

$$\frac{Q}{A} = \frac{s^3}{12D} \cdot \frac{\delta h}{\delta l} \cdot \frac{\rho g}{\mu} \tag{10}$$

where Q is the flow rate, A is the cross-sectional area, s is the aperture, D is the fracture spacing, δl is the pressure head, ρ is the fluid density and μ is the fluid viscosity.

To estimate the permeability, first the fractures are clipped to conform to each geocellular volume (fracture fragments) and then approximated by polygons. The contribution to the permeability of each fracture is dependent on the area of the clipped polygon, on the aperture and orientation of the fracture. To calculate the permeability for that specific cell, the software sums the contribution of all the fracture fragments. The permeability is presented in Move® in different forms. Here the maximum and minimum values of the permeability for each volume will be show, along with the values of the tensor of the permeability *Kxx* and *Kyy,* to make a comparison with the available data on the study site (Panza et al., 2017).

The **porosity fraction** for a given grid cell is calculated as the ratio of the total fracture volume in a cell per cell volume:

$$\phi = \frac{\Sigma_{polygon} \ V_{polygon}}{V_{cell}} \tag{11}$$

where volume V of an individual fracture polygon is equal to its surface area times its aperture size.

The following Figure 17 and Figure 18 show the DFN obtained for the different fault volumes with the related parameters (see also Figure 15 and Figure 16 for reference).

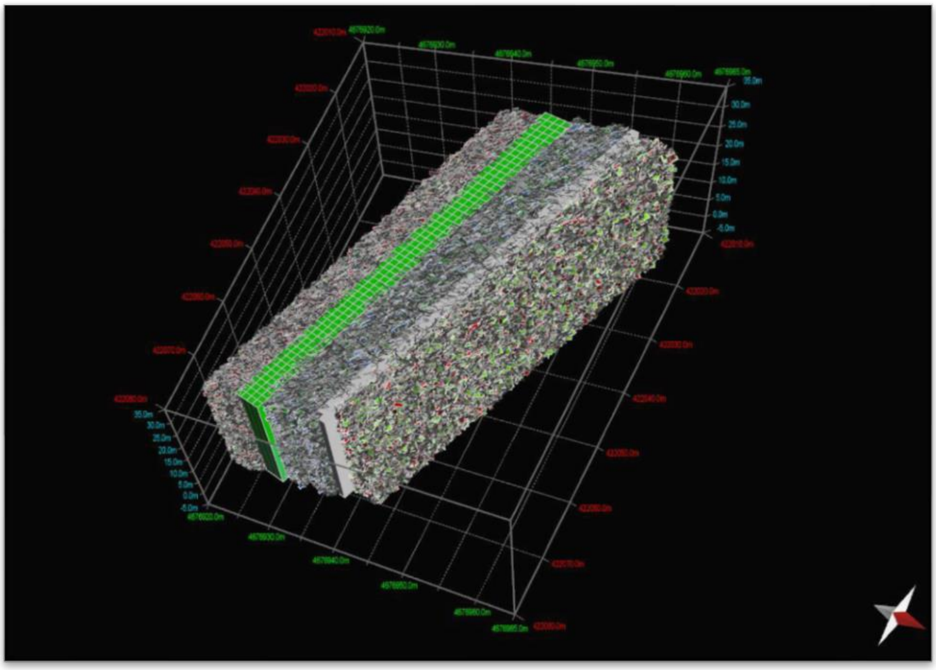

Figure 17. DFN generated for the northern sector of the fault. The green and gray blocks are the cores of the fault. Fractures in the damage zones have different colors relative to the different sets.

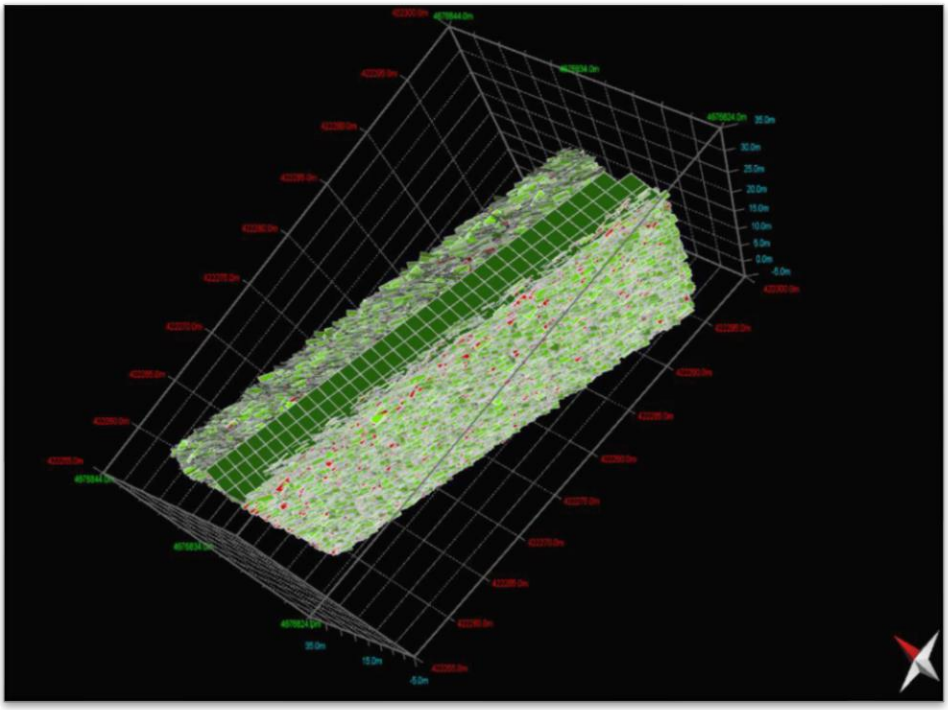

Figure 18. DFN generated for the southern sector of the fault. The grey block is the core of the fault. Fractures in the damage zones have different colors relative to the different sets.

Table 3. Parameters characterizing the fractures in the volumes generated for the southern and northern portion of the fault zone, moving from south to north.

	POROSITY (%)	PERMEABILITY (min and max) [mD]	PERMEABILITY Kxx (min-max) [mD]	PERMEABILITY Kyy (min-max) [mD]	P32 [1/m]
SOUTH ZONE					
Volume 1	0.87	644.877-953.562	434.066-659.217	345.645-516.27	8.4
Volume 2	1.34	986.656-1479.43	865.886-1304.53	301.965-469.495	12.76
NORTH ZONE					
Volume 1	1.12	830.522-1303.87	535.991-822.001	520.219-839.58	11.56
Volume 2	0.71	350.554-502.772	186.173-276.255	252.628-368.955	8.23
Volume 3	0.77	474.026-767.634	445.133-730.476	301.21-483.004	7.3

3.2 Modeling the fault zone

This part of the model was developed during the period as Visiting Scholar at the University of Illinois at Urbana-Champaign. Here, under the supervision of prof. Albert J. Valocchi, I collaborated with the Computational Earth Science Group of the Earth and Environmental Sciences Division of the Los Alamos National Laboratory (LANL).

The goal of the work is to simulate the flow of CO_2 with the entire fault zone, coupling the damage zones with the core of the fault. The LANL developed the open source software employed to set up the fracture model and run the fluid flow simulation.

The fault conceptual model is described in Figure 19. Because of the high degree of fracturing, the damage zones can be modeled by a discrete medium, while the core of the fault can be modeled as a continuum porous medium. One of the major challenges arising from this conceptual model is the coupling between the discrete of the damage zones and the continuum domain of the core, because of numerical continuity issues at the boundary between the two media.

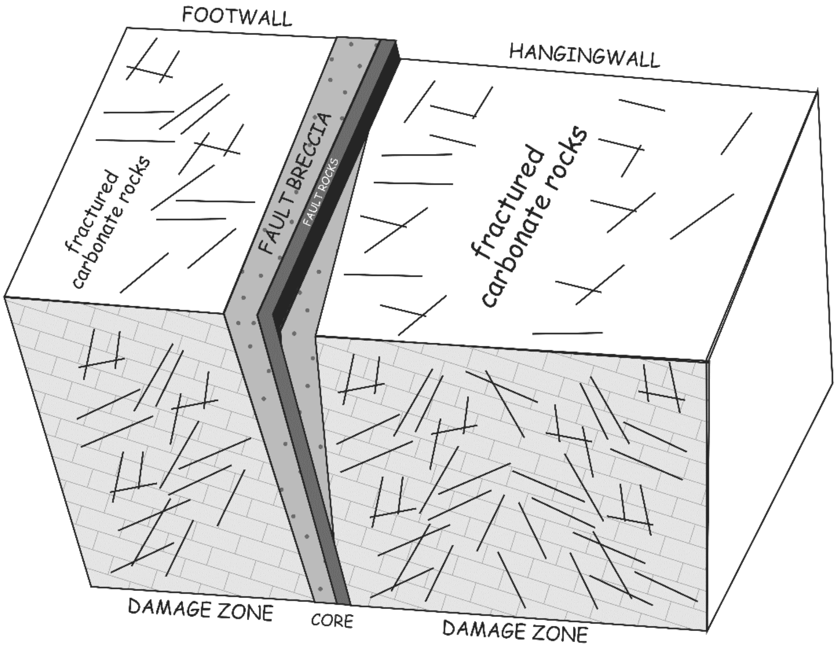

Figure 19. Conceptual model of the fault.

To ensure that continuity between the discrete and continuum domain is always satisfied, the modeling approach included the following steps:

1. Modeling the damage zone using the DFN approach at the scale of the fractures;
2. Characterize the effective permeability of the fracture networks;

3. Use the calculated parameters as input for the numerical simulation of fluid flow in the equivalent continuum medium representing the whole fault zone (core+damage zone);

The first two points from the construction of the DFN to their hydraulic characterization, are introduced in section 3.2.1 and section 3.2.2. The third point is discussed in 4. MODELING FLUID FLOW AT THE FAULT SCALE.

The DFN modeling of the hanging wall and footwall damage zones was performed using dfnWorks (Hyman et al., 2015), a parallelized computational suite, developed at LANL to generate three-dimensional DFN and simulate flow and transport at scales ranging from millimeters to kilometers. The software has three main modules: DFNGEN, DFNFLOW DFNTRANS. The workflow is summarized as in Figure 20:

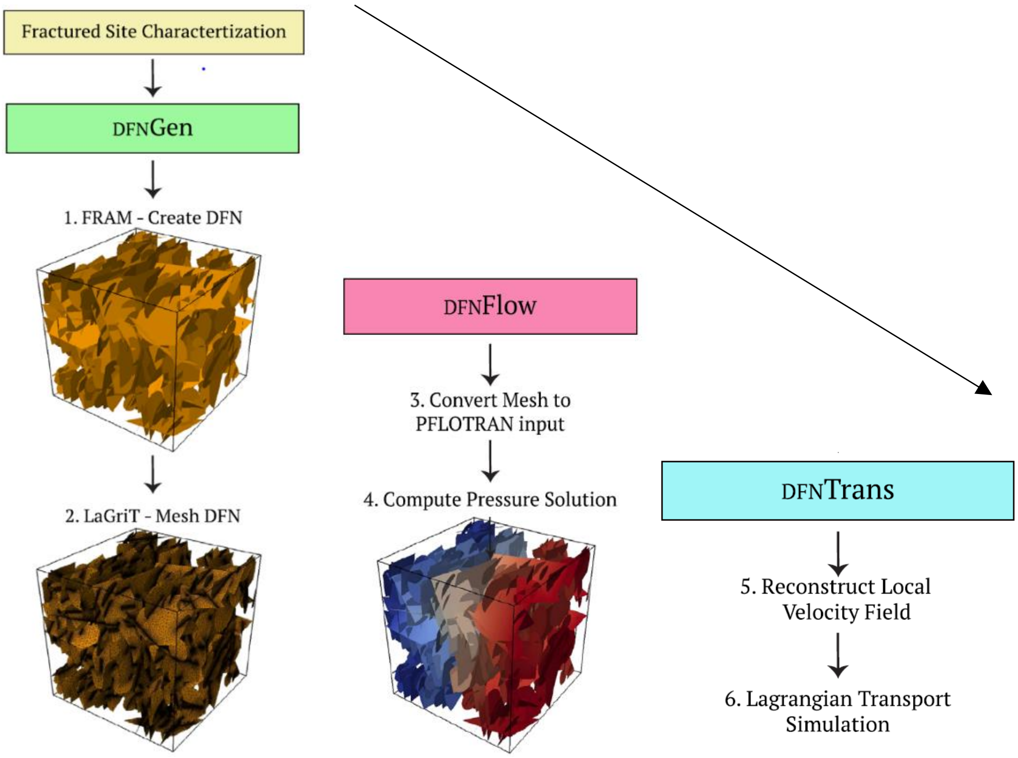

Figure 20. dfnWorks workflow (modified after Hyman et al., 2015).

The first module generates the fracture network and the meshing; the second one employs a flow solver (PFLOTRAN) to perform flow simulation on the meshed fracture network; the third module simulates transport by particle tracking using the solution obtained from DFNFLOW. Only the first two modules were used in the present study, since no transport simulation was performed.

3.2.1 DFNGEN

The parameters acquired in the field and their statistical properties were used to build the DFN model. In DFNGEN, fracture networks are considered as sets of two dimensional intersecting polygons embedded in a three-dimensional space. The spatial distribution among these planar surfaces can create arbitrary small features, like small intersections between two fractures, or the intersection of two parallel fractures with a third one. These “pathological cases” represent one of the major obstacles in modeling the flow through discrete fracture network, because resolving these small elements might have a strong impact in terms of the quality of the mesh and the computational cost. In fact, the mesh must be the same size or even smaller than the feature in order to properly simulate the physics of the problem. Most of the available methods (e.g. Koudina et al., 1998; Mustapha and Mustapha, 2007; Maryška et al., 2004) generate automatically the mesh that is then manually adjusted to improve its quality. Unfortunately, this method may cause distortions in the underlying network and the fractures may be no longer represented by planar surfaces.

To avoid these problems, DFNGEN uses the Feature Rejection Algorithm for Meshing (FRAM), described in Hyman et al., (2014), to construct a conforming mesh capable of solving all the features in the fracture system. The core of FRAM is the generation of a network with features equal or larger than a prescribed minimum feature size *h*. In this way, arbitrary small features are not included in the network, high quality conforming Delaunay Triangulation mesh naturally arises and no adjustments a posteriori are required.

Each fracture in the DFN is represented by a planar straight-line graph (PSLG) made up of a certain number of vertices defining a set of line segments, that represent the fracture boundary and the intersections with other fractures. For a single PSLG the minimum feature size *h* is the radius of the smallest circle (in three dimension of the smallest sphere) that intersects two non incident vertices of the PSLG (see Figure 17). FRAM requires that the DFN never generates a fracture PSLG with a feature size less than *h*. Multiple intersections are removed for convenience and simplicity.

The shape of the fracture can be a rectangle, or an ellipse represented by an N-vertex convex planar polygon. Each fracture is generated sequentially, and it is accepted in the network only if it does not form features less than *h*, otherwise it is rejected. It is possible to generate multiple fracture sets in the network, prescribing for each set their statistical parameters (e.g. shape, orientation, length). DFNs are generated for both the hanging wall and the footwall damage zones of the studied fault, based on the parameters acquired in the field.

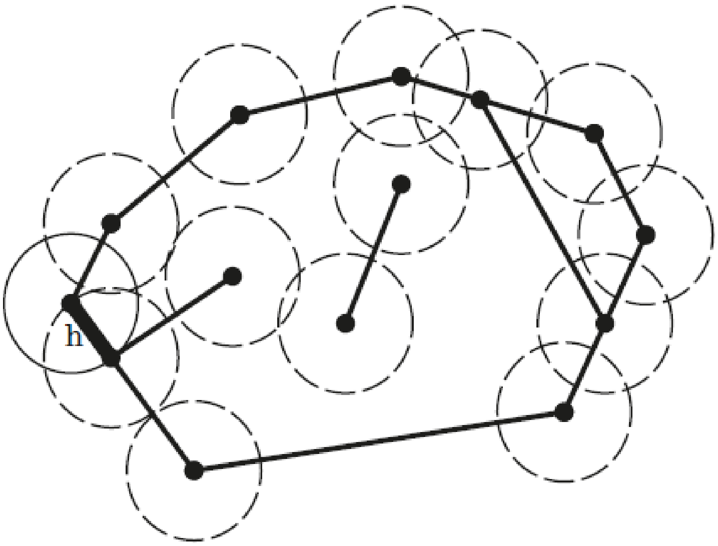

Figure 21. Possible PSLG configuration, showing the different kind of features, all larger than the minimum feature size h, occurring on the left boundary from (Hyman et al., 2014).

Once the DFN was created, a Delaunay Triangulation is generated in parallel for each fracture with the software LaGriT (http://lagrit.lanl.gov), guaranteeing the conformity to all the fracture segments. The cells of the mesh have variable length edge *O(h)* that is finer close to the fracture intersections and coarser moving away. The Voronoi Volumes, dual of the Delaunay Triangulation, are then constructed in a format that can be used as input to finite volume flow solvers like FEHM (Zyvoloski, 2007), TOUGH2 (Pruess, 1999), and PFLOTRAN (Lichtner, P., G. et al., 2015).

The most important parameters adopted for building the DFN and create statistically generated fracture networks are presented in Table 4. Most of these parameters come from the field investigation.

Table 4. Main input parameters used for the generation of the DFNs with DFNGEN for the hanging wall and footwall damage zones. The extension indicates if the parameter was applied to all the fracture sets or if it is different for each set. When specified, the order of the fracture set parameter is listed in the same way, to associate all the parameters to the same set.

Parameter	**Extension**	**HW**	**FW**
Domain size (m^3)	all	27	27
h (m)	all	0.005	0.005
nShape	all	ellipse	ellipse
easpect	all	1	1
Number of vertices	all	8	8
famProb	for each set	0.25, 0.10, 0.40, 0.25	0.35, 0.15, 0.25, 0.25
Number of sets	all	4	4
etheta	for each set	0.098π, 0.1π, 0.12π, 0.07π	0.18π, 0.07π, 0.13π, 0.09π
ephi	for each set	0.2π, 0.67π, 1.14π, 1.36π	0.16π, 0.56π, 1.08π, 1.4π
ekappa	for each set	14.95, 13.98, 28.2, 33.61	9.19, 14.84, 18.7, 24.17
PDF	all	Truncated power law	Truncated power law
emin (m)	for each set	0.08, 0.12, 0.02, 0.06	0.02, 0.07, 0.02, 0.07
emax (m)	for each set	1.4, 0.3, 1.75, 1.4	1.8, 0.5, 1.5, 1.4
ealpha	for each set	1.85, 1.46, 1.46, 1.24	1.75, 1, 1.48, 1.9
epowerLawReject	all	10	10
Aperture (m)	all	$7x10^{-4}$	$7x10^{-4}$

The DFN was built by respecting the following rules:

1. The domain size was chosen to be large enough to be a representative volume of the damage zones, considering the distribution of the sizes (mostly less than 300 cm) of the fractures and the computational cost, since the larger the volume, the larger the time necessary to populate the domain.
2. The minimum feature size *h* was chosen after a series of trail-and-error tests, in order to reject only the smallest number of fractures possible, keeping the values of the P32 inferred from field data and taking into account the statistical distribution of fracture sizes, showing both for the hanging wall and the footwall a large fraction of fractures of the order of few centimeters (see Figure 6). Therefore, imposing *h* one order of magnitude smaller than the order of magnitude of the size of the fractures, ensured the inclusion of possible small features occurring in the fracture network, since the mesh is *O(h).*
3. The shape of the fractures (*nShape*) was imposed as elliptical, using 8 vertices.
4. The probability of occurrence of each family of random distribution ellipses (famProb), should add up to 1.0 (100%). The fractures are generated for each set according to the imposed probability. Since the algorithm implemented in FRAM can produce an over-rejection of larger fractures that consequently cannot be correctly represented in the DFN (see Hyman et al. (2014) for details), I imposed that sets with fractures larger in size have a higher probability to be included in the DFN.
5. Four sets of fractures were created for both the hanging wall and the footwall damage zones, according to the orientation of the sets found from the field data. The orientation of each set is expressed in radiant as:
6. -*etheta*: the angle the normal vector makes with the z-axis;
7. -*ephi*: the angle the projection of the normal onto the x-y plane makes with the x-axis;
8. Fisher's $\boldsymbol{k}$ distribution parameter is expressed for each set of fractures as *ekappa*.
9. A truncated power law was chosen as probability density function, following the distribution of the fracture size inferred from field data. The required parameters that must be used as input are the minimum radius of the fractures (*emin*), the maximum radius (*emax*) and the exponent of the PDF (*ealpha*). Considering an aspect ratio

(*easpect*) equal to 1, the range of the radius were directly calculated from the range of the diameter (Table 2)

10. Another parameter that can be selected is the maximum number of rejections of one fracture of a given radius, before its radius is decreased. This value was imposed for all the fractures equal to 10, as suggested in the tutorial of the software.
11. The aperture of the fractures was imposed constant, regardless of their size, using a mean value obtained from the field data and from literature data (Agosta et al., 2010).

To have a good representation of the fracture systems, one hundred realizations were performed for the damage zones. Figure. 18 shows one of the realizations generated for the hanging wall damage zone of the fault. Representative parameters for the realizations in the hanging wall and footwall damage zones are presented in Table 5.

Table 5. Representative parameters for the statistic realizations of the fracture networks of the hanging wall and footwall damage zones

	Total number of fractures	P32	Fracture Porosity (P33)
HANGING WALL	2066	8.1	0.005
FOOTWALL	2071	6.3	0.0045

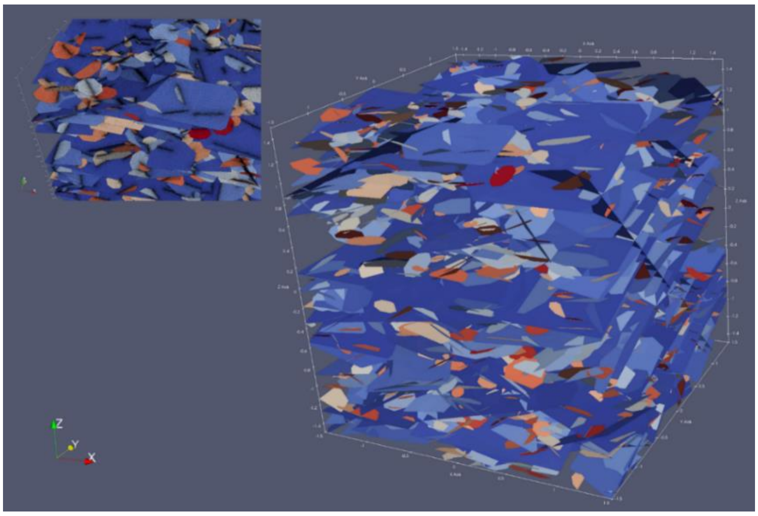

Figure 22. DFN realization for the HW damage zone. In the left upper corner, a detail of the figure including the meshing.

3.2.2 DFNFLOW

Once the DFN were generated with DFNGEN, a Python script prepares the output from DFNGEN to be suitable by the flow solver in DFNFLOW. The flow solver used in the present study is PFLOTRAN. PFLOTRAN is an open source, massive parallel, subsurface flow and reactive transport code, solving a system of generally nonlinear partial differential equations describing multiphase, multicomponent and multiscale reactive flow and transport. PFLOTRAN requires in input the explicit unstructured grid of the Voronoi mesh, including the locations of the Voronoi cell centers, the connectivity of the cell-centers and the cell areas. The software determines the steady state pressure field within the DFN using a two-point flux based finite volume scheme. Some of the currently available subsurface flow processes available in PFLOTRAN are: solution of Richards equations, non-isothermal two phases water supercritical CO_2, general mode for multiphase flow of any two component systems. In the dfnWorks workflow, PFLOTRAN returns the fluid fluxes (Darcy velocities) at the edges of the Voronoi control volumes. For each DFN realization, the flow is simulated along the three main directions *x*, *y*, *z*, to calculate the tensor of the permeability. Appropriate boundary conditions are imposed to produce a flow parallel to each direction, using a gradient of pressure. In Figure 23 an example of flow in the fracture network in the *z* direction, imposing a pressure of 1.5 MPa at the bottom of the domain and a pressure of 1 MPa at the top.

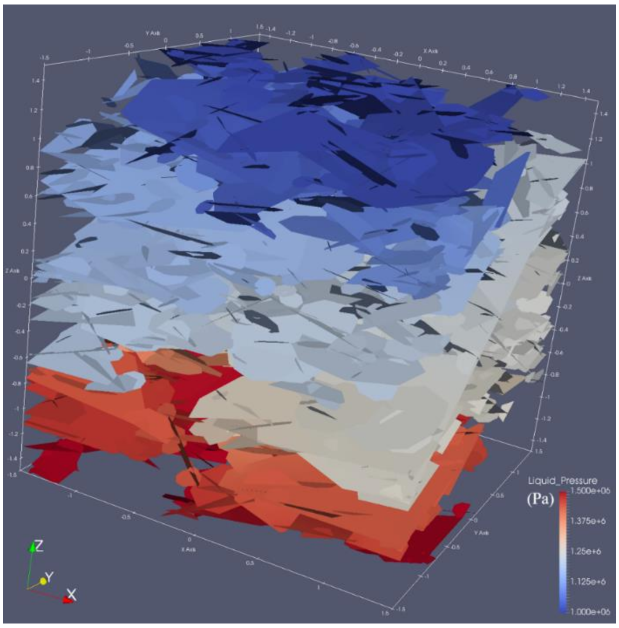

Figure 23. Liquid pressure variation in one of the realizations for the HW damage zone.

4. MODELING FLUID FLOW AT THE FAULT SCALE

4.1 Underground geological storage of Carbon Dioxide

Global mean surface temperatures have undergone a significant rise over the period from 1880 to present. Carbon dioxide (CO_2) is an important heat-trapping (greenhouse) gas, which is released through human activities such as deforestation and burning fossil fuels, as well as natural processes such as respiration and volcanic eruptions. The increase in the content of CO_2 in the atmosphere has been addressed as one of the causes of the temperature increase of global mean surface temperature: 406.94 ppm of CO_2 were measured in August 2017 at Mauna Loa Observatory, Hawaii (data from NASA).

Carbon Capture and Storage (CCS) has been proposed as one of several methods for keeping atmospheric greenhouse gas emissions at an acceptable level whilst meeting global energy requirements (Pacala and Socolow, 2004). CCS techniques consist of capturing CO_2 from major stationary sources (e.g. power stations), transporting it usually by pipeline to an adequate storage site and then injecting it into a suitable underground geological formation, in order to be trapped for a long period of time. The main targets for geological storage are depleted oil and gas reservoirs (possibly coal formations) and deep saline formations. There are many published studies of the cost of capturing and compressing CO_2 and several generic studies of the cost of transport and storage (Metz et al., 2005)

Information and knowledge gained from injection and/or storage of CO_2 from a large number of existing enhanced oil recovery (EOR), as well as form the Sleipner (3000 t/day), Weyburn (3-5000 t/day) and In Salah (3-4000 t/day) projects, indicate that it is feasible to store CO_2 in geological formation as a CO_2 mitigation option to contrast the accumulation of this greenhouse gas in the atmosphere. Injecting CO_2 into deep geological formations at carefully selected sites can store it underground for long periods of time: it is considered likely that 99% or more of the injected CO_2 will be retained for 1000 years.

To geologically store CO_2, it must be first compressed usually to a dense fluid state known as “supercritical”. In fact, at depths below 800-1000 m, supercritical CO_2 has a liquid-like density that is easily stored in the pores of sedimentary rocks with different mechanisms. CO_2 injection into subsurface geological formations causes change in the state of the system, with changes in the local pressure and fluid saturation. To select the best place for storage purposes, it is important to be able to understand, monitor and manage such to guarantee the safety of the site. In fact, one of the concerns raised about storage is the possibility of leakage in the short and long term. In a geological CO_2 storage site, the main migration pathways in case of leakage would be compromised boreholes or gas permeable faults. Real field test sites have a fundamental value, since they enable the development and demonstration of the best practices for the entire storage cycle, from site characterization to operation, including monitoring and mitigation/remediation of leakage.

In tests conducted in the CCS research, both CO_2 and water have been injected at different depths:

- Shallow injections: <2 m
- Moderate: 10-100 m, but typically <20m
- Deep: >800 m

Usually deep injections are pilot projects, having a research objective and where less than 100.000 tons of supercritical CO_2 are injected into the subsurface, typically over a few years. Shallow and moderate injections have the aim to observe the flux of CO_2, to test the monitoring systems and to study the impact of the CO_2 on the groundwater and the ecosystem.

All over the world, tests sites have been performed in shallow and moderate depths, especially in Europe and mostly onshore. The parameters that characterize an injection site test include: the duration of the experiment, the amount of CO_2 injected and the rate of the injection. The duration of the injection varies from a minimum of few hours (Maguelone test site, Montpellier, France) up to 455 days (ASGARD test site, Nottingham, UK). The highest injection rates characterize the shallower sites, for example:

- Ginninderra (Australia), three injection tests:
  - 51 kg/d from February to May 2012,
  - 77 kg/d from October to December 2012
  - 51 kg/d from October to December 2013;

- ASGARD, two injection tests:
    - 34 g/d injected from May to September 2006
    - 11 kg/d from March 2011 to June 2012;

Most of the injection tests have been performed in porous media, characterized only by a primary porosity. The most important test sites where CO_2 have been injected in fractured media (secondary porosity) are:

- SIENA GRABEN (Italy)
    - the injection well is located at 25 m of depth, with an injection rate varying in time from 34 to 70 kg/d for 0.1 day.
- INAS (Fukuoka, Japan)
    - this test was performed at around 100 m of depth, with a very high injection rate, 1189 kg/d, for a short period of time, 0.1 day. This was the first test ever performed in volcanic fractured rocks.
- LATERA (Italy)
    - this test site was conducted at 9-12 m of depth in a fault zone, with an injection rate of 10 kg/d of CO_2, for 0.25 day.

Usually, the CO_2 is injected through a well drilled to a specific depth with different inclinations according to site conditions. A series of monitoring wells and/or a geophysics network close to the injection area, monitor the behavior of the reservoir to the dispersion of the CO_2 plume and the impact of the injection on the quality of the groundwater. Figure 24 shows an example of configuration for an injection test site.

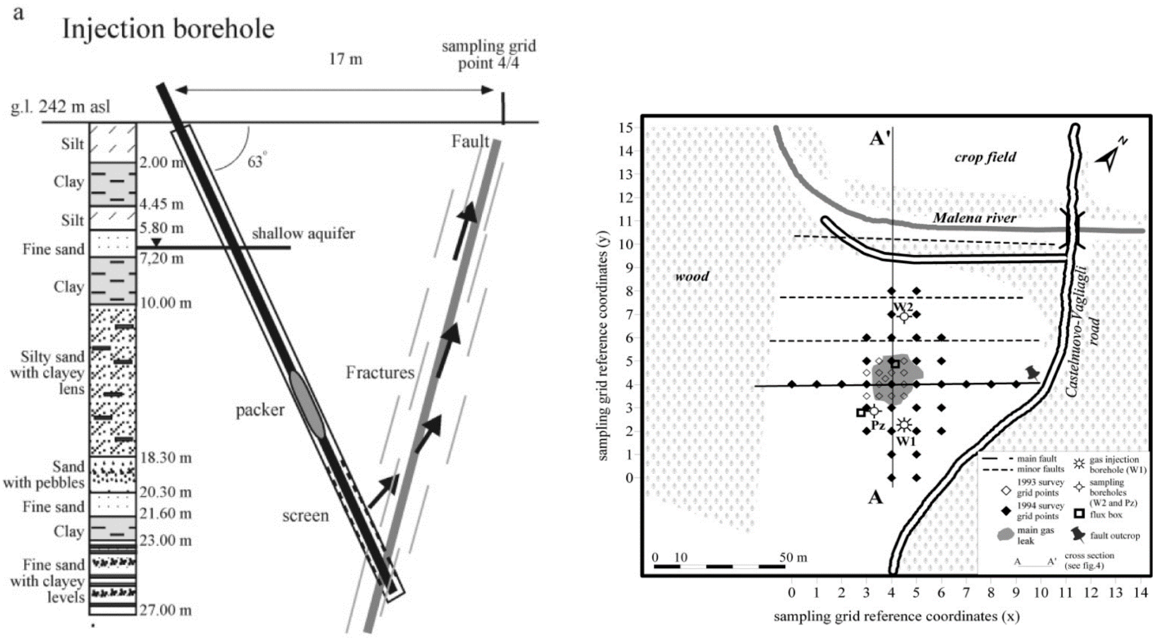

Figure 24. Injection test performed in the Siena Graben. On the left the section of the injection site; on the right the map of the monitoring area. The injection happens close to the fault plane to monitor how the fault behaves to the migration of the CO_2 (Modified after Ciotoli et al., 2005).

4.2 Modeling pipeline

In the next paragraphs, the methodology used to model the fluid flow at the scale of the bulk fault is described, to study the behavior of all its component to the migration of the CO_2. The presented workflow was customized with the Los Alamos National Lab Group of in Earth & Environmental Sciences Division (EES-16) to be applied to a similar study case. All the PYTHON scripts described were built in to reproduce the conceptual model of the fault zone (Figure 19) and its properties.

The fluid flow simulations were performed in the fault domain with the software PFLORTRAN. PFLOTRAN input file is called CARD and is based on keywords. Each keyword specifies all the components and conditions that characterize the simulation. Initial and boundary conditions and material properties are assigned to spatial regions using a coupler approach: for example, initial and boundary conditions (keyword CONDITION) are assigned to regions (keyword REGION) using keywords INITIAL_CONDITION and BOUNDARY_CONDITION (see PFLOTRAN User’s manual). The main keywords used to perform the simulation will be described. A card is organized in blocks and sub-blocks, grouping keywords that work together. Two cards were built to run the simulations: the *CARD 1* (Table 9) describes the “Steady state simulation” (see paragraph 4.4.1 Steady state simulation), while the “CO_2 injection” is described in the PFLOTRAN *CARD 2* (Table 10) (see paragraph 4.4.2 CO2 injection). The results of the first simulation (*CARD 1)* were used as initial condition for the second simulation (*CARD 2),* where the actual injection of CO_2 in the footwall of the fault was modeled. This pipeline was used for the first time and this contributed to development and debug of the available codes.

4.3 Upscaling the small-scale properties

Modeling the fluid flow at the fault scale requires addressing two main problems:

1) Measure large scale permeability directly;
2) Coupling the fractured media of the damage zones with the continuum media of the core, according to the conceptual model adopted to describe the fault zone;

Discontinuum models can provide a framework to estimate large-scale continuum properties. The basic assumption underlying this approach is that fracture density is large enough that nearly all the fractures contribute to the effective permeability. Snow (1965) and then Oda (1985) and Oda et al., (1987) developed analytical formulations to relate fracture geometry (frequency, orientation, length) to larger scale hydraulic properties. This method is one of the most used for this kind of calculation, but it is limited by the difficulty of obtaining representative estimates of hydraulic apertures and because of it does not consider the connectivity of the fractures. To resolve this limitation, several authors (e.g. Long et al., 1982; Robinson, 1984; Dershowitz, 1984; Hudson & La Pointe, 1980; Cacas et al., 1990) developed an approach to estimate continuum properties from discrete models of fluid flow in fracture networks.

In the present study this hybrid approach was used, building continuum approximation of discrete fracture networks. In fact, the high values of the parameter P32 (fracture density) found for the fracture system (see

Table 3) allow us to approximate the properties characterizing the two damage zones with an equivalent continuum. This upscaling to an equivalent continuum allowed also to couple the damage zones previously treated as a discontinuum domain with the core considered a continuum. In this way the power of both the approach is employed. First, using the DFN to appropriately characterize the hydraulic properties of the fracture network and then reducing the geometric complexity of flow patterns in the fractured rock mass to a continuum medium, easier to implement at the scale of the fault from a mathematical point of view. Different domains have been created, representing the different component of a fault zone, following the conceptual model described in Figure 21, different domains have been created, representing the different component of a fault zone. The total domain size reflects the real *x, z* dimension of the Roman Valley Quarry where the fault is exposed, that is approximately 30 m wide (x), 80 m long (y) and 25 m high (z). The *y* direction has been reduced to half, to contain the computation cost, considering the symmetry of the conceptual model in that direction.

The relative dimensions of the hanging wall and footwall damage zones have been chosen according to the model of evolution of the fault zone of the Roman Valley Quarry described in Agosta et. al (2009). The mature stage of the fault (Figure 20) occurred along the SW and NE faults exposed in the quarry. Strain localized around the main slip surfaces, causing also the intense brecciation and fragmentation and cataclastic deformation of the fault cores, as thick as 1 m. The fault cores were flanked by damage zones characterized by opening mode failure, dilation of favorably oriented pre-existing elements and minor faulting. The damage zones are asymmetric relative to the hanging wall, and more developed in the hanging wall than the footwall (Berg and Skar, 2005).

A PYTHON script generates the geometry of the integration domain according to the distance from the origin of the axes, whose *(x,y,z)* coordinates are (0,0,0), using for the different components of the fault zone, the proportions as from the conceptual model in Figure 20. The script assigns for each domain of the fault an identification number (*material id),* to appropriately associate the hydraulic properties appropriately. The fault dips ~78˚, accordingly to the field data.

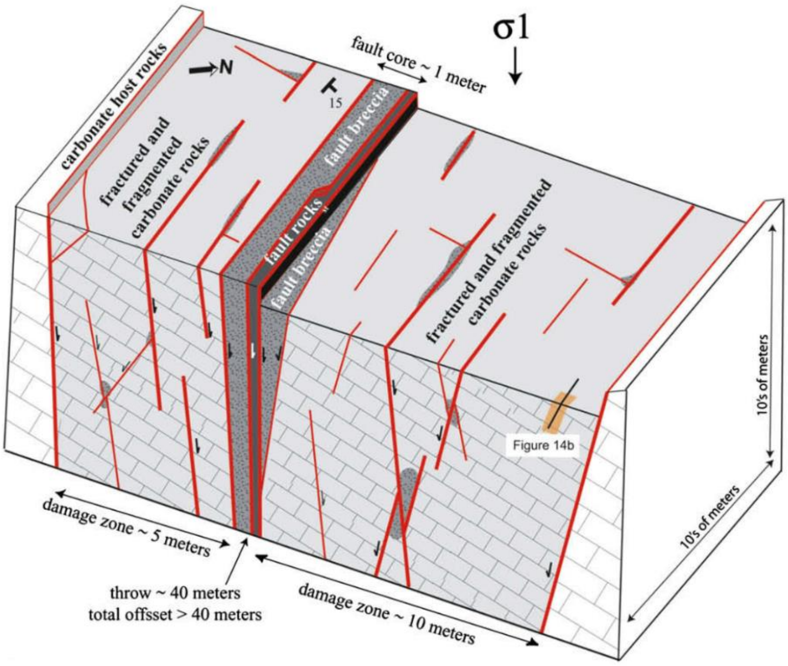

Figure 25. Conceptual model of oblique normal faulting in the mature stage (modified after Agosta et al., 2009).

Figure 26 shows the different domains of the fault (*material ids*), in different colors: blue represents the host rock, red and light blue are the hanging wall and footwall damage zone respectively, while the light orange domain is the core of the fault. To resolve the core of the fault zone appropriately, the mesh is a structured grid with cubes of 25 cm of side.

For each *material id*, permeability and porosity values have been assigned to characterize the hydraulic parameters of this equivalent continuum. In a conventional equivalent continuum, where individual fractures are not more treated explicitly, the heterogeneity of the fractured rock is modeled by using a limited number of regions with uniform hydraulic properties (i.e. permeability and porosity), representing the volume-averaged hydraulic behavior of the fractures. The properties of the rock mass can be treated from either a deterministic or stochastic approach. In the present study a stochastic approach was used, with the tensor of the effective permeability treated as a spatially variable random field, characterized by a probability distribution for each of the main directions of the tensor: (K_{xx}, K_{yy} and K_{zz}).

The first step was the calculation of the distribution of the permeability of the fractures characterizing the damage zone. Once the Darcy velocities have been computed for each DFN realization with DFNFLOW, a PYTHON script calculates the permeability component of the permeability tensor for the fracture systems. The script takes as input the geometry of the DFN boundary we are interested in calculating the permeability, (e.g. the face boundary of the domain in the x direction) and the computed Darcy velocities for the fractures along the same direction. Then it performs a mass balance and calculates the effective permeability along the specified boundary, in the direction of flow. This procedure is repeated for all the main direction obtaining the components of the tensor of the permeability in the principal directions*: Kxx, Kyy, Kzz*. Figure 23 shows the distribution of the calculated effective permeability in each direction for all the DFN realizations

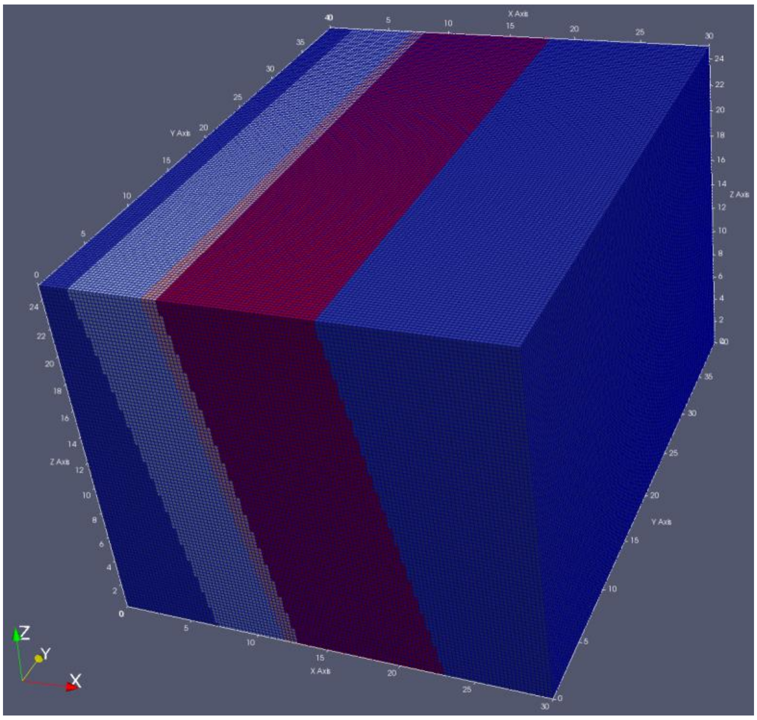

Figure 26. Continuum domain representing the whole fault zone. The different colors refer to the different material ids (see text for explanation).

The tensor of the permeability shows a Gaussian distribution: the maximum values (~10^{-10} m^2) are distributed along the *x* and *y*, while the minimum values (~10^{-11} m^2) are found along the z direction in the order of (~10^{-11} m^2), (Figure 27).

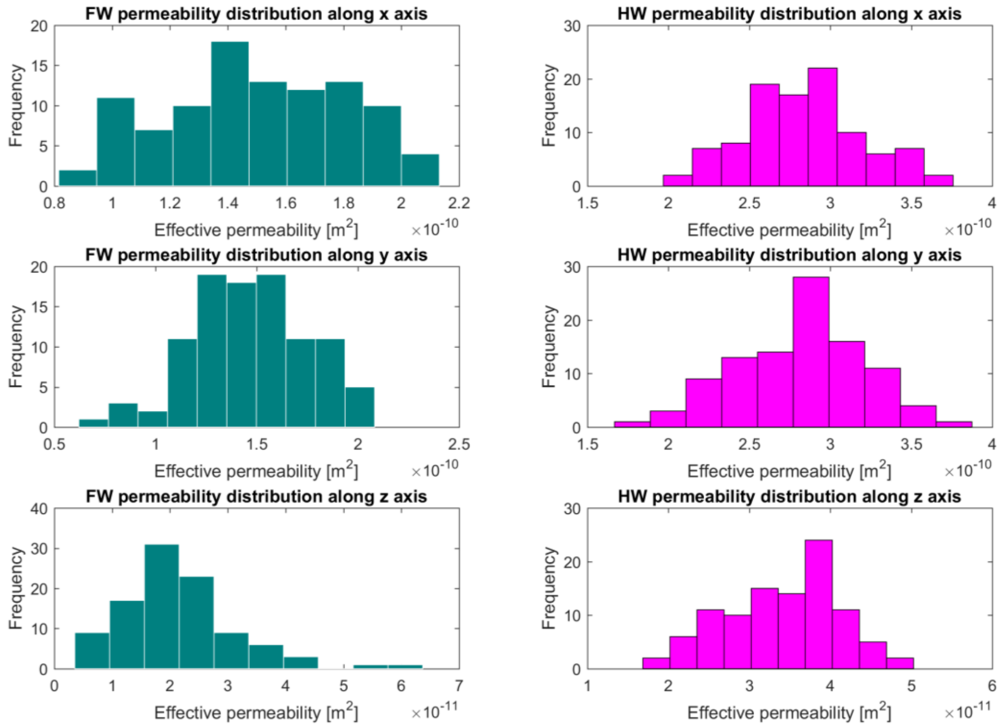

Figure 27. Permeability distribution along the three main directions for all the DFN realizations in the hanging wall and footwall damage zones.

To assign to each cell the appropriate permeability and porosity, a PYTHON script takes as input the location of the *material ids*, the distribution of the permeability for each direction and the porosity of the different domains (see Figure 27):

- The permeability (Figure 28) is assigned based on the different *material ids.* For the host rock and the fault core, considered continuum media, a constant value of the permeability is assigned to each cell. These parameters are taken from the results of the analysis conducted on samples of carbonate fault rocks (see Agosta et al., (2007)):

- host rock: 6.77×10^{-19} m^2
- fault core: 9.67×10^{-20} m^2

These values have been selected considering that the host rock permeability is not affected by the interconnecting systems of fractures that can contribute to increase the permeability, but it is rather characterized far from the fault by a background deformation (i.e. pressure solution seams and deformation bands; Agosta et al., 2009). The value for the fault core has been selected considering the case of a cemented fault rock.

For the *material ids* representing the damage zones, a value of permeability is assigned to each cell by picking up iteratively a random number from the distribution of the values in each direction (Figure 27), obtained from the DFN realizations. Using this approach, the properties of the DFN are upscaled to characterize the ones of the equivalent continuum medium in the domain of the damage zones of the fault.

- The porosity (Figure 29) is a constant value assigned based on the *material id*:

- host rock: 5%
- damage zones: 0.45%
- fault core: 0.6 %

The porosity for the host rock is a conservative value, at the lower end of the range that characterizes most of the grainstones beds of the Bolognano Formation (5% to 20%, Agosta et al., 2010). The value for the damage zones is taken from the medium value found for the fracture porosity (P33) of the DFN modeling. Finally, the porosity value for the fault core is taken from Agosta et al., (2009).

Once the properties of the equivalent continuum domain were defined, the next step was the simulation of fluid flow at the scale of the fault. We investigated the behavior of the different components of the fault after the injection of CO_2. This modeling approach can help in the characterization of potential reservoirs for storage purposes, in the context of Carbon Capture & Storage (CCS) techniques.

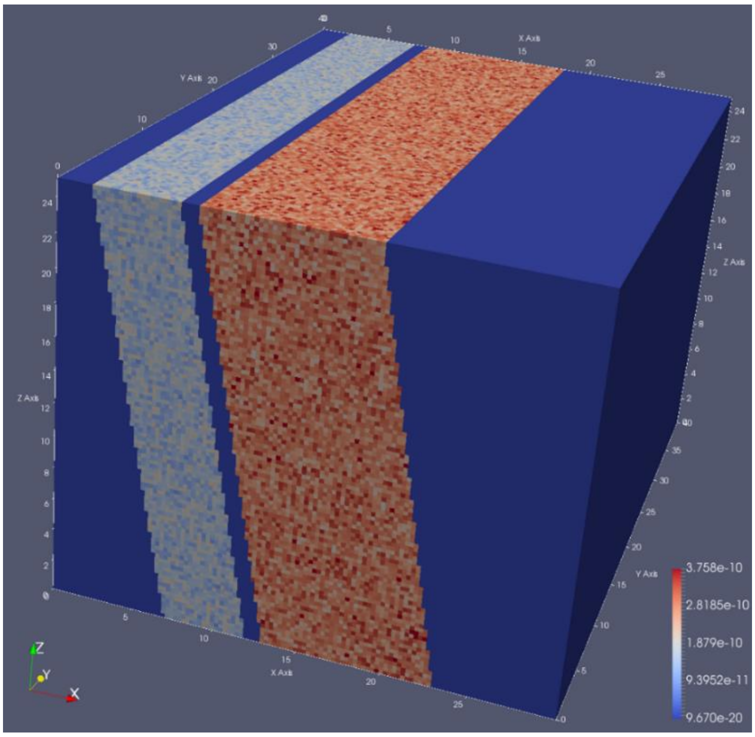

Figure 28. Distribution of the permeability (m^2) in the different domain of the fault.

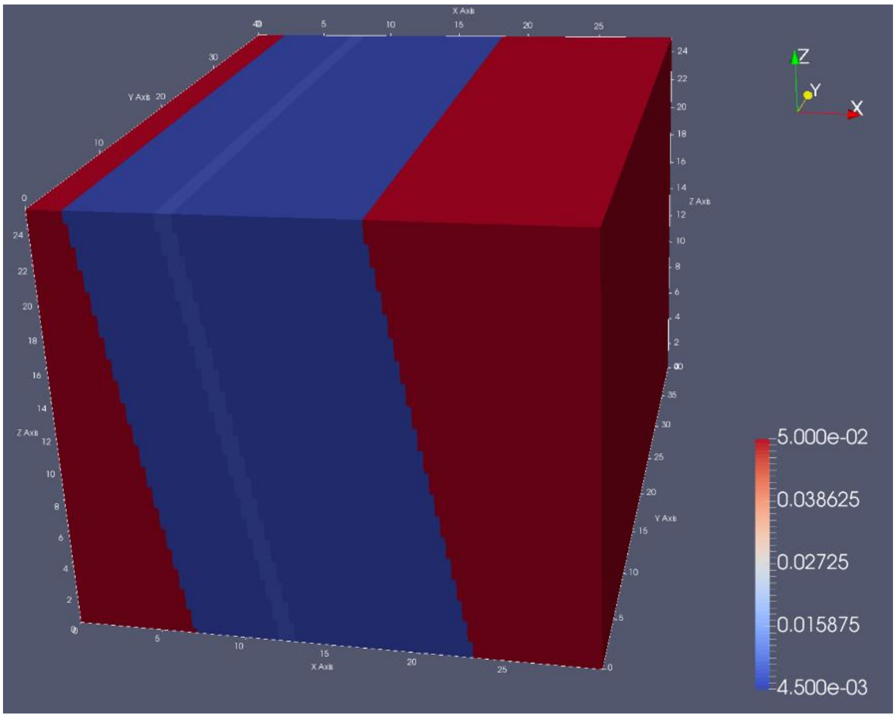

Figure 29. Distribution of the porosity in the different domains of the fault.

4.4 Fluid flow simulations

4.4.1 Steady state simulation

The PFLOTRAN *CARD 1* is described. In this card the simulation was performed to reach a "steady state initial condition" to be used as initial condition for the simulation of injection of the CO_2, described in *CARD 2*.

✧ *Section "flow mode"*

The section "flow mode" in the input card contains the information relative to the kind of simulation that is performed (i.e. the equations solved in the numerical model).

<u>KEYWORD → MODE</u>: determines the flow mode

The GENERAL mode was chosen to perform the simulation. This mode involves the solution of the coupled partial differential equations describing the two phases liquid-water flow (reactive and transport mode). The code solve the coupled system of mass conservation (12), energy (13) and flow (Darcy's law; 15) for the liquid and gas-phase:

$$\frac{\partial}{\partial t}\varphi\left(s_l\rho_l x_i^l + s_g\rho_g x_i^g\right) + \boldsymbol{\nabla}\cdot\left(\boldsymbol{q}_l\rho_l x_i^l + \boldsymbol{q}_g\rho_g x_i^g - \varphi s_l D_l\rho_l\boldsymbol{\nabla}x_i^l - \varphi s_g D_g\rho_g\boldsymbol{\nabla}x_i^g\right) = Q_i \tag{12}$$

Where we have the liquid and gas saturation $s_{l,g}$, density $\rho_{l,g}$, diffusivity $D_{l,g}$, Darcy's velocity $\boldsymbol{q}_{l,g}$, and mole fraction $x_i^{l,g}$.

The energy conservation equation has the form:

$$\sum_{\alpha=l,\,g}\left\{\frac{\partial}{\partial t}\left(\varphi s_\alpha\rho_\alpha U_\alpha\right) + \boldsymbol{\nabla}\cdot\left(\boldsymbol{q}_\alpha\rho_\alpha H_\alpha\right)\right\} + \frac{\partial}{\partial t}\Big((1-\varphi)\rho_r C_p T\Big) - \boldsymbol{\nabla}\cdot\left(\kappa\boldsymbol{\nabla}T\right)\Big) = Q \tag{13}$$

As the sum of contributions from liquid and gas fluid phases and rock, with internal energy U_α and enthalpy H_α of fluid phase α, rock heat capacity C_p and thermal conductivity κ (from Somerton et al., 1974) expressed as:

$$\kappa = \kappa_{\text{dry}} + \sqrt{s_l}\left(\kappa_{\text{sat}} - \kappa_{\text{dry}}\right) \tag{14}$$

where k_{dry} and k_{sat} are dry and fully saturated rock thermal conductivities.

The Darcy velocity of the α^{th} phase is equal to:

$$\boldsymbol{q}_\alpha = -\frac{kk_\alpha^r}{\mu_\alpha}(\boldsymbol{\nabla} p_\alpha - \gamma_\alpha \boldsymbol{g}), \quad (\alpha = l, g) \tag{15}$$

where $\boldsymbol{g}$ denotes the acceleration of gravity, k denotes the saturated permeability, k_α^r the relative permeability, μ_α the viscosity, p_α the pressure of the α^{th} fluid phase, and:

$$\gamma_\alpha = W_\alpha \rho_\alpha \tag{16}$$

with W_α the gram formula weight of the α^{th} phase:

$$W_\alpha = \sum_{i=w,\,a} W_i x_i^\alpha \tag{17}$$

where W_i refers to the formula weight of the i^{th} component.

The main OPTIONS applied to the GENERAL MODE are:

GAS_COMPONENT_FORMULA_WEIGHT: specifies the molecular weight; in this case it is relative to the Carbon Dioxide, being equal to 44.0095 g/mol.

-ISOTHERMAL: disables the energy calculation.

KEYWORD → CHECKPOINT: defines checkpointing options for restart capabilities. Checkpoint files enable the restart of a numerical experiment at any discrete point in a simulation where a checkpoint file has been printed. A file named restart.chk will also be written when PFLOTRAN properly terminates a simulation. Check-pointing can be used to start a new simulation from an initial steady-state solution.

PERIODIC TIMESTEP: 2 d specifies a time interval for checkpoint file output (d stays for day)

TIMES: d 6. 8. 10. 12. 14 16. 18. 20. specifies the points in times where checkpoints file output is desired, with the time units (days).

✧ *Section "discretization"*

This section includes information relative to the domain are set.

KEYWORD → GRID: defines the discretization scheme, the type of grid and resolution and the geometry employed in the simulation. The required input parameters are described.

TYPE: structured.

This means that a regular grid is used for the tessellation of the space.

NXYZ: 59 19 9

is the number of cells in the *x,y,z* direction.

BOUNDS: 0 0 0 <x_{min}, y_{min}, z_{min}>

30 10 5 <x_{max}, y_{max}, z_{max}>

To shorten the computational time, the simulations were performed with a coarser mesh, in a reduced domain. The main reason was the time necessary to complete the simulation on the computer I used because of the number of nodes involved and the difficulties encountered in running the simulation in parallel. The original number of nodes for the original full mesh domain was ~1 million. Coarsening the mesh allowed me to reduce the nodes of two orders of magnitude (~ten thousand). The mesh was still dense enough to resolve adequately the core, that is the smallest region of the integration domain. The reduction of the dimension of the domain was made in the *y* and *z* direction, in order to preserve the boundaries and the proportions between the different components of the fault zone in the *x* direction.

✧ *Section "solver options"*

KEYWORD → NEWTON SOLVER: specify nonlinear equations solver for the flow simulation.

✧ *Section "data sets"*

KEYWORD → DATASET: specifies the input data set for the parameters of the simulation. The dataset includes data for Permeability and Porosity, stored in the FILENAME *.h5*.

The Permeability is specified as an anisotropic tensor, with different values in the main directions *x, y, z*.

✧ *Section "fluid properties"*

Section with fluid parameters, e.g. the diffusion coefficients. In this case, the diffusion coefficient is zero for both the liquid and gas PHASE, because of the approximation of immiscible fluids.

KEYWORD → EOS: defined the equation of state for a simulated fluid.

EOS WATER

DENSITY EXPONENTIAL: reference density (tho0=996.629 kg/m^3), reference (p0=101320 Pa = 1 atm), compressibility (4.45×10^{-10}).

Exponential function= rho0*exp(compressibility*(pressure-p0)).

VISCOSITY CONSTANT: dynamic viscosity = 8.5077×10^{-4} Pa·s

ENTHALPY CONSTANT: 1.8890×10^{6} J/kmol

EOS GAS (CO_2)

VISCOSITY CONSTANT: dynamic viscosity = 16.1×10^{-6} Pa·s

✧ *Section "material properties"*

KEYWORD→MATERIAL_PROPERTY: material properties to be associated with a region in the problem domain, in this case called "soil".

POROSITY: it is taken from the DATASET Porosity.

PERMEABILITY: ANISOTROPIC, since an anisotropic tensor of permeability is defined in DATASET.

Additional OPTIONS added to the block are:

CHARACTERISTIC CURVES: SF1, defined here, but described and specified in the following section.

SOIL_REFERENCE_PRESSURE: 101320 Pa, is the reference pressure for soil matrix compressibility function.

TORTUOSITY: 1

✧ *Section "saturation function"*

This section specifies relative permeability, saturation functions and additional parameters to be associated with a material property.

Capillary pressure-saturation function

KEYWORD→CHARACTERISTIC CURVES: SF1 (defined in the previous section)

The capillary pressure is the difference in phase pressure between two phases in contact with each other. It depends on the interfacial tension between the two phases and is a function of phase saturation. Capillary pressure is related to the effective liquid saturation by the Van Genuchten and Brooks-Corey saturation function.

SATURATION FUNCTION: BROOKS_COREY

LAMBDA: 1.0121, the Brooks-Corey lambda parameter

ALPHA: 1.142×10^{-6}, the Brooks-Corey alpha parameter (Pa^{-1})

In the multiphase formulation, s_e is described in terms of effective liquid saturation s_{el}. Liquid saturation is obtained from the effective liquid saturation by

$$s_l = s_{el}s_0 - s_{el}s_{rl} + s_{rl} \tag{18}$$

where s_{rl} denotes the liquid residual saturation and s_0 denotes the maximum liquid saturation. The gas saturation can be obtained from the relation:

$$s_l + s_g = 1 \tag{19}$$

The effective gas saturation s_{eg} is defined by the relation:

$$s_{eg} = 1 - \frac{s_l - s_{rl}}{1 - s_{rl} - s_{rg}} \tag{20}$$

where s_{rg} is the gas residual saturation.

The Brooks-Corey saturation function is in the form:

$$s_e = \left(\frac{p_c}{p_c^0}\right)^{-\lambda} \tag{21}$$

with λ=mn and inverse relation

$$p_c = p_c^0 s_e^{-1/\lambda} \tag{22}$$

where m, n and p_c^0 (renamed α) are empirical constants determined by fitting to experimental data. Equation (22) is a special form of the Van Genuchten (1980) relation for $\frac{p_c}{p_c^0} \gg 1$.

The parameters used to define the Brooks-Corey saturation function in the present study are taken from literature data on carbonate rocks (Lian et al., 2016). Lian et al., (2016) followed a new method to interpret evaluate the water saturation more accurately. In this method, typical radius R30 (the pore aperture radius corresponding to 30% of mercury saturation in a mercury penetration test) is selected to describe the flow capacity of carbonates, and capillary pressure curves are used to establish the saturation height function, by combining Corey-Brooks function and R30.

An OPTIONAL card is:

MAX_CAPILLARY_PRESSURE: 1x10^8 Pa, defining the cut off for maximum capillary pressure.

Relative permeability function

For a multiphase system, the permeability of one phase is reduced for the presence of other phases in the pore space. Relative permeability is the ratio of the permeability of a particular phase within the porous medium to the absolute permeability of the porous medium and is proportional to the phase saturation.

Burdine 's relative permeability function based on Brooks-Corey saturation function is defined for each phase by:

$$k_l^r = (s_{el})^{(3\lambda+2)/\lambda} \tag{23}$$

$$k_g^r = \left(1 - s_{eg}\right)^2 \left[1 - \left(s_{eg}\right)^{(\lambda+2)/\lambda}\right] \tag{24}$$

PERMEABILITY_FUNCTION: BURDINE

LAMBDA 1.0121

LIQUID RESIDUAL SATURATION 0.088

The gas relative permeability values are defined according to Brooks-Corey equation:

PERMEABILITY_FUNCTION BURDINE_BC_GAS

LAMBDA 1.0121

LIQUID_RESIDUAL_SATURATION 0.088

GAS_RESIDUAL_SATURATON 1x10^{-5}

✧ *Section "output"*

KEYWORD→OUTPUT: defines the type and frequency of output.

One of the OPTIONAL card used is:

OBSERVATION_FILE: an observation file gives the values of specified variables (e.g. GAS SATURATION, GAS PRESSURE, ecc.) at a given point at several moments in time.

✧ *Section "time"*

KEYWORD→TIME: specifies the time step and final simulation time

FINAL_TIME: the final time of the simulation

CARD 1: 50 d

CARD 2: 10 d

INITIAL_TIMESTEP_SIZE: 1x10^{-2} days, specifies the initial time step size

MAXIMUM_TIMESTEP_SIZE: 1 day, specifies the maximum time step size

The timestep size is however adjusted by the flow solver according to the mesh resolution and parameters used in the simulation.

✧ *Section "region"*

KEYWORD→REGION: defines a region within the domain.

```
REGION all                    #dimension of the entire domain
 COORDINATES
   0 0 0
   30 10 5
```

```
REGION top                      #top region
  FACE TOP
  COORDINATES
    0 0 5
    30 10 5

REGION bottom                   #bottom region
  FACE BOTTOM
  COORDINATES
    0 0 0
    30 10 0

REGION east                     #east region
  FACE EAST
  COORDINATES
    30 0 0
    30 10 5

REGION west                     #west region
  FACE WEST
  COORDINATES
    0 0 0
    0 10 5

REGION north                    #north region
```

```
 FACE NORTH
 COORDINATES
  0 10 0
  30 10 5

REGION south                  #south region
 FACE SOUTH
 COORDINATES
  0 0 0
  30 0 5
```

- *Section “flow conditions”*

KEYWORD→FLOW CONDITION: sets flow parameters (scalar or vector data sets) used in setting up the flow boundary and initial conditions and source/sinks.

The type of the flow condition is specified in the sub-block TYPE. For each option TYPE, a corresponding type-value card must be included, specifying the value of the TYPE. For this simulation, the Dirichlet boundary conditions have been applied, specifying a fixed value across the entire condition.

```
FLOW_CONDITION 1
 TYPE
  GAS_PRESSURE dirichlet
  LIQUID_SATURATION dirichlet

  GAS_PRESSURE 1.01325e+05                # (Pa)
  LIQUID_SATURATION 9.999900e-01
```

```
FLOW_CONDITION atmosphere
  TYPE
   GAS_PRESSURE dirichlet
   LIQUID_SATURATION dirichlet

  GAS_PRESSURE 1.01325e+05                    # (Pa)
  LIQUID_SATURATION 9.999900e-01

FLOW_CONDITION bottom
  TYPE
   GAS_PRESSURE dirichlet
   LIQUID_SATURATION dirichlet

  GAS_PRESSURE 1.53905+05                     # (Pa)
  LIQUID_SATURATION 9.999900e-01
```

Boundary and initial condition have been applied considering the dimension of the domain involved and the goal of the simulation. The bottom boundary condition has imposed assuming a gradient equal to 10.516 kPa/m. The pressure at the top boundary has been set at the atmospheric conditions. The domain is considered almost fully saturated with water at the beginning of the simulation.

Section “condition couplers”

The condition set in the previous section are here linked to the appropriate region, using different keywords according to the type of condition.

```
INITIAL_CONDITION
  FLOW_CONDITION 1
  REGION all
END

BOUNDARY_CONDITION
  FLOW_CONDITION atmosphere
  REGION top
END

BOUNDARY_CONDITION
  FLOW_CONDITION bottom
  REGION bottom
END
```

✧ *Section “stratigraphy couplers”*

KEYWORD→STRATA: this keyword couples materials ids and/or properties with a region in the problem domain.

```
  MATERIAL soil
  REGION all
```

4.4.2 CO$_2$ injection

The injection of CO$_2$ in the fault domain is described in the PFLOTRAN *CARD 2*. The configurations used for the numerical experiments include an injection well located in the footwall damage zone of the fault and an observation well located moving toward the surface.

This CARD differs from the *CARD 1* only for few keywords applied in the specified section. Only the different keywords are thus described. *CARD 2* simulates the injection of gas CO$_2$ in a well located in the footwall of the fault and uses as initial conditions the results from the simulation with the PFLOTRAN *CARD 1*.

✧ *Section "flow mode"*

KEYWORD→RESTART: defines a checkpoint file from which the current simulation should be restarted. If a time is specified after the file name, the initial simulation is set to that time.

```
RESTART restart.chk 0.0d
```

✧ *Section "region"*

```
REGION well                    #this is the position of the injection well, located in the
COORDINATES                     footwall damage zone of the fault

    8 5 2

    8 5 2


REGION obs1                    #this is the position of the first observation point

COORDINATES

    7.5 5 3.5

    7.5 5 3.5
```

✦ *Section “observation points”*

KEYWORD→OBSERVATION: specifies a location where flow and transport results (e.g. pressure, saturation, flow velocities, ecc.) will be printed in the output.

REGION obs1: The observation point is located at the coordinates defined for REGION obs1.

✦ *Section “flow conditions”*

```
FLOW CONDITION well
    TYPE
        RATE mass_rate
    /
    RATE 0.d0 6.d-4 0.d0                      # kg/s   kg/s   MW  respectively the
                                                liquid, gas and energy values with
                                                the units
```

An injection velocity of $6x10^{-5}$ kg/s was used in a second test of injection.

The injection well (source/sink condition) is the flow condition applied only in the *CARD 2*, restarting using the results of *CARD 1* as initial condition. The well, located in the footwall damage zone, is characterized by the injection rate specified in the “FLOW CONDITION well”. The injection rate is equal to $6x10^{-4}$ kg/s, similar to the injection rates used in the injection test Latera (Pearce, J.M 2004).

✦ *Section “flow conditions”*

```
SOURCE_SINK well
  FLOW_CONDITION well
      REGION well
```

5 Results

The structural analyses conducted in the Roman Valley Quarry evidenced how the distribution of the tar is controlled by the activity of the two oblique normal faults cutting the Bolognano Formation. The hydrocarbons migrated toward the surfaces along main migration pathways, like slip surfaces and extensional jogs. They also migrated laterally filling the high porous carbonate rocks flanking the faults. Most of the hydrocarbon flow postdated fracturing and faulting (Agosta et al., 2009).

5.1 Northern and southern sectors of the fault

It is clear from field investigations the different hydraulic behavior of the southern and northern sectors of the fault. The southern sector is characterized by a core, filled with tar both in the matrix and in the fractures, behaving as a conduit to the flow. The northern part is characterized by cores with discontinuous bodies filled with tar, behaving mostly like seals to the flow. The number of fractures filled with tar is around 52% in the southern sector and around 35% in the northern one. In the southern sector, most of the fractures filled with tar are parallel to the NE fault zone. In the northern sector, also fractures perpendicular to the fault plane result filled with tar, probably because the proximity to the SW fault zone is interfering with the stress field.

The DFN modeling performed with Move® shows that permeability and porosity vary along the quarry. In the fault zone, the permeability shows higher values in the hanging wall of the fault, because of the gravitative effects due to the dip direction of the fault plane. Comparing the two sectors of the fault, the highest values of permeability are found in the southern sector of the fault, in agreement with field observations, with a maximum medium value of 1154 mD (order of 10^{-12} m^2); the porosity show a maximum value of 1.34%. Furthermore, in the southern sector the higher values of permeability are found closer to the core, in agreement with the different distribution of fractures along the fault.

5.2 Numerical experiments of flow in the fault zone

The first results of the numerical experiments of fluid flow in a hybrid medium (see Paragraph 3.2) are presented to show how the proposed workflow can be applied to model fluid flow in a fault zone. To allow the first simulations to run in a reasonable time, the original domain of the fault (Figure 22) was reduced in the y and z dimension and the mesh coarsened (Paragraph 4.4). Two simulations were performed with the same boundary and initial conditions, but using two different injection rates, to see how the diffusion of the CO_2 in the fault domain is affected by this parameter.

5.2.1 Steady state (initial condition)

The first simulation was performed to reach a steady state condition of pressure in the fault domain (Figure 30; paragraph 4.4.1 Steady state simulation- CARD 1). The steady state was used as the initial condition for the simulations of the injection of CO_2.

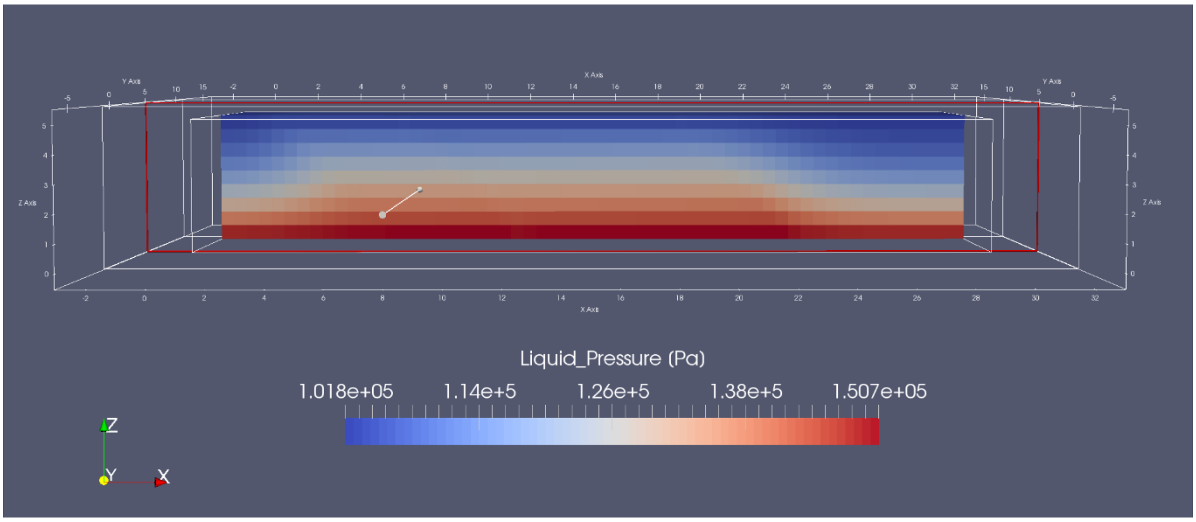

Figure 30. Initial steady-state condition applied for both the high and low velocity injection as result of the simulation with the PFLOTRAN CARD 1 (see paragraph 4.4.1 for detailed explanation). The hydrostatic condition shows the distribution of the pressures linearly increasing with depth. Only liquid pressure is shown, since the domain is initially full saturated in water. The scale of the horizontal and vertical axes is in meters.

5.2.2 Injection of CO_2

Results from the numerical experiment with the injection of CO_2 are presented (paragraph 4.4.2 CO2 injection - CARD 2 for details). The following figures show the results at different time steps of the injection of CO_2 in the footwall of the fault, for a slice of the domain created along the y direction, at the point of injection, located at the coordinates (x, y, z): (8, 5, 2). The figures show the results for two different injection mass rates used in the simulation at the most significant time steps, for the two most important variables: gas pressure and gas saturation. The higher injection rate refers is equal to 6×10^{-4} kg/s while the lower injection rate is 6×10^{-5} kg/s.

5.2.2.1 Gas pressure

Gas pressure variations are shown in the very first moments after the injection, to show the saturation changes around the injection well and then with a coarser time step, with the spreading of the CO_2 plume until the end of the simulation. Time steps are expressed in days.

<u>High injection rate (6×10^{-4} kg/s)</u>

a) Time step: 0.001 days

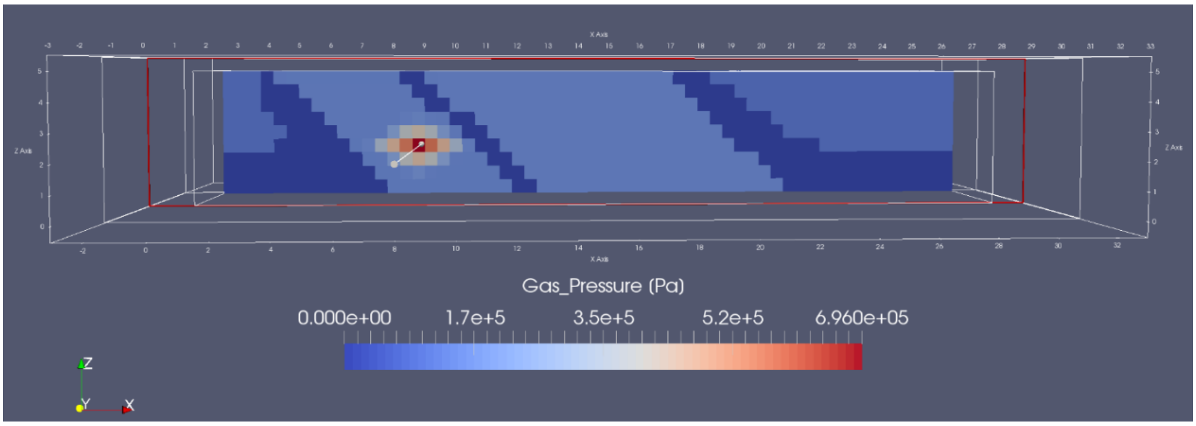

b) Time step: 0.009 days

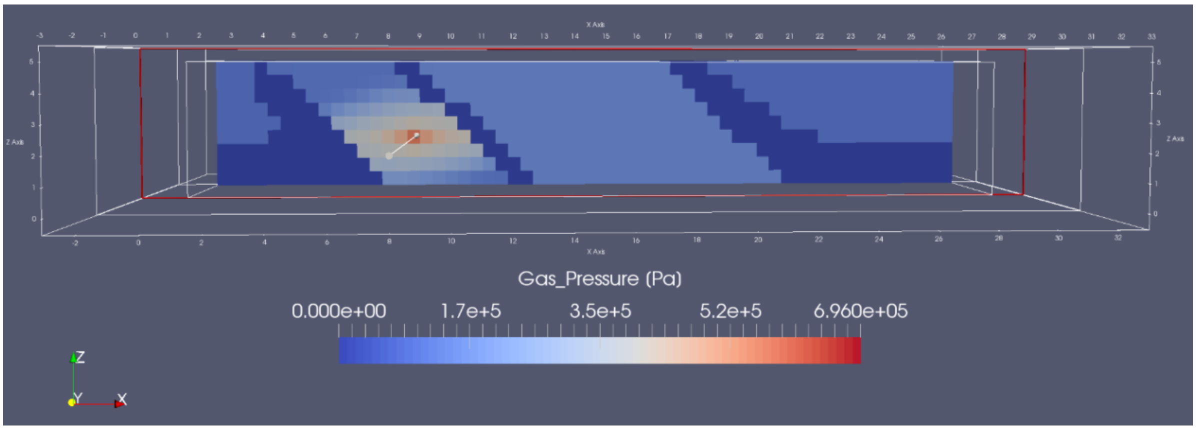

c) Time step: 1 day

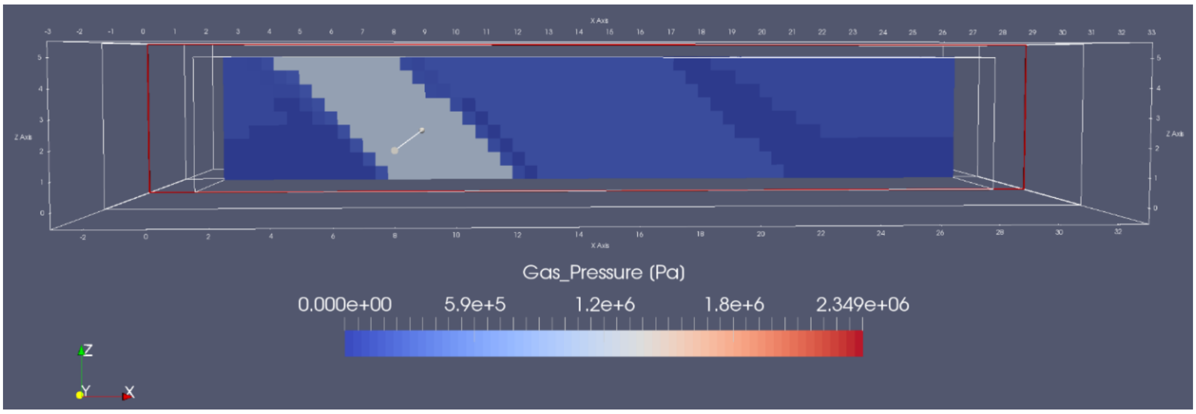

d) Time step: 5 days

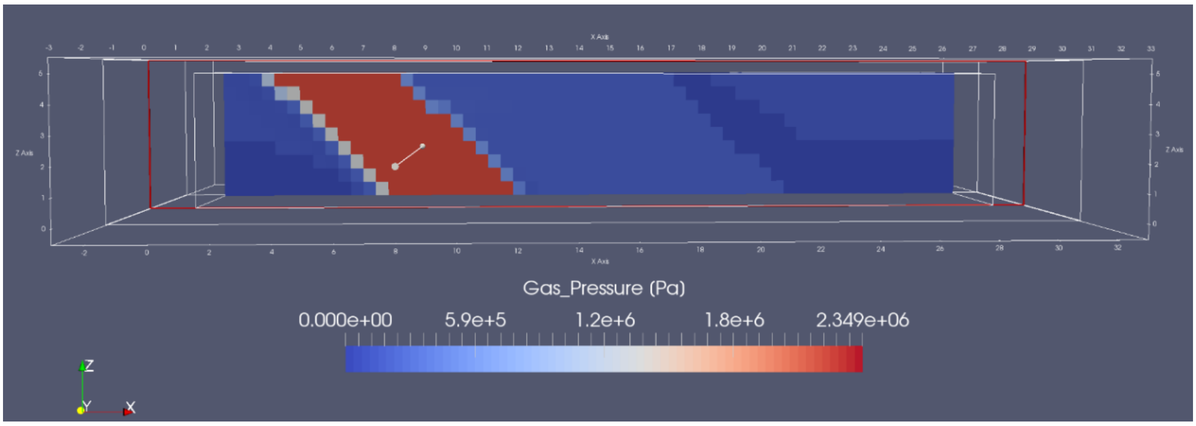

e) Time step: 10 days

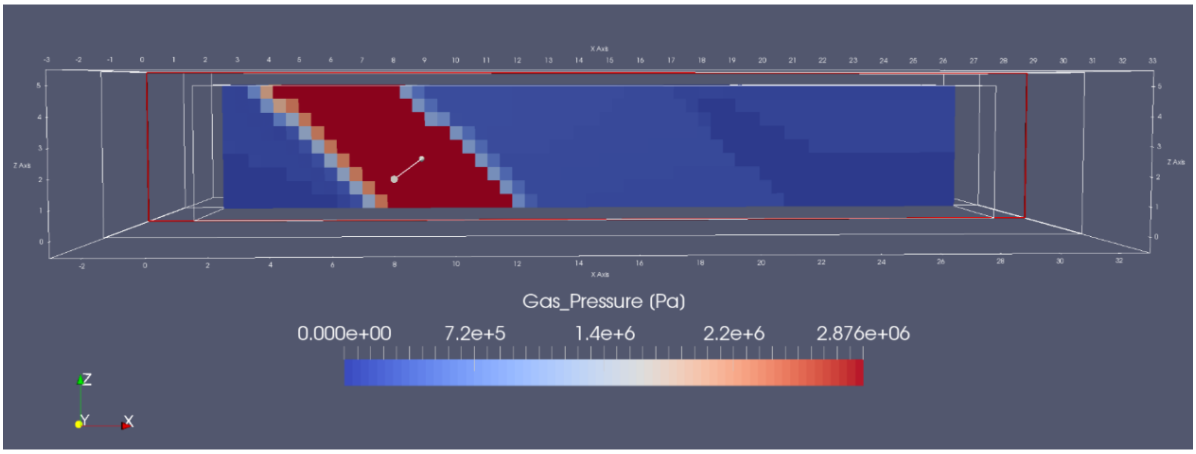

Figure 31. Gas pressure variations in the fault domain after the injection of gas CO_2 *into a well located at the coordinates (x, y, z): (8, 5, 2). The increase in gas pressure is shown at different time steps and appears controlled by the permeability structure of the domain. Figures a-b show the very first moments after the injection: the gas appears to be concentrated around the injection point, where it reaches the maximum value of the pressure. Figures c-d-e show respectively the variations at 1, 5 days and at 10 days (end of the simulation): the gas progressively invades the fault footwall domain, since its dimension is pretty small. Figure e shows how the gas pressure is relatively smaller along the boundary with the core (permeability in the order of* 10^{-20} m^2*), compared to the rest of the fault footwall. These values are explained in Chapter 6. The scale of the axes is in meters.*

<u>*Low injection rate (*6×10^{-5} *kg/s)*</u>

a) Time step: 0.001 days

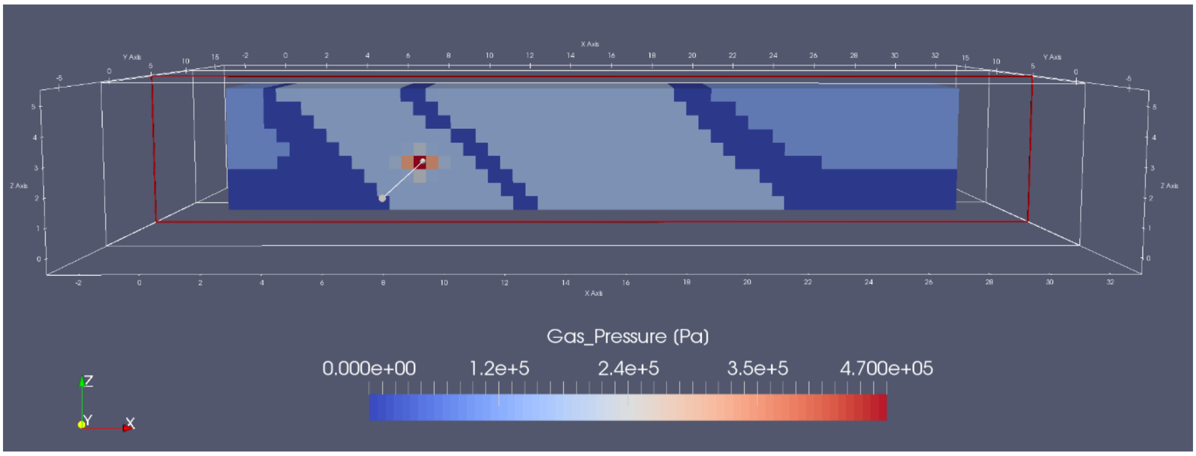

b) Time step: 0.009 days

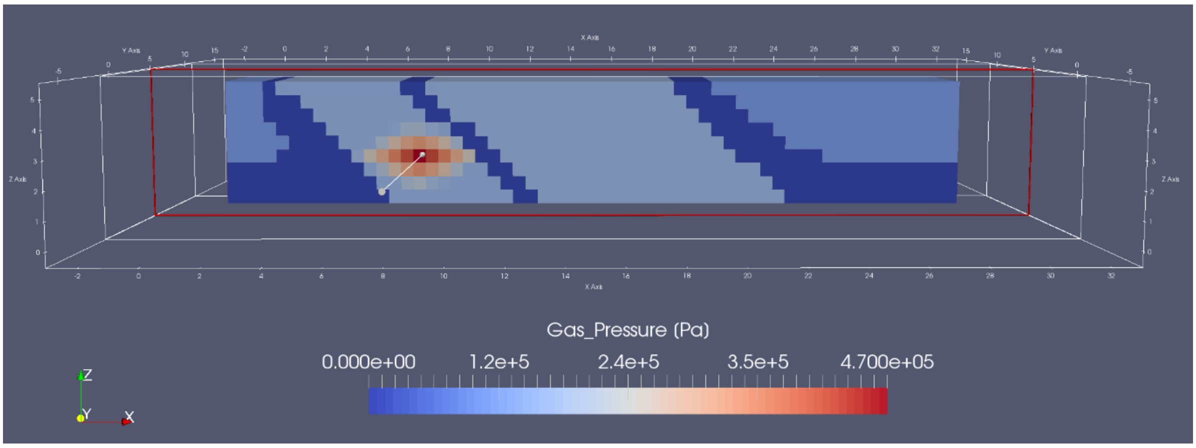

c) Time step: 1 day

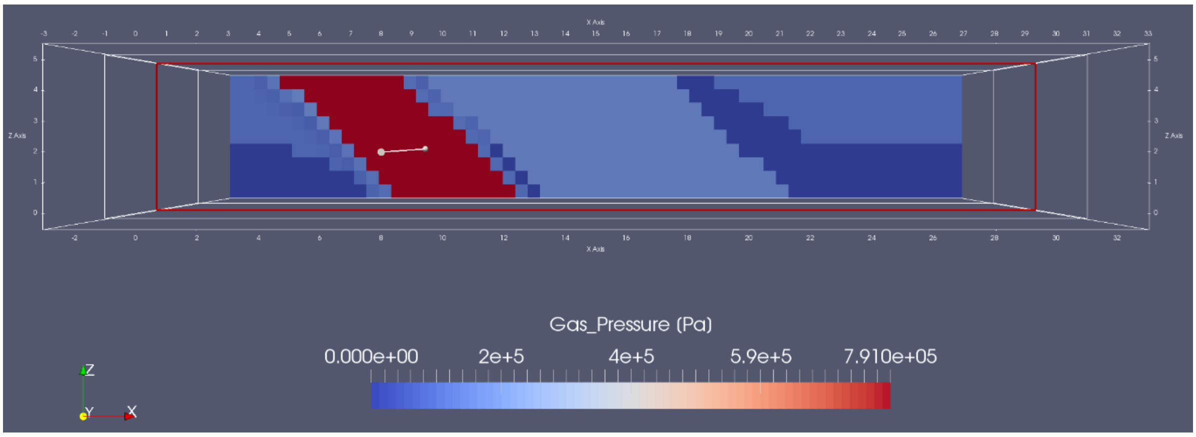

d) Time step: 5 days\

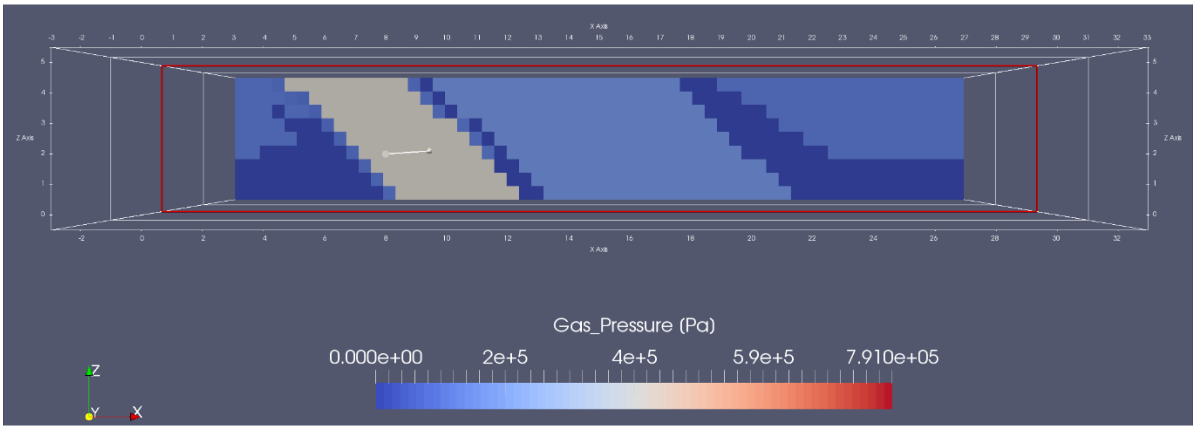

e) Time step: 10 days

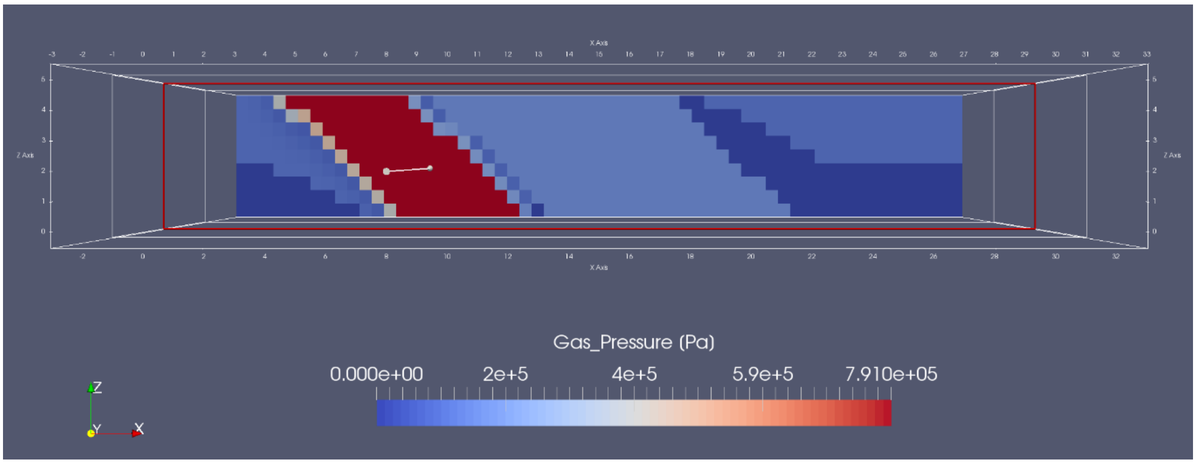

Figure 32. Gas pressure variations in the fault domain after the injection of gas CO_2 *into a well located at the coordinates (x, y, z): (8, 5, 2). The increase in gas pressure is shown at different time steps and appears controlled by the permeability structure of the fault zone. Figure a-b show the very first moments after the injection: the gas appears to be concentrated around the injection point, where it reaches the maximum value of the pressure. Figure c-d-e show respectively the variations at 1, 5 days and 10 days (end of the simulation): the gas progressively invades the fault footwall domain, since its dimension is pretty small. Figure e shows how the gas pressure is relatively smaller along the boundary with the core (permeability in the order of* 10^{-20} m^2*), compared to the rest of the fault footwall. These values are explained in Chapter 6. The scale of the axes is in meters.*

5.2.2.2 Gas saturation

Gas saturation variations are shown in the very first moments after the injection, to show the saturation changes around the injection well and then with a coarser time step, until the end of the simulation. Time steps are expressed in days.

High injection rate (6×10^{-4} kg/s)

a) Time step: 0.001 days

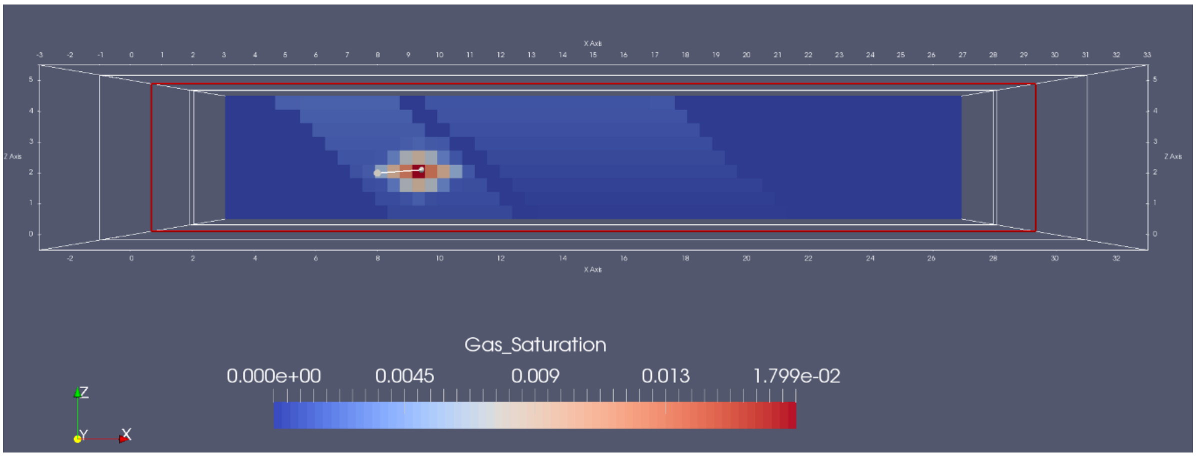

b) Time step: 0.009 days

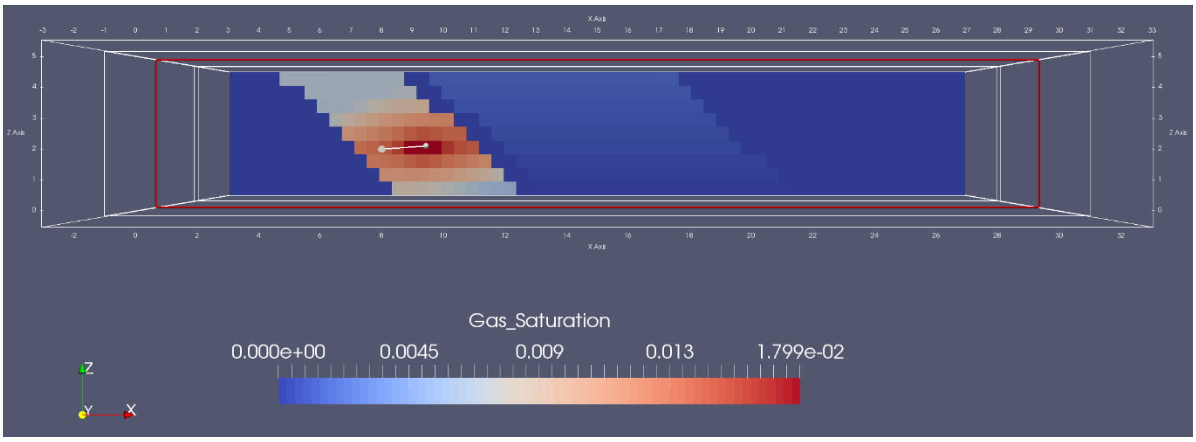

c) Time step: 1 day

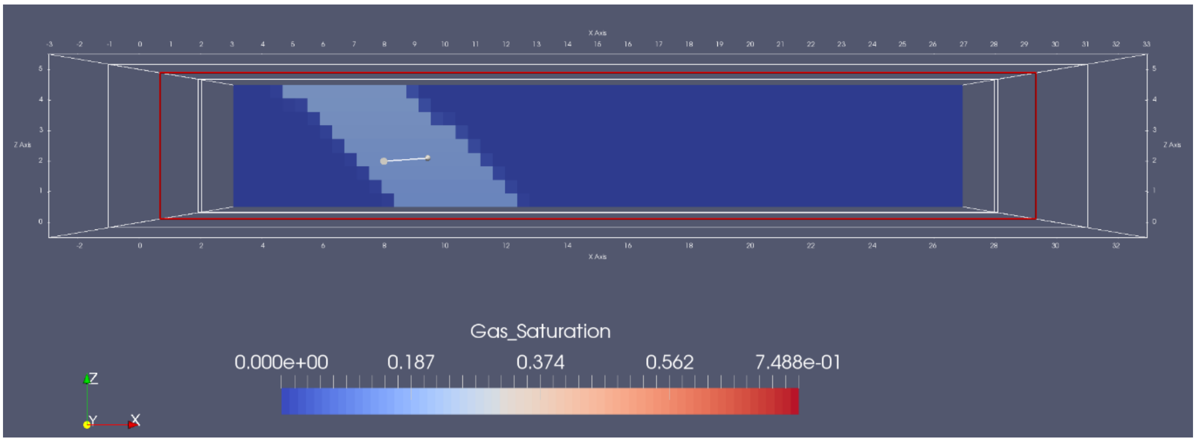

d) Time step: 5 days

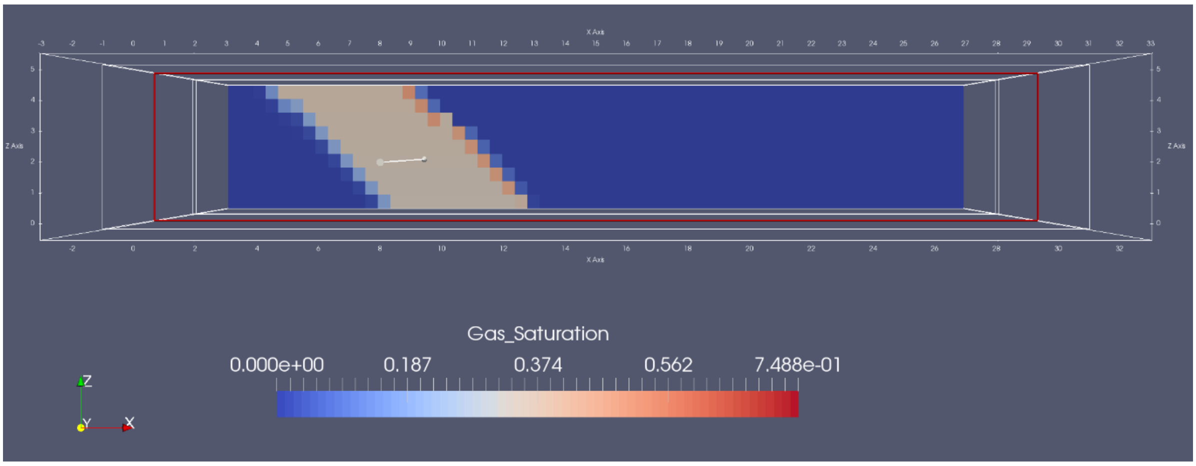

e) Time step: 10 days

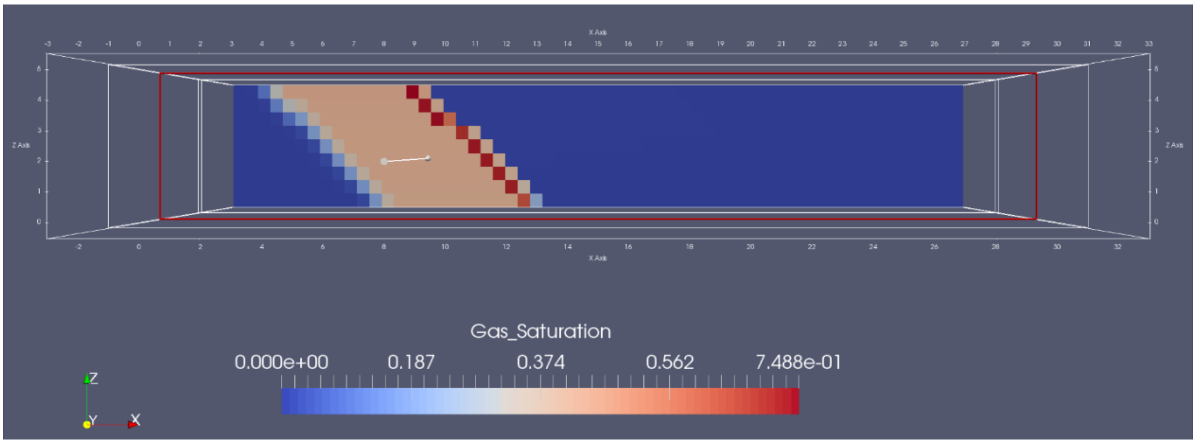

Figure 33. Gas saturation variation in the fault domain after the injection of gas CO2 into a well located at the coordinates (x, y, z): (8, 5, 2). The increase in gas saturation is shown for different time steps. Figure a-b show the very first moments after the injection: the gas appears to be concentrated around the injection point, where it reaches the maximum value of the saturation. Figure c-d show the variations until the at 1, 5 and days respectively: the gas progressively invade the fault footwall domain, since its dimension are pretty small. Figure e shows the distribution of the saturation at the end of the simulation, where the gas appears concentrated mostly close to the core of the fault, characterized by a low permeability (in the order of 10^{-20} *m*^{2}*). The scale of the axes is in meters.*

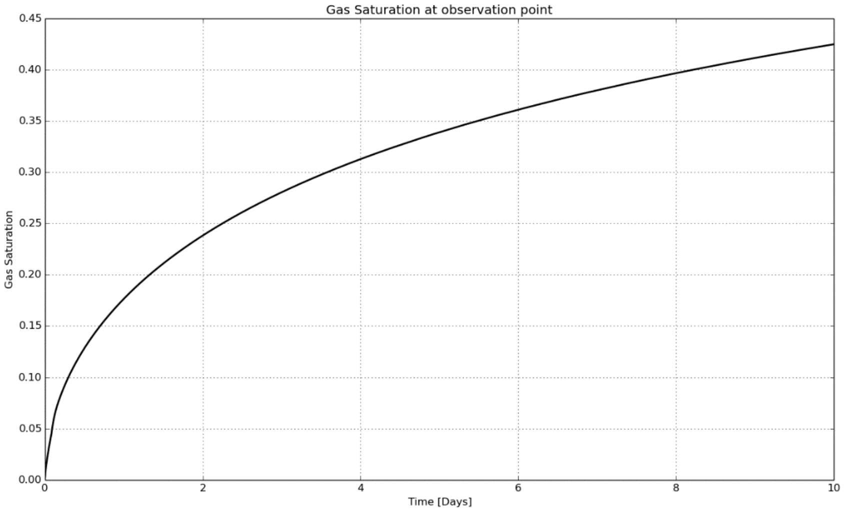

Figure 34. Gas saturation variation detected at an observation point located in the fault footwall at the coordinates (x, y, z) : (7.5, 5, 3.5). The gas saturation progressively increases as long as the injection happens.

<u>Low injection rate (6×10^{-5} kg/s)</u>

a) Time step: 0.001 days

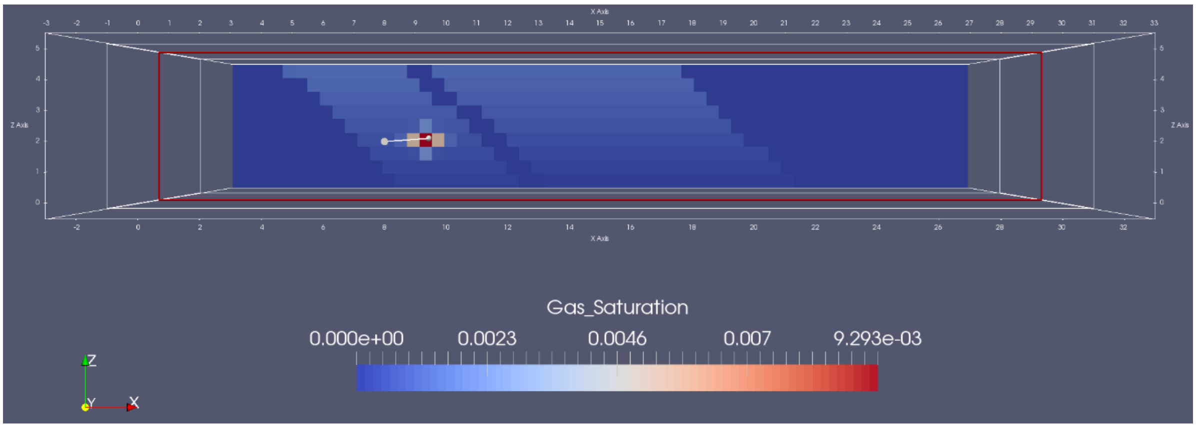

b) Time step: 0.009 days

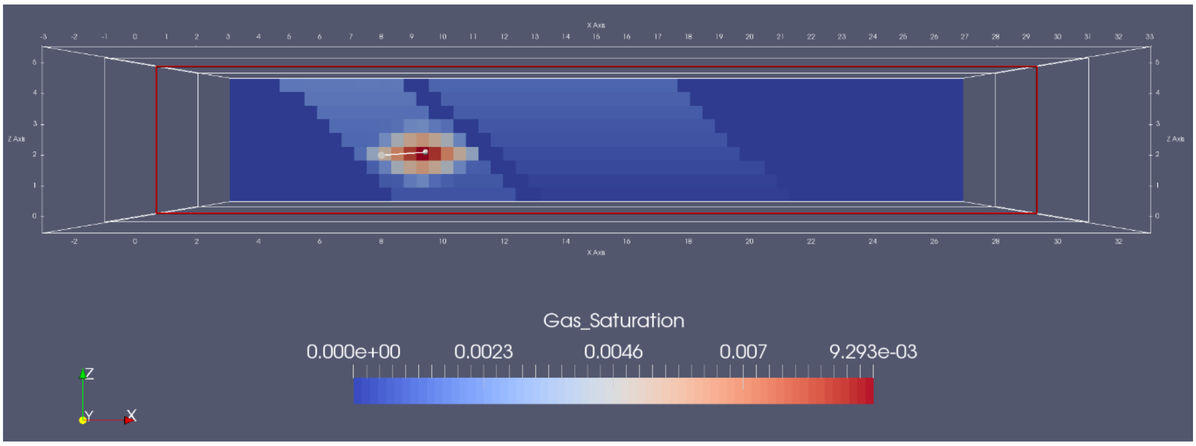

c) Time step: 1 day

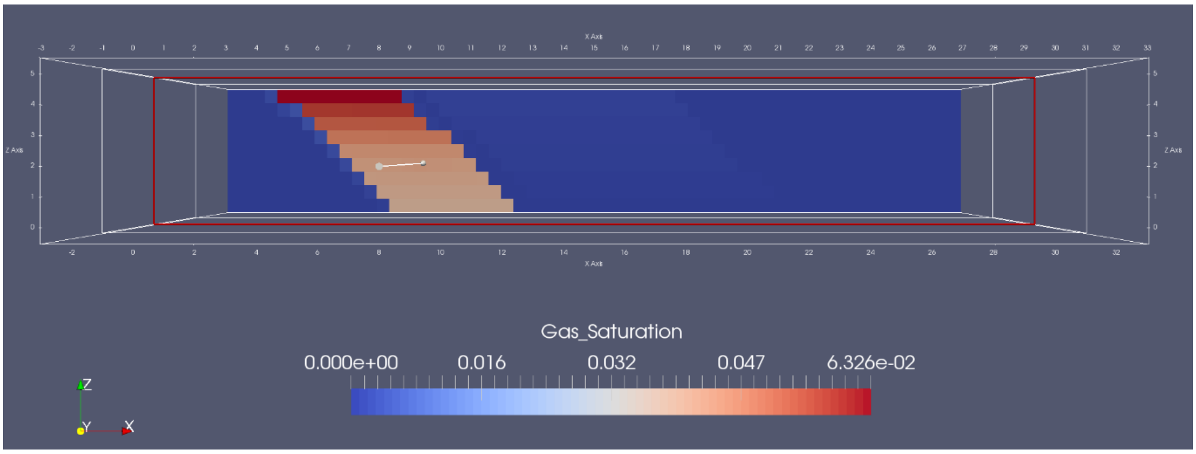

d) Time step: 5 days

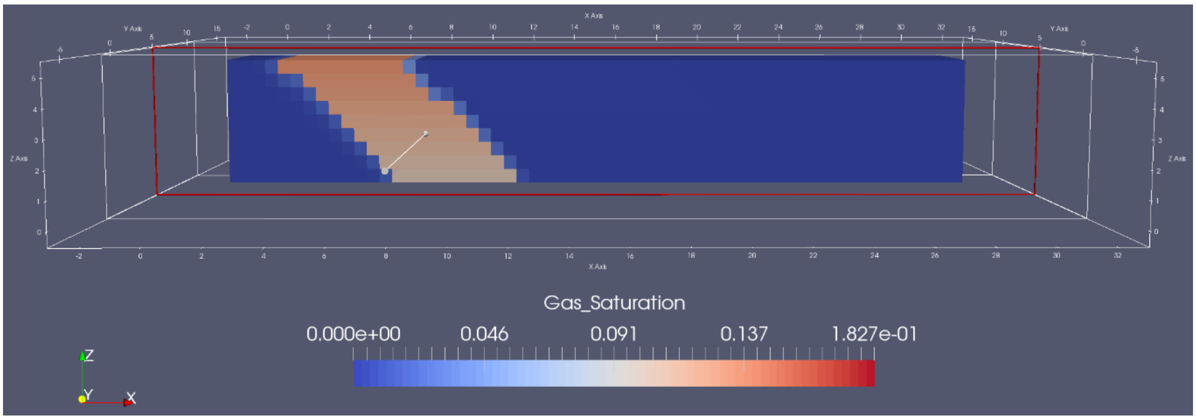

e) Time step:10 days

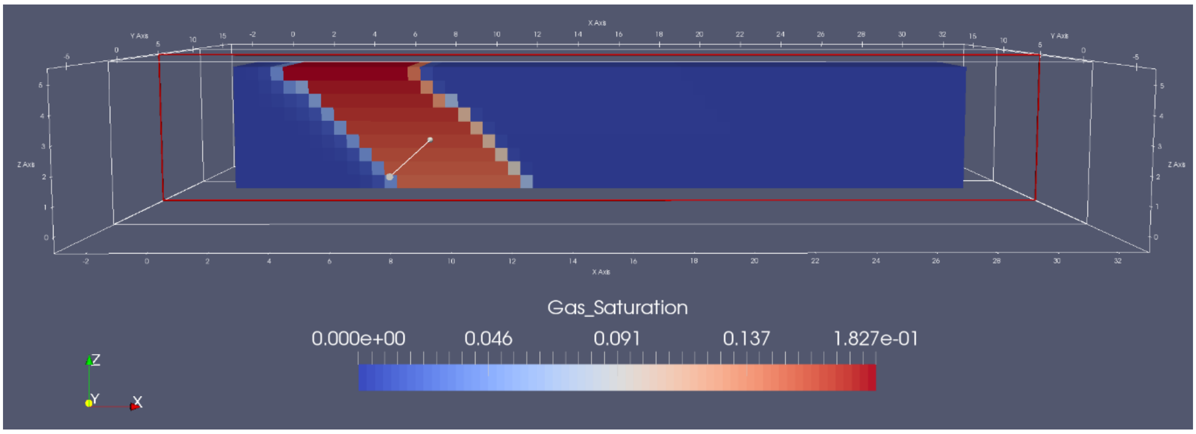

Figure 35. Gas saturation variation in the fault domain after the injection of gas CO_2 into a well located at the coordinates (x, y, z): (8, 5, 2). The increase in gas saturation is shown for different time steps. Figure a-b show the very first moments after the injection: the gas appears to be concentrated around the injection point, where it reaches the maximum value of the saturation. Figure c-d show the variations until the at 1, 5 and days respectively: the gas progressively invade the top of the fault footwall domain and then invades progressively the whole domain, since its dimension are pretty small. The scale of the axes is in meters.

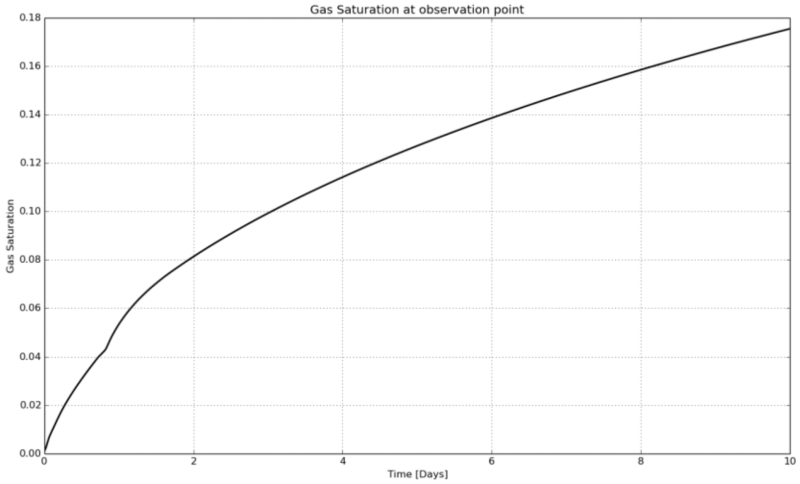

Figure 36. Gas saturation variation detected at an observation point located in the fault footwall at the coordinates x, y, z: 7.5, 5, 3.5. The gas saturation progressively increases as long as the injection happens.

6. Discussion

The hydraulic differences found along the fault zone are related mainly to the architecture of the fault: the distribution of the lithologies along with the stress field brought a variation in the deformation style from one side to the other in the fault and hence to the mechanisms of hydrocarbon migration.

The variation in the throw within the fault from one side to the other was not considered explicitly in the numerical experiments, but probably some of the differences observed between the two sides of the fault could be addressed by a variation of this parameter. The cores are the main flow conduits in the southern portion of the fault, characterized by coarser granulometries and the migration of tar in both fractures and matrix of the Bolognano Formation. In the northern sector, the cores act as a flow barrier because of the smaller granulometries, forcing the tar to mainly flow along the fracture systems.

Previous field works in the Roman Valley Quarry (Agosta et al., 2010) found power law spacing and length distribution of the fractures parameters, a result confirmed by the analysis of field data in the present study. Agosta et al. (2010) evidenced that tar-rich fractures may have up to 1.2% of 2D porosity, with a mean value of 0.45%, in accordance to the pronounced secondary porosity of the carbonate matrices present in the fault damage zone (Nelson, 2001). These values agree with those found in the present study. The DFN modeling shows values higher than 0.45%, closer to the upper range reported in Agosta et al. (2010). On the other hand, the DFN generated with *dfnWorks* show a value of the porosity close to the medium value found by the same authors. According to Agosta et al. (2009) most of the hydrocarbon flow postdated the fracturing and faulting of the carbonates, again in agreement with the field investigations reported in the present study.

Panza et al., (2017) estimated the equivalent permeability of the fracture systems outcropping in the quarry, in terms of background deformation and evolution of the fault zones (incipient, small and medium faults). For the medium faults in the model, they found medium values for the K_{xx} and K_{yy} direction respectively equal to ~$1.15*10^4$ mD and ~$4.5*10^3$ mD (10^{-11} to 10^{-12} m^2). They considered structural elements of different nature: pressure solution seams, joints and calcite veins, presenting the data relative only to the x and y directions of the permeability tensor, because of they did not include in the calculation all the bed-parallel primary and secondary elements (pressure solution seams and compaction bands).

The data acquired in the field work for the present study are relative only to the fractures (joints) created by the NE fault activity. We did not consider any background deformation. The conceptual model of the fault outcrop (Figure 25, paragraph 4.3 Upscaling the small-scale properties) was inspired by the description of the mature stage of the main fault zones in Agosta et al. (2009). The choice to limit the dataset to open fractures only was made to reduce the complexity of the numerical model by including only those elements effectively contributing to the fluid migration. High permeability fractures in and around a storage formation can provide pathways to transport CO_2 towards the surface (Pruess, 2008; Annunziatellis et al., 2008) and as such are generally seen in a negative light when assessing storage security. For the DFN generated with Move®, the order of magnitude of the medium values for the K_{xx} an K_{yy} are respectively in the order of 10^{-13} m^2 for both the northern and southern zones.

The dataset used to study the differences between the two sides of the fault zone is related primarily to the spacing of the fractures, used to distinguish volumes along the fault profile characterized by the same frequency of the fractures. In this way the anisotropy in the permeability tensor has not been detected, because of the different data analysis approach, based on the zonation of the fractures of the fault damage zones according to their spacing along the fault profile, instead of to their characteristic orientations. The permeability values calculated by *dfnWorks* are in the order of 10^{-10} m^2 in the K_{xx} and K_{yy} directions and 10^{-11} m^2 for the K_{zz} direction. The smaller value in the K_{zz} direction is in agreement with the stress field in the region, where the minimum permeability is parallel to the orientation of the maximum stress component ($\sigma 1$). The differences with Panza et al. (2017) can be explained by the different approach employed in the calculation of the permeability. Move® uses the analytical methodology from Oda (1985), where the equivalent permeability is calculated directly from the geometry and the properties of the fractures contained in a cell. The approach used with *dfnWorks* is a numerical upscaling, that not always match with the results of the analytical method. The lack in differences between the components of the permeability tensor in the x and y direction is because of my choice to assign a higher probability of occurrence in the generation of the DFN to the size of the data sets, instead of their density values (see Table 4). This may have influenced the values of the calculated upscaled permeability.

The fluid flow simulation in the bulk fault zone, was performed primarily to test to the methodology, coupling the core of the fault, with the upscaling of the properties of the DFN simulation to an equivalent continuum. The computational resource available at that moment strongly influenced the simulation, impacting on the time necessary to perform the numerical calculations.

The first numerical results show how the distribution of the permeability controls the migration of the CO_2. The high permeability in the footwall damage zone allows for the fast diffusion of the gas in this portion of the fault.

Also, the injection rate plays a role in the spreading of the CO_2 plume. The CO_2 injected with a higher mass rate accumulates mostly toward the fault core, where it reaches its maximum values of saturation (see Figure 33e). The injection at a lower mass rate shows instead a wider diffusion in the fault footwall domain, in terms of saturation, without any significant accumulation at the core-footwall damage zone boundary (see Figure 35e). To ensure the numerical consistency of the results, a comparison was made between the liquid and gas pressure at the boundary fault damage zone-core, to exclude the presence of a numerical instability in the model.

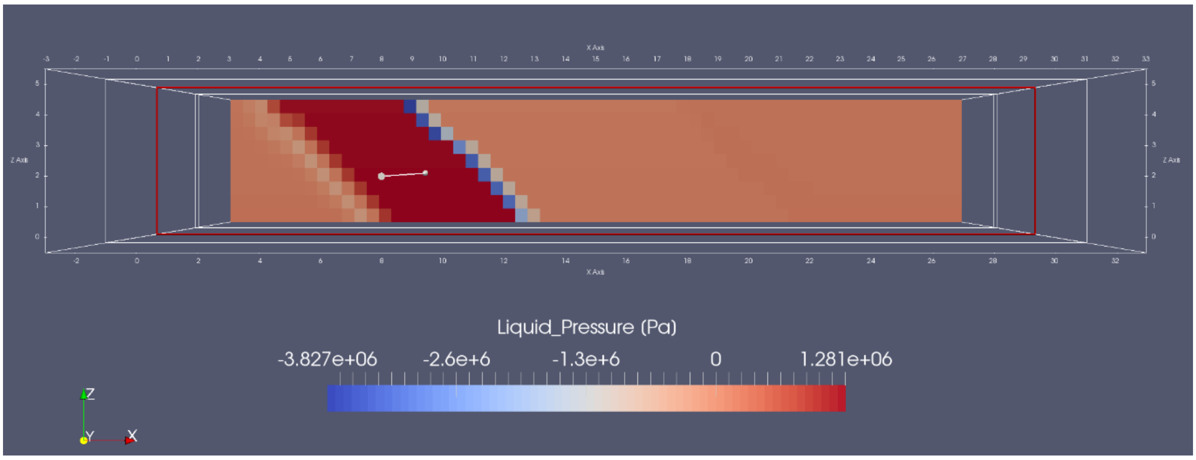

Figure 37. Liquid pressure distribution in the fault footwall domain for the high injection mass rate simulation. Negative values are found in the grid cells close to the fault footwall damage zone-core boundary. These values are numerically consistent with the value of the capillary pressure in the same grid cells (see text for explanation). The scale of the axes is in meters.

The existence of negative liquid pressure values in cells at the core/damage zone boundary is a proof of the stability of the numerical method implemented since they can be explained by the effect of capillary pressure and gas saturation (see Figure 33). For a grid cell at the fault footwall damage zone-core boundary, the liquid pressure can be calculated according to:

$$p_c = p_g - p_l \tag{25}$$

where p_c, p_g, p_l are respectively the capillary pressure, the gas phase pressure and the liquid phase pressure. Figure 38 shows a plot of the experimental capillary pressure against the analytical curve calculated according to (22), the equation governing the relation between capillary pressure and saturation of the liquid phase. The agreement between the analytical values from (22) and the numerical values of the liquid pressure from (25) verify the numerical consistency of the results.

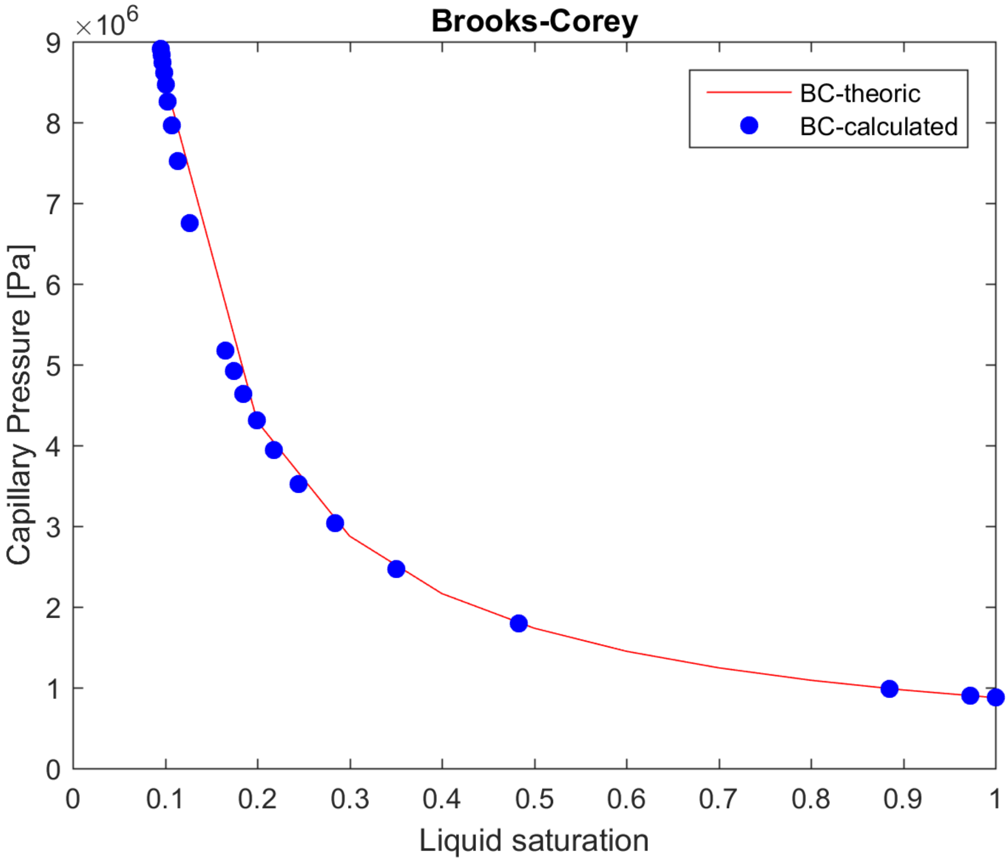

Figure 38. Comparison between the theoretical and the calculated values of the capillary pressure in the numerical simulation of injection of CO2 in the fault footwall. The experimental data fit with the analytical solution, ensuring the consistency of the simulation

7. Conclusions

A quantitative assessment of how fractures and faults control fluid flow is critical in several areas of geological and environmental sciences: petroleum, gas, geothermal and water supply reservoirs as well as potential sites for CO_2 and CH_4 sequestration, or nuclear wastes disposal can be hosted in fractured rocks. My work integrated geological fieldwork, quantitative analysis of the faults/fractures distribution and numerical modeling to investigate fluid flow in a fault zone, in a multidisciplinary approach to the problem.

The specific target of my studies was the fault zone of the Bolognano Formation exposed in the Roman Valley Quarry, in the town of Lettomanoppello (PE), Majella Mountain. We selected the Roman Valley Quarry as study site because of the exposure of the inner structure of two oblique slip normal faults. Furthermore, the massive presence of fluid migration in the form of tar in the fracture systems makes this site a good natural analogue for studies of fluid flow in fractured media.

The numerical modeling was performed using both commercial (MOVE) and open source software (*dfnWorks,* PFLOTRAN). MOVE was used to develop a first model to explore the hydraulic differences observed in the field between the northern and southern sectors of the fault zone. The model was based on the division of the fault zone in volumes characterized by similar spacing values in the fracture systems. In the fault zone, the permeability shows higher values in the hanging wall of the fault, because of the gravitative effects of the immersion of the fault plane.

Comparing the two sectors of the fault, the highest values of permeability are found in the southern sector of the fault, in agreement with field observations, with a maximum value of 1479,43 mD (order of 10^{-12} m^2). The southern sector can thus be assimilated to a flow conduit, while the northern sector acts more as a seal.

dfnWorks was used to infer the hydraulic parameters of the fracture systems of the damage zones of the fault. These parameters were then used to upscale the properties of the fractures to an equivalent continuum medium, to simulate the fluid flow in the bulk fault zone, coupling the core and the damage zones.

The numerical model of CO_2 flow in the fault zone was developed using the open source software PFLOTRAN. To better reproduce a real-life case study, I simulated the injection of CO_2 into the footwall of the Roman Valley Quarry fault. Hydrostatic initial conditions were imposed. I then simulated the injection of CO_2 through a well in the fault foot wall. The numerical experiments show that the main factor controlling the migration of the CO_2 in the along the fault is the distribution of the permeability. The high permeability in the footwall damage zone allows the fast diffusion of the gas in this portion of the fault. For high injection mass rate, the CO_2 accumulates mostly toward the fault core, reaching its maximum values of saturation at the end of the simulation.

Modeling multiphase flow in three dimensional similar scenarios is a complex problem, involving many different processes at different scales. The numerical experiments presented here show the potential of the software and the proposed workflow. The numerical complexity of the problem (for example, a mesh of about 10^6 cells may be necessary to correctly reproduce the geometry of the fault zones) requires appropriate computational resources and numerous numerical experiments to calibrate the appropriate boundary conditions necessary to reproduce a real test site of CO_2 injection.

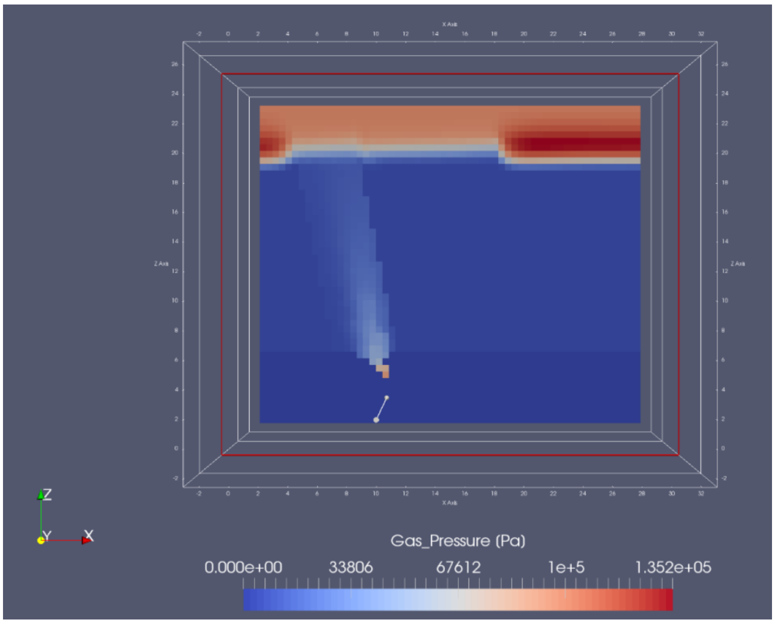

Figure 39. CO_2 injection in the fault footwall domain into a well located at (x,y,z): (10,8,2). The dimension of the domain respects the real dimension of the fault zone object of this study, whose properties are described in Chapter 4.3. The initial condition is hydrostatic and takes into account a saturation and initial pressure also for the gas phase (compared with the simulation described in Chapter 4.4). After few hours from the injection into a well, the plume of CO_2 rising to the top of the domain is visible. The scale of the axes is in meters.

8. Formation and evolution of the near axis 8˚20’N seamount chain

The present discussion will focus on the geophysical data analysis and interpretation, to understand whether the volcanoes that comprise the seamount chain are coeval or if the chain is age progressive. This has strong implications on the mechanism of migration of melts feeding off-axis magmatism.

8.1 Data collection

The geophysics data were collected on board the R/V Atlantis, for the AT37-05 OASIS expedition (Nov-Dec 2016). The survey comprised the acquisition of multibeam, gravity and magnetic data at the 8˚20’N seamount chain on the west flank of the EPR, north of the Siqueiros Fracture Zone. Surveys were conducted at an average speed of ~10 knots with a sampling rate of ~1 Hz. The combined track lines of both surveys collected over 1900 line-km of data.

8.1.1 Multibeam data collection

Bathymetric data were collected using a mounted Kongsberg EM122 multibeam system, using a swath angle of 65° in water ranging in depth from 4,251– 2,029 meters with corresponding swath widths of 2,560 – 5,364 m. The survey consisted of eight E-W long survey lines and five N-S lines, three of which transect the E-W survey (Figure 2). At the start of each long survey line, an 1800 m XBT was launched to record sound velocity, conductivity, and temperature. XBTs do not measure salinity and as such salinity measurements at depth are assumed to be comparable to those measured at the surface. The geophysics survey mapped over 30 edifices in the chain with complex relationship to both local and regional structures. These include E-W to NNE-SSW trending ridges in the eastern half of the chain upon which the larger edifices are built and that generally parallel the Siqueiros FZ, and ~N-S trending constructs that conform to EPR abyssal hill trends (~350°) on the Pacific Plate in this region.

In addition, there are numerous small ~1-2 km flat-topped conical constructs, often with summit craters, occurring as satellite features around the larger seamounts and in some cases aligned along abyssal hill trends. The geophysics survey provided also a context for the location of the seamounts with respect to the Siqueiros fracture zone to the South. Two tie lines connecting the surveys provided additional data compare the northern, younger plate with the older plate to the South. All the bathymetric data were processed at sea using QPS Qimera software, which allows for the visualization, processing, and manipulation of raw sonar data. The map was gridded at 75 m in the WGS-84-UTM-13N coordinate system.

8.1.2 Gravity (tie information, processing of data at sea)

Gravimetric data were collected using a BGM-3 sea gravimeter installed on the R/V Atlantis to acquire continuous gravity data. The processing of the data started at sea: the raw gravity data were filtered with a low-pass Buttherworth filter and corrected for both Eötvös and drift correction. Land gravity ties were carried out at each port stop of the R/V Atlantis over the 3 months before the expedition and were used to calculate the drift of the BGM-3 sensor to correct the data. Finally, the Free-Air Anomaly (FAA) was calculated by subtracting the corrected raw data with the IGF80 reference gravity field. At the end of each geophysical survey, the comparison of all the FAA data with the bathymetric maps acquired by the multibeam system ensured the consistency of the gravity data.

8.1.3 Magnetic

Magnetic data collection was conducted using a Marine Magnetics SeaSPY Overhauser Magnetometer System. The SeaSPY is a total field magnetometer that measures the magnitude of the magnetic field vector independent of its direction. Surveys were conducted with the magnetometer towed approximately 280 m behind the ship.

The processing of the magnetic data started at sea. Due to a "spark" effect thought to be caused by a cable issue, raw data were filtered using a 1000th median filter. The filter successfully smoothed the "sparking" points without changing the normal data. The processing was performed using the NSF-supported Rolling Deck to Repository (R2R) Program. The R2R code utilizes navigation information to generate the magnetic scalar potential at the time of the data collection and removed the corresponding IGRF model before outputting magnetic anomaly data.

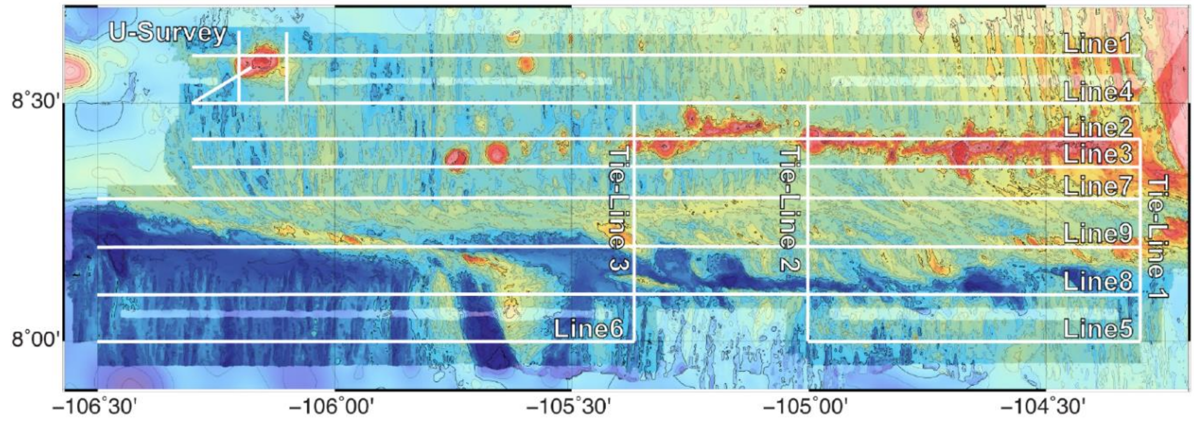

Figure 40. A ship-based geophysical survey was conducted to map the entire region. EM-122 multibeam, BGM-3 gravity, and SeaSPY Overhauser Magnetics were collected along white lines as indicated.

8.2 Methods

8.2.1 Thermal model calculations

A three-dimensional (3D) passive mantle upwelling model was developed following the methods of Gregg et al. (2009) using the commercial finite element software COMSOL Multiphysics® 5.2, to evaluate the thermal structure in the region. The geometry of the ridge-transform fault, was defined within a computational domain 600km long, 200km wide and 100km deep.

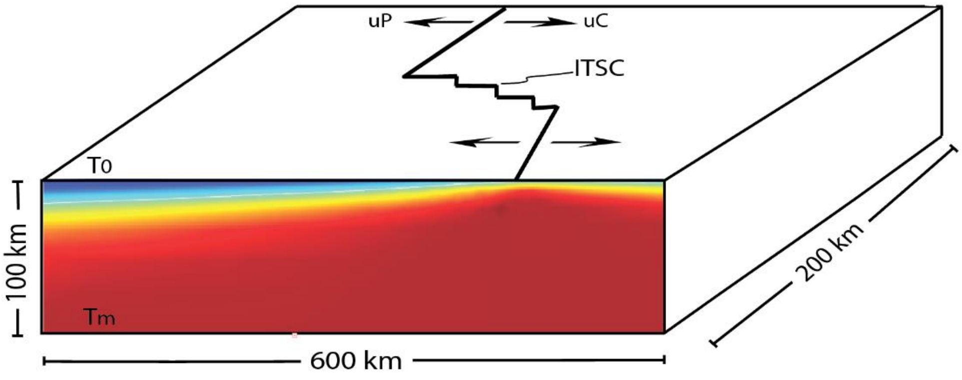

Figure 41. Three-dimensional passive flow model used to simulate the thermal structure in the study area. Spreading velocities are imposed at the surface. The temperature at the surface, T_0 and at the base, T_m are used as boundary condition at the top and the base of the model box. The bottom and side boundaries are imposed stress free, allowing the convective flux from the mantle below.

The region of interest is focused in the region from 9.2 to 7.4 N, around the Siqueiros Transform Fault, which has been reconstructed including the four ITSCs within the transform domain. Mantle flow is driven by the divergence of two plates, at the top of the domain, with an half spreading rate of 55 mm/yr. Temperature on top is assumed to be 0˚C and a mantle temperature of 1350 ˚C is imposed on the bottom. The bottom and the side boundaries are imposed as stress free, allowing for convective flux from the mantle below. We defined a tetrahedral mesh, which is finer in the first 30 km of depth and around plate boundaries. The flow field and temperature are solved using the “Laminar Flow” and “Heat Transfer in Fluids” Comsol Multiphysics® applications. The model is assumed to be in steady state and is solved using the default solver provided by the software.

Conservation of mass, momentum and energy are given by:

$$\nabla \cdot \mathbf{V} = 0 \tag{26}$$

$$\nabla P = \nabla \cdot [\eta(\nabla \boldsymbol{V} + (\nabla \boldsymbol{V})^T)] \tag{27}$$

$$\rho C_p(\boldsymbol{V} \cdot \nabla)T = \nabla \cdot (k \nabla T) \tag{28}$$

respectively, ρ is the density of the mantle, P is pressure, $\mathbf{V}$ is the velocity field, η is the effective mantle viscosity, C_p is the heat capacity, T is temperature, and k is the thermal conductivity.

We adopt a temperature dependent viscosity, calculated by:

$$\eta_T = \eta_0 exp\left[\frac{Q}{R}\left(\frac{1}{T} - \frac{1}{T_m}\right)\right] \tag{29}$$

where η_0 is the reference viscosity, Q is the activation energy, and R is the universal gas constant.

Table 6. Parameters and variable used in this study.

Name	Symbol	Value	Unit
Coordinates	x,y,x		km
Imposed half spreading rate	U_0	55	mm/yr
Mantle velocity	V		mm/yr
Pressure	P		Pa
Temperature	T		˚C
Temperature at the surface of thermal model	T_m	1350	˚C
Mantle Potential Temperature	T_0	0	˚C
Effective thermal conductivity	k		W/K·m
Specific heat capacity	C_p	$1.25x10^3$	J/kg·K
Reference mantle density	ρ	3300	kg/cm^3
Activation energy	Q	250	kJ/mol
Universal gas constant	R	8.314	J/K·mol
Viscosity	η		Pa·s
Reference viscosity	η_0	10^{19}	Pa·s

8.3.2 Gravity processing

Shipboard gravity data were analyzed in order to understand the distribution of mass anomalies near the Earth's surface in the context of the 8˚20'N seamounts-EPR-Siqueiros Transform geodynamic setting. We followed the method described in Kuo & Forsyth, (1988). Starting from the FAA calculations performed at sea, we constructed the FAA map: we interpolated the gravity data on track-lines into 0.25 km spaced grids using a tension continuous curvature surface gridding algorithm (Figure 42a). The FAA range from -25 to 17 mgal. The lowest anomalies occur along the trace of the Siqueiros Fracture Zone; highest values are found in areas close to the ridge and along the 8˚20'N seamount chain, with a local high around Liona Seamount. This indicates that the topography or the water crust interface is the most important contributor to the FAA. We adopted the forward modelling approach of Prince and Forsyth (1998), to separate the effects of the different components contributing to the gravity signal: seafloor topography, Moho relief and 3D mantle thermal structure.

Parker's (1973) method was used to convert the elevation profile, from the multibeam data, and the density contrast to evaluate their gravity signal. For the water-crust interface we assumed a density of 1.03 g/cm^3 for the water and a density of 2.73 g/cm^3 for the crust. In order to estimate the attraction of the Moho, we assumed a constant crustal thickness of 6 km and a mantle density of 3.3 g/cm^3. The gravity map obtained adding the signal from the seafloor topography and the one from the Moho predicts the effect in and above the oceanic crust, with no topographic effects (Gregg et al., 2007; Kuo and Forsyth, 1988; Lin et al., 1990). We interpolated these data with the same criteria adopted for the FAA, in order to generate the map of the Mantle Bouguer Anomalies (MBA). The MBA show progressive lower values approaching the ridge, in a range between -20 and 20 mgal, indicating how the dominant component of the anomalies is the density variations associated to the thermal structure in the ridge-transform scenario (Figure 42b). The MBA is caused by variation in crustal thickness and the temperature and density structure of the mantle.

As the thermal effect of the aging lithosphere is significant, calculating a Residual Mantle Bouguer Anomalies (RMBA), which incorporates thermal subsidence, is necessary.

The 3D upwelling mantle model, described in 4.1, is used to provide the temperature predictions for discrete horizontal layers at increasing depths (Figure 43). Temperature is then converted into density variations to provide the predicted gravity signal observed at sea level, thus producing the RMBA correction (Kuo and Forsyth, 1998). The total signal, given by the stacking of each layer, is in accordance to the thermal structure of the ridge-transform domain. The minimum values, around -20 mgal are along the ridge axis, while the highest values are found moving away from it, up to 60 mgal. The RMBA correction subtracted from the MBA, obtaining the RMBA (Figure 42c).

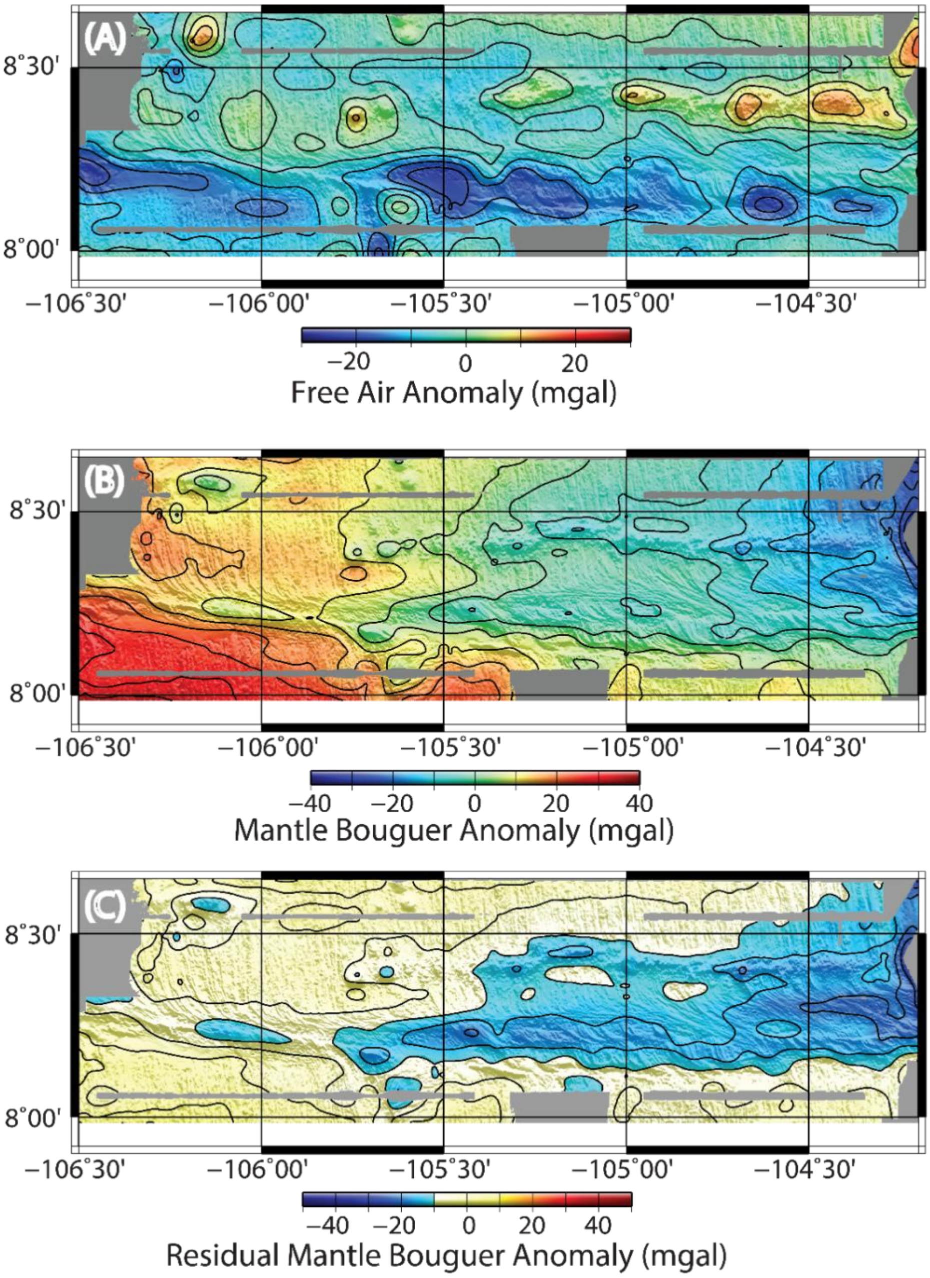

Figure 42.a) Free Air Anomaly Map calculated filtering raw data using low-pass Butterworth filter and correcting for Eötvös and drift effects; b) Mantle Bouguer Anomaly map, calculated removing the effects of seafloor topography and a reference 6 km-thick crust; c) a Residual Mantle Bouguer Anomaly is calculated by removing the effects of lithospheric cooling as estimated from the three-dimensional passive mantle flow thermal model (see section 4.1 for details).

8.3.3 Gravity-derived elastic plate thickness

The response of the lithosphere to an applied load is related to its rigidity an is hence tied to its age and thermal structure (Koppers and Watts, 2010). The FAA, is used in combination with the thermal structure of the region and bathymetric data to determine the spatial variation in the oceanic elastic thickness and the relative differences in compensation at the proximal and distal portion of the seamount chain. In the Fourier transform domain, the relation between the topography, gravity and the gravitational admittance is given by (Watts, 1978, 2001):

$$Z(k) = \frac{output}{input} = \frac{\Delta g(k)}{H(k)} \tag{30}$$

where $Z(k)$ is the gravitational admittance, $\Delta g(k)$ are the discrete Fourier transform of the observed free air anomaly and the topography, k is the wavenumber (2π/wavelength).

The elastic thickness is calculated for different profiles along the chain, over the main seamount edifices recognized. The elastic thickness was computed based on Watts, (2001), where the gravitational admittance is given by:

$$Z(k)_{flex} = 2\pi G(\rho_l - \rho_w)e^{-kd}\left\{1 - \varphi_e'(k)\frac{((\rho_c)+(\rho_m-\rho_c)e^{-kt})}{(\rho_m)}\right\} \tag{31}$$

where $\varphi_e'(k) = \left[\frac{Dk^4}{(\rho_m-\rho_c)g} + 1\right]^{-1}$, G is the gravitational constant, ρ_l is the density of the load, ρ_w is the density of the water, ρ_c, is the density of the crust, ρ_m is the density of the mantle, d is the mean water depth, t is the mean thickness of the crust and D is the flexural rigidity, given by:

$$D = \frac{ET_e^3}{12(1-\nu^2)} \tag{32}$$

where E is the Young's modulus and ν is the Poisson's ratio, T_e is the elastic thickness. We used an iterative RMS square method to minimize the error between the observed value of the FAA and the gravity computed according to eq. (5), using as variables the elastic thickness and the density of the load. According to the thermal model described in section 4.1, profiles of the isotherms relative to the 400 and 600 ˚C are plotted to provide a range in the brittle layer thickness (Figure 5). For each seamount, the values corresponding to the brittle layer thickness (as estimated by the 400 and 600 ˚C isotherm) is used as range to constrain the search of the optimal elastic thickness. Other parameters used in the calculation are shown in Table 7:

Table 7. Parameters used in this study.

Name	Symbol	Value	Unit
Gravitational constant	G	6.67408×10^{-11}	$km^3/kg \cdot s^2$
Density of the water	ρ_w	1030	kg/m^3
Density of the crust	ρ_c	2900	kg/m^3
Density of the mantle	ρ_m	3300	kg/m^3
Mean thickness of the water	d	3000	m
Mean thickness of the crust	t	6000	m
Young modulus	E	70×10^9	Pa
Poisson ratio	ν	0.25	

The values of plate elastic thickness are used to infer the age of the lithosphere at the time of loading, which is compared to the age of the seafloor at the present time. This has strong implication on the geodynamic model used to explain how the chain forms; if the seamounts were drafted from the ridge axis along with the underneath oceanic lithosphere or if they formed in a different time.

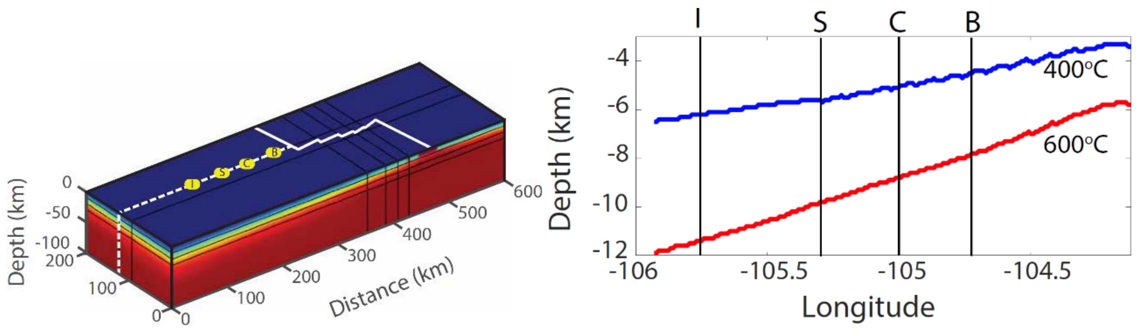

Figure 43. On the left, same thermal model described in figure 3, used to provide the temperature predictions for discrete horizontal layers at increasing depths, with the location of the seamounts used to evaluate the trend of the elastic thickness. On the right the 400° and 600° C isotherms are plotted from the trace profile in Figure 5 to provide potential elastic thicknesses (Te) if the seamounts formed in situ.

8.3.4 Magnetic data processing

The magnetic data processed at sea are used along with the bathymetry as input to calculate the rock magnetization distribution in the area (Figure 44). We follow the procedure described in Macdonald et al. (1980), using a suite of Matlab® scripts for magnetic data processing provided by Maurice Tivey at http://deeptow.whoi.edu/download.html (Hosford et al., 2003; Tivey, 1994; Tivey and Johnson, 1990; Williams et al., 2008). This inversion method removes from the observed field the effect of the topographic relief, revealing the distribution of crustal magnetization associated with the tectonic setting and to the reversals in polarity of the Earth's field through time. The code uses Parker and Huestis (1974) Fourier inversion method. A constant thickness of the source layer of 0.5 km is assumed, whose upper bound is bathymetry from the multibeam. The layer is assumed with a uniform magnetization and oriented parallel to an axial geocentric dipole field. A bandpass filter for short and long wavelength is applied, of respectively 4 km and 800 km. The 3D magnetization of the area is gridded at 0.25 km, using the same technique adopted for the gravity data.

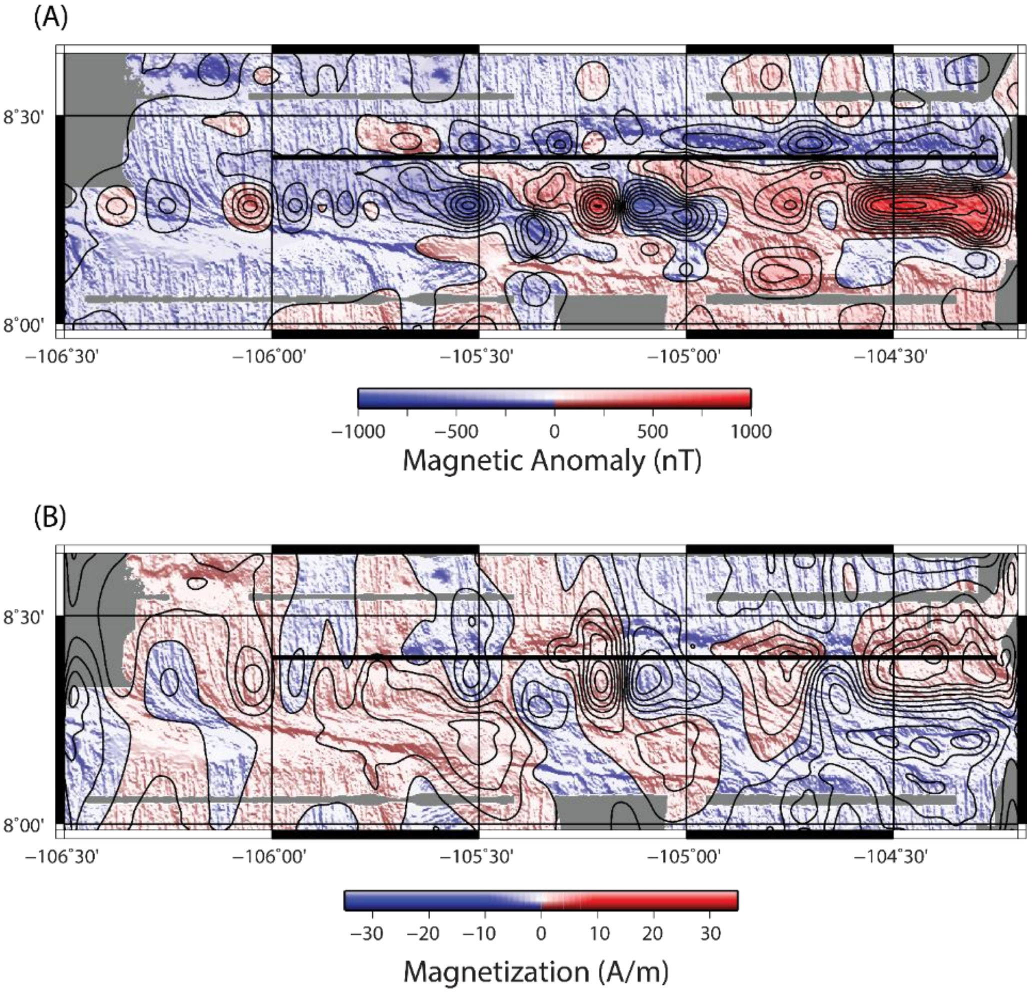

Figure 44. A) The magnetic anomaly is calculated to remove the International Geomagnetic Reference Field (IGRF) of the region; B) Magnetization map has been made removing from the observed field the effect of the topographic relief, and thus revealing the distribution of crustal magnetization associated with the tectonic setting and to the reversals in polarity of the Earth's field through time.

A two-dimensional profile is extracted across the seamount chain to investigate the polarity of the seamounts magnetization with respect to that of the surrounding crust, in order to make a more detailed comparison of the crustal and lithospheric properties and their role in the formation of the seamounts (Figure 45).The data are compared to Carbotte and Macdonald, (1992), in order to ensure reproducibility of the inversion approach, indicating good agreement with their data (Figure 45c).

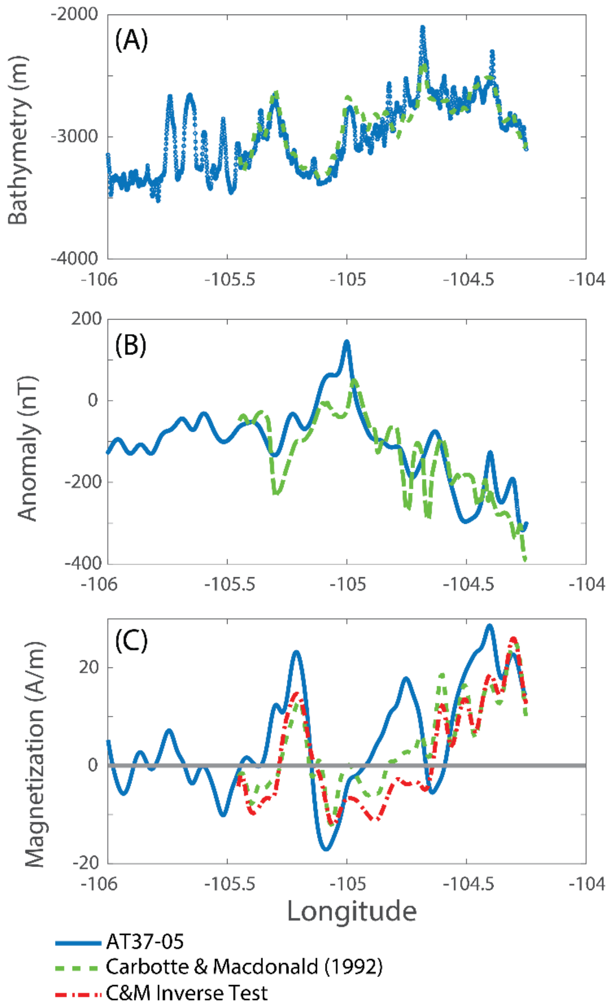

Figure 45. The Carbotte and Macdonald (1992) magnetic anomaly observations are inverted and compared to their 1992 results to ensure reproducibility to our observation approach; a) bathymetric profiles; b) observed anomaly; c) calculated magnetization, that shows good agreement between the three inversions.

8.4 Results

8.4.1 Elastic Plate Thickness

Elastic thickness (Te) estimates are calculated for B-Beryl, C-Coral, S-Sparky, and I-Ivy (as indicated in Figure 43) to investigate variations associated with the seamount chain given their location and predicted lithospheric thickness (Figure 46). We focus on fitting the elastic plate thickness along the profile running northward of the seamount (all plots are south to north), because of the influence of the fracture zone to the south. Best fit estimations are bolded. The estimated Te values are consistently thicker than what would be predicted if the seamounts were emplaced near the ridge axis (Te ~ 5km, Figure 43). However, it does not appear that all the seamounts have formed *in situ*. For example, model predictions for Sparky and Beryl give similar Te estimated suggesting that Sparky may have formed further to the East. Coral's relative high Te value may indicate that it has formed in place at ~105˚ or that the 600 ˚C may be a low estimate for the brittle-ductile transition in this region. Unfortunately, lack of multibeam data north of Ivy limited our ability to model its Te. To gain better Te calculations for the distal seamounts, additional northward lies are necessary to provide sufficient data for the inversion.

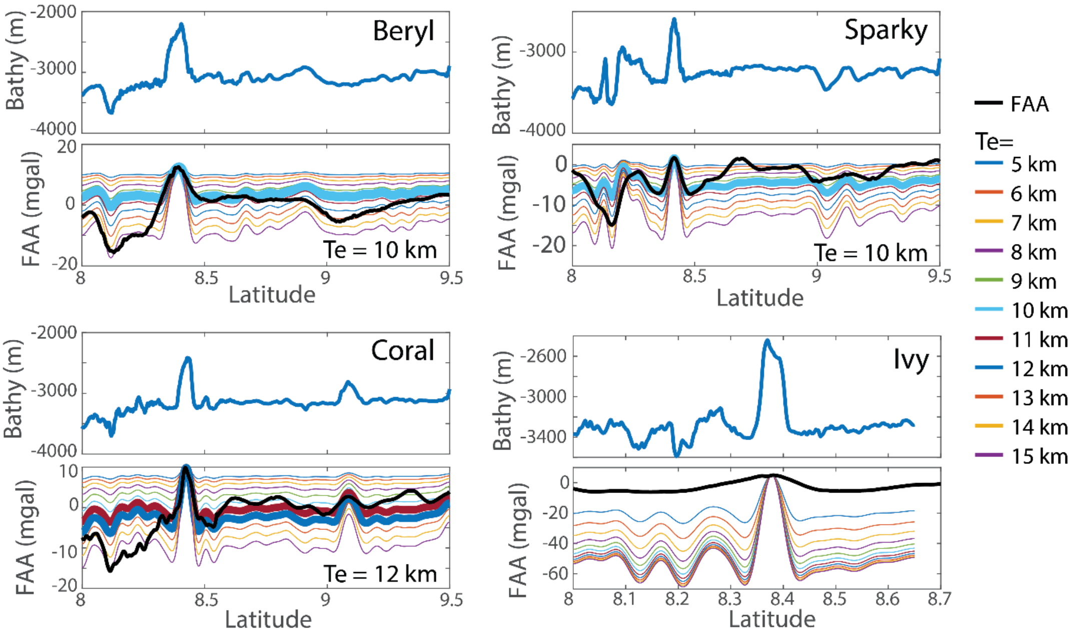

Figure 46. Using Watts et al., (1978), Te estimates are calculated for B-Beryl, C-Coral, S-Sparky and I-Ivy. Model predictions for Sparky and Beryl give similar Te estimates suggesting that Sparky may have formed further to the East. Coral's relatively high Te value may indicate that it has formed in place at ~105W. Each profile is disrupted to the south by the Siqueiros Fracture Zone, as such, the model was fit to the FAA profile to the north. Unfortunately, lack of multibeam data north of Ivy limited our ability to model its Te.

8.4.2 RMBA-Derived Crustal Thickness

The RMBA map, obtained by subtracting the regional component to the observed field, shows a good match with the structural units, with the residual anomalies following the trend of the seamount chain and the fracture zone. The residual gravity field is interpreted in terms of anomalous crustal thickness variations with a calculated range of 0.5 to 1 km (Figure 47). The variations in crustal thickness suggest an increase in melt flux eastward along the chain, with high emplacement volumes observed east of -105˚20’ W, ~130 km from the ridge axis corresponding with lithosphere younger than 2 Myr.

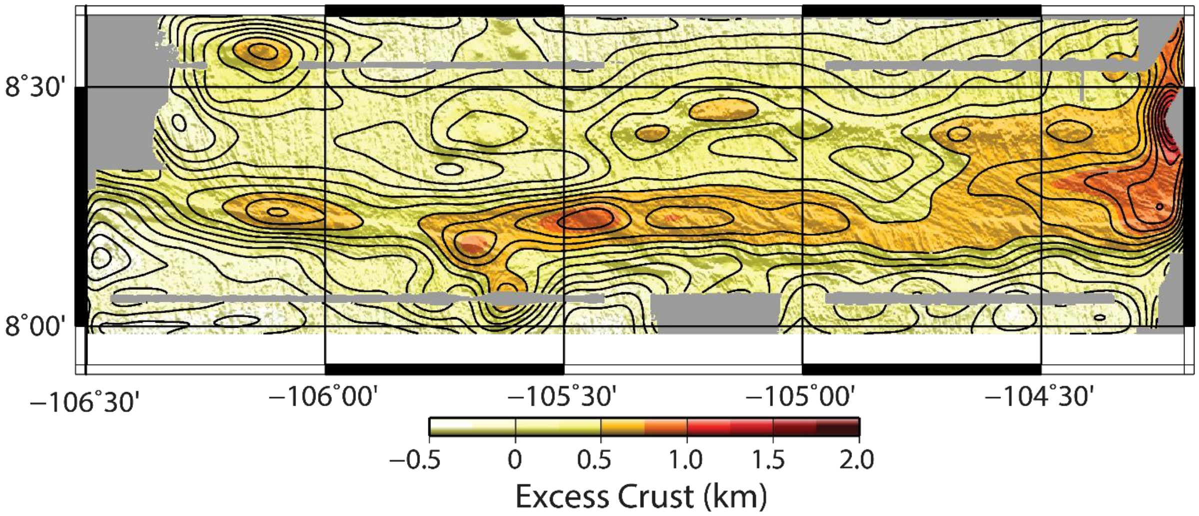

Figure 47. Map of crustal thickness variation in the 8˚20’N seamount area, obtained by subtracting the regional component of the gravity to the observed field. The map indicates an increase in crustal production toward the ridge axis, located ~104.2W.

8.4.3 Magnetization

Inverted three-dimensional magnetization data indicate that the seamounts have recorded a series of magnetic reversals along the chain (Figure 48). If the seamounts were age progressive and formed nearer the axis than their current location their magnetic reversals should correlate to those recorded in the crust they are emplaced on. Portions of the chain between -105 W and -104.7 W indicate that the seamounts may be younger than their surrounding seafloor, as shown comparing seamount magnetization and the magnetic field alignment of the seafloor. The geophysical observations indicate an age progressive nature for the overall seamount chain, but also coeval volcanism in a region 15-100 km from the EPR.

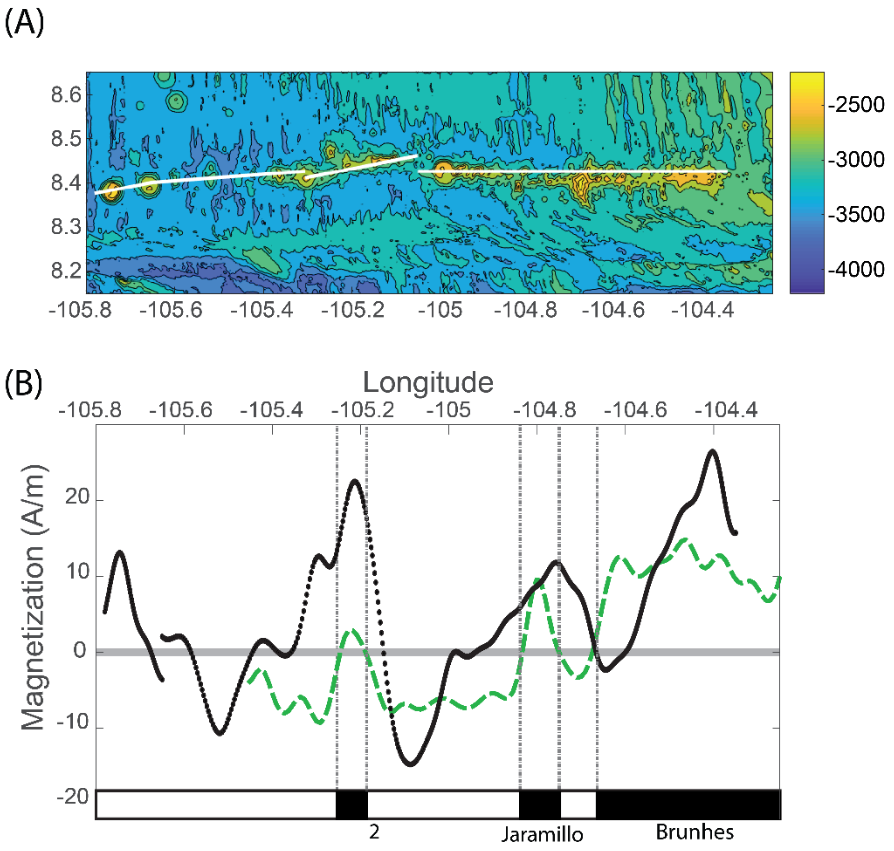

Figure 48. A) Trace of the profiles; B) Seamount magnetization (black dots) taken along the tracks above, is compared to observed reversals from Carbotte and Macdonald (1992). The black bars indicate normal or positive polarity matching the current magnetic field alignment. White bars indicate reverse polarization. The green dashed line is Carbotte and Macdonald (1992) magnetization at 8.7 N.

8.5 Discussion

The main questions that arise from the results concern the time and mechanism of emplacement of the seamounts. The age progressive or coeval nature of these volcanoes has strong implications on the geodynamic model used to explain the melt migration in the Siqueiros fracture zone region feeding the seamount chain. A full analysis of the geophysical observations indicates that the seamounts rest somewhere between the two end members, exhibiting both coeval and age progressive volcanism. In fact, the volcanoes show from several evidences a progressive nature West of -105˚W and a coeval nature moving East from -105˚W. The seamounts are characterized by the passage from discrete edifices to a continuum ridge morphology moving toward the EPR axis, along with an increase in the crustal production in the same direction. Not all the seamounts show an “in situ” formation, as evidenced from the calculated values of the elastic plate thickness Te for Sparky and Beryl seamounts. Magnetic data does not show a matching to the magnetization of the seafloor East of -105˚W, suggesting a more complicated emplacement history and the potential for long-lived and coeval volcanism along the chain. Previous studies evidenced a high reflectivity on the side scan sonar record along the seamount chain (Carbotte and McDonald, 1992; Carbotte et al., 1991; Scheirer and Macdonald, 1995), attributed to the presence of glass. Alvin dives and dredging showed a huge presence of manganese, that is the main cause of the observed high reflectivity. The manganese rinds are thicker and harder to sample in most distal seamounts, while glass is present in a higher amount in the outcrops toward the ridge axis. Besides during dive AL4855, at the base of Hook ridge, 35 km from EPR ridge axis, tubeworms casings, *Tevnia jerichonana* were observed (Figure 49).

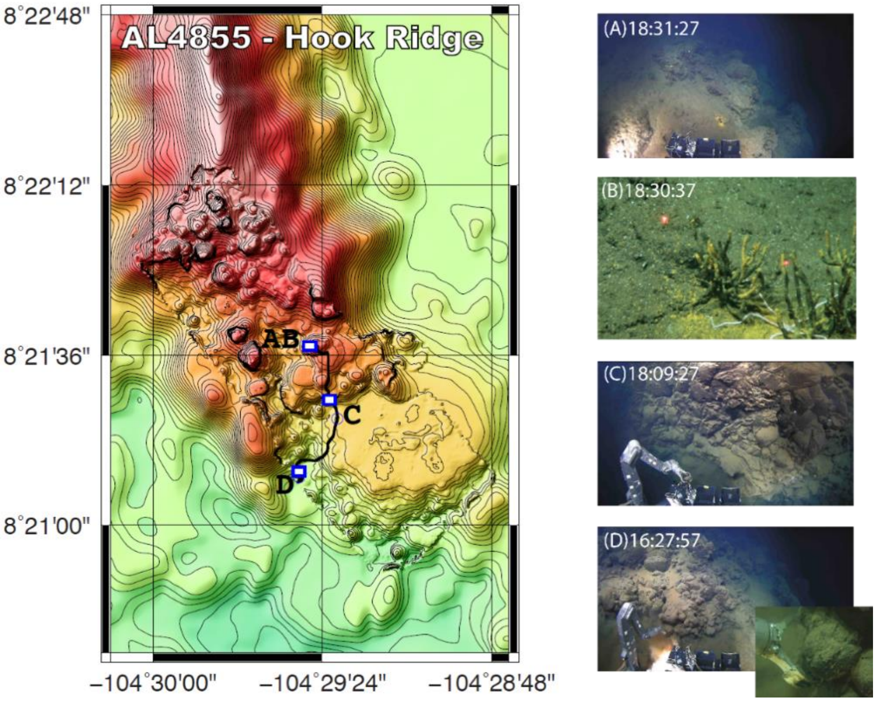

Figure 49. Left: Map of Hook Ridge, located ~35km from the EPR axis, with the location of some images (A-D, right figure) acquired during AL4855. Right: A) Area of hydrothermal sediments and inactive tubeworms; B) Close up of Tevnia jerichonana tubeworms. These organisms indicate recent volcanism (within 2.5 Ma, Ravaux et al. (2003)) in the area, since they are considered first colonizer in the 9N region (Moore et al. 2009; Luther et al. 2012); C) Small pillow bud sampled during the dive; D) Lobate to sheet lava form interbedded in pillows, along a near vertical constructional pillow wall, with a close up of a sample collected during the dive.

These organisms are a biological evidence of recent volcanic activity, since they are considered first colonizer in the 9˚N region (Moore et al., 2009; Luther et al., 2012). Ravaux et al., (2003) conducted experiments with tubeworm chitin that suggest they will denigrate within 2.5 years in deep marine environments.

The geodynamic model that can be used to explain the formation of the seamount chain is related to the tectonic evolution of the Siqueiros Transform Fault. In fact, the seamounts chain does not follow a hotspot reference frame, but instead runs parallel to the fracture zone, at a constant distance. This observation is unusual, compared to the other seamounts in the region. Besides, evidences of plate direction rotation in variation of the main trend of the chain can be observed. They can be attributed to events of plate rotations that characterized the evolution of the Siqueiros Transform Fault as according to Pockanly et al. 1997: the seamount chain may have formed with the first event of plate reorganization from 3.5 Ma, with the inset of the volcanism close to the RTI (Figure 50). If the above hypotheses are valid, we could think about a melt migration model that considers the tectonic evolution of the area, pointing out the role of a stress concentration in the vicinity of the RTI as triggering mechanism for the volcanism.

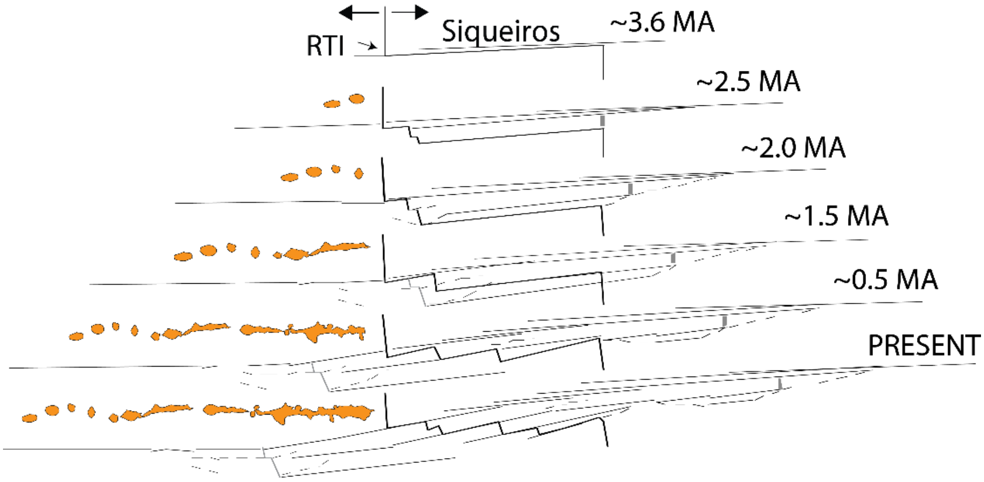

Figure 50. The seamounts are shown appearing as the plate reorganized during the past 3.6 Ma. Adapted from Pockalny et al. (1997), the seamounts corresponding to the age of the crust on which they were emplaced are shown for each time step.

8.6 Conclusions

The OASIS (Off-Axis Seamount Investigations at Siqueiros) expedition is a multidisciplinary effort to systematically investigate the 8˚20’N Seamount Chain to better understand the melting processes in the southern portion of the 9˚-10˚N segment of the East Pacific Rise (EPR). While the geophysical observations indicate that the overall seamounts chain is age progressive, they suggest coeval volcanism in a region 15-100 km from the EPR. The seamounts do not follow absolute plate motions, but are located consistently 15-20km north of the Siqueiros fracture zone, which further suggests that their formation is linked to the location and tectonic evolution of the Siqueiros-EPR-ridge-transform intersection. Excess crustal thickness variations of 0.5 to 1 km, derived from Residual mantle Bouguer Anomaly suggest and increase in the melt flux and in the volume of magma emplaced eastward along the chain. This can be linked also to the morphology of the seamounts, characterized by discrete edifices in the distal portions of the chain and by a continuum ridge toward the EPR axis. Magnetization recorded along the 8˚20’N Seamounts suggest a complicated emplacement history, potentially related to long-lived and coeval volcanism along the chain. These findings have implications for the melt region sourcing the EPR as well as how melt is transported near a fracture zone.

9. The big picture: the role of fluid in geologic processes

Application of fluid mechanics to geology spans from rivers, magma ascent into the crust, lava flows, geysers, glaciers, oil, gas, induced seismicity, sand waves and so on. All these applications depend mainly on the physical properties of the fluid and the geological context under consideration.

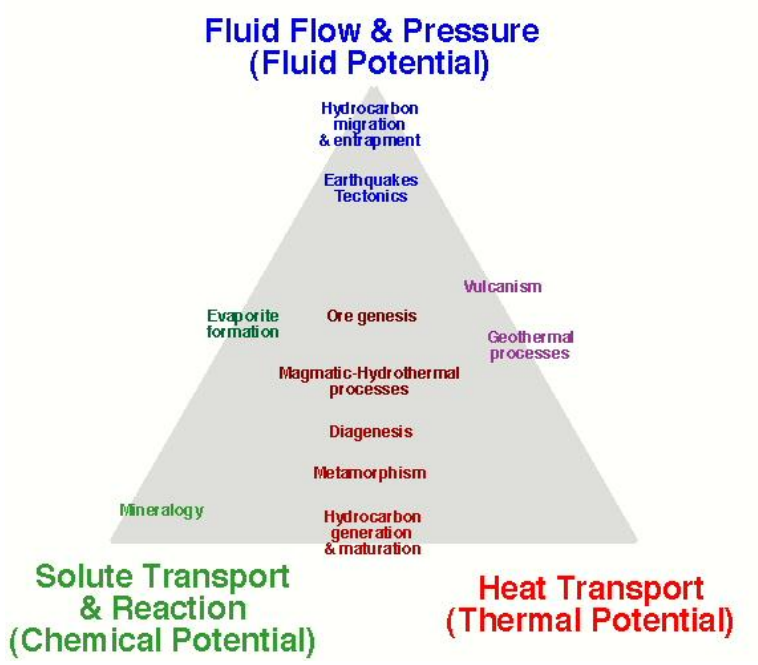

Figure 51. Big picture of the role of fluids in most of geological processes.

I worked on two cases involving different fluids at different scale tectonic structures: in the first case modeling the flow of CO_2 in a fault zone at the scale of tens of meters, in the second one interpreting the geophysical signature of a chain of volcanoes formed from the migration of melts along a fracture zone at the scale of hundreds of kilometers.

My work on the modeling of fluid flow in a fault zone finds a strong application in the context of Carbon Capture & Storage (CCS) techniques. Research conducted over the last 20 years indicates that geological storage of anthropogenic CO_2, together with other approaches, can significantly contribute to the reduction of this gas concentration in the atmosphere (up to 14% according to IPCC, 2005 and IPCC, 2007). In a geological CO_2 storage site, the main migration pathways in case of leakage would be compromised boreholes or gas permeable faults or fractures. The improvement of models able to describe the impact of faults and fractures on the migration of CO_2 is a fundamental step in the choice of the appropriate storage site and reduce the risks associated to the CO_2 sequestration. I proposed a workflow combining detailed geological observations and numerical modeling that can be also applied to other scenarios, involving different fracture systems, faults, and type of rocks. This will lead to models on the CO_2 flow in the fault zone considering also the case of injection supercritical CO_2 and the mineral reactions that have place in this context.

The inaccessibility of the mantle to direct observations, make geodynamic models a fundamental tool to study the processes governing mantle dynamics at Mid Ocean Ridges. Geodynamic models allow us to test governing parameters and investigates physical hypotheses and conceptual models derived from geological, geophysical, and geochemical observation (Gregg et al, 2012). The formation and development of seamount chains that extend away from mid-ocean ridge spreading centers provide a unique opportunity to probe the three-dimensional mantle melt region feeding an adjacent ridge segment. My work on the geophysical data analysis on the 8˚20’N seamount have strong implications for the melt region sourcing the EPR as well as how melt is transported near a fracture zone. The natural evolution of this work will be the modeling of melt migration describing the formation, transport and composition of the melts feeding the 8˚20’N seamount chain.

Appendix

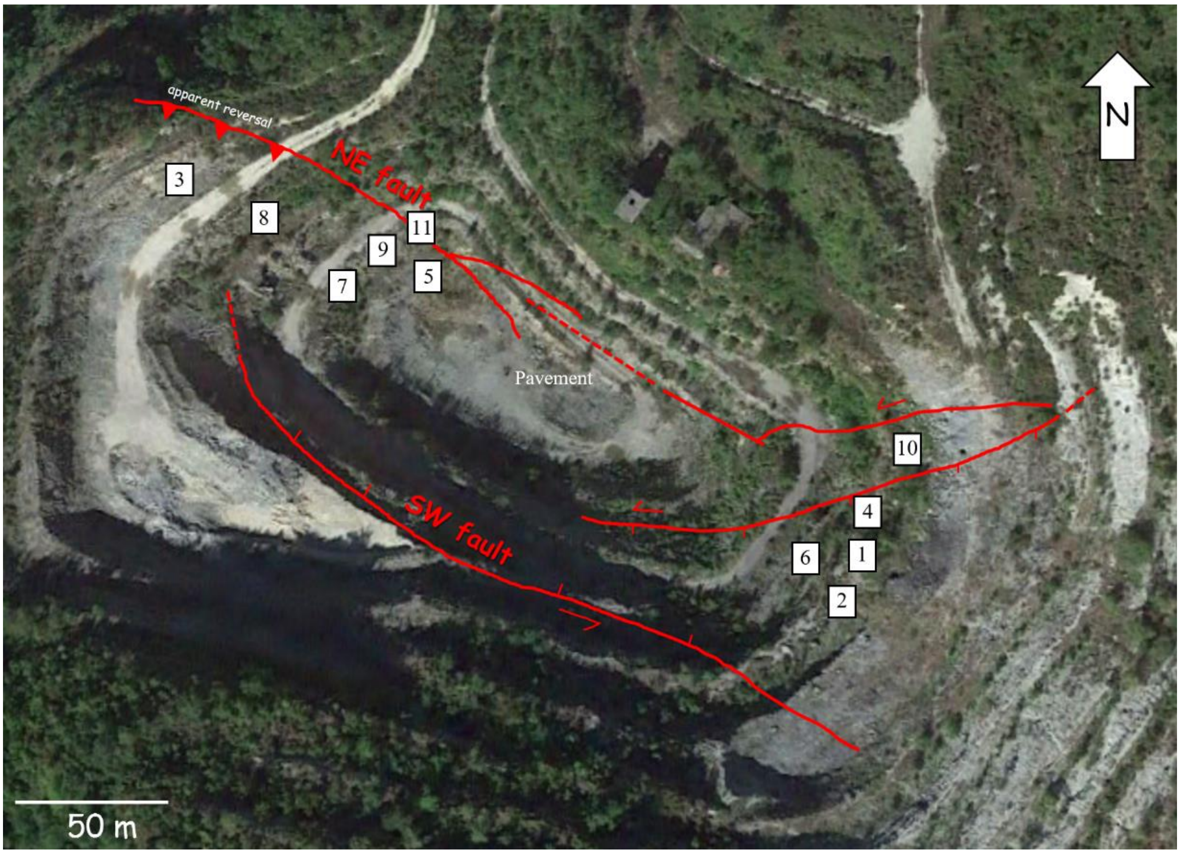

Figure 52. Aerial view of the Roman Valley Quarry with the location of the scan lines.

Table 8. Scan lines of the data acquired along the scan lines. Legend of the symbols: ↑=up, ↓=down, F=fracture, R=Rock, S=strata, FA=fault ?=not defined, V=void, C=calcite, T=tar, A=other

SCAN LINE 1 --- orientation N30°

Measure	**Distance from zero**	**Dip**	**Azimuth**	**Length up (cm)**	**Length down (cm)**	**Termination**	**Aperture (mm)**	**Filling**
1	19	190°	55°	15	50	↑S↓?	0,2	T
2	30	190°	68°	7	3	↑S↓F	0,15	V
3	33	210°	65°	0	7	↑F↓F	0,15	V
4	39	205°	85°	7	26	↑S↓S	0,2	V
5	42	210°	58°	2	2	↑F↓R	0,1	V
6	62	190°	43°	5	6	↑F↓F	0,5	V
7	6	195°	60°	1	8	↑R↓F	0,1	V
8	77	195°	62°	1	20	↑R↓S	0,1	V
9	90	220°	80°	55	14	↑?↓S	0,1	V
10	100	190°	70°	25	12	↑S↓S	0,1	V
11	103	210°	80°	1	11	↑F↓S	0,1	V
12	110	210°	75°	3	9	↑F↓S	0,1	V
13	118	215°	82°	6	6	↑F↓S	0,1	T
14	131	215°	60°	10	40	↑F↓R		T
15	146	210°	70°	10	40	↑R↓R		T
16	154	215°	45°	37	21	↑R↓R	0,1	T
17	164	195°	60°	40	2	↑R↓R	0,1	T
18	171	195°	66°	0	6	↑F ↓R	0,1	T

19	173	195°	66°	2	7	↑F ↓R	0,2	T
20	188	195°	70°	28	14	↑R ↓S	0,15	T
21	195	205°	71°	14	40	↑F ↓R	0,15	T
22	210	210°	65°	200	150	↑FA ↓?	0,1	T
23	665	210°	48°	15	10	↑FA ↓S	0,5	T
24	675	190°	70°	12	6,5	↑S↓S	0,1	V
25	683	30°	27°	300	5	↑S↓S	0,1	V
26	692	187°	47°	5	7	↑S↓S	0,5	T
27	697	193°	54°	65	3	↑?↓FA	0,1	V
28	700	190°	59°	9	1	↑S ↓S	0,1	T
29	702	30°	25°	300	50	↑FA↓F	0,2	V
30	710	185°	60°	3	56	↑R↓?	0,1	V
31	714	30°	25°	300	5	↑ ↓S	0,1	V
32	720	190°	62°	36	40	↑FA ↓FA	0,3	V
33	728	200°	46°	0	12	↑?↓S	0,1	V
34	730	30°	25°	80	80	↑?↓S	0,5	T
35	731	200°	45°	40	9,5	↑? ↓S	0,5	T
36	736	210°	87°	65	6	↑? ↓F	0,1	V
37	740	190°	67°	60	47	↑S ↓F	0,5	T
38	745	25°	35°	300	18	↑? ↓F	0,1	V
39	749	209°	65°	2	2	↑S ↓R	0,1	V
40	753	25°	35°	200	7	↑? ↓S	0,1	A
41	759	20°	80°	10	13	↑S ↓R	0,1	V
42	763	210°	65°	60	36	↑S ↓S	0,2	T
43	766	60°	85°	7	10	↑? ↓S	0,1	V

44	773	190°	64°	17	31	↑S ↓S	0,5	T
45	784	200°	61°	100	30	↑? ↓F	0,2	V
46	789	190°	71°	47	23	↑F ↓R	0,2	V
47	790	25°	40°	150	12	↑S ↓S	0,5	A
48	796	30°	60°	7	19	↑F ↓S	0,3	A
49	800	190°	46°	100	18	↑S ↓S	0.1	A
50	801	10°	83°	20	20	↑R ↓S	0,1	V
51	820	195°	75°	34	15	↑F ↓S	0,1	V
52	827	190°	71°	16	14	↑F ↓S	0,1	V
53	840	205°	64°	45	1	↑? ↓FA	0,3	V
54	842	220°	55°	40	4	↑?↓FA	0,1	V
55	846	30°	25°	20	150	↑?↓S	0,2	A
56	880	30°	25°	20	150	↑? ↓S	0,2	A

SCAN LINE 2 --- orientation N30˚

Measure	**Distance from zero**	**Dip**	**Azimuth**	**Length up (cm)**	**Length down (cm)**	**Termination**	**Aperture (mm)**	**Filling**
1	0	237°	88°	7,5	7	↑S ↓S	0,1	V
2	3	215°	60°	2	8	↑F ↓S	0,1	V
3	8	198°	45°	15	65	↑S ↓S	1	V
4	20	210°	34°	4	4,5	↑F ↓S	2	V
5	24	216°	25°	15	66	↑S ↓S	0,1	V

6	27	30°	30°					A
7	33	215°	89°	6,5	4	↑S ↓S	0,5	V
8	38	224°	67°	5	2	↑S ↓S	0,1	V
9	41	210°	89°	11	24	↑F ↓F	0,1	V
10	51	208°	65°	?	11	↑? ↓F	0,1	V
11	59	198°	62°	15	3	↑S ↓S	0,1	V
12	62	196°	60°	3,5	61	↑S ↓S	2	V
13	66	23°	80°	22	1	↑S ↓F	1	V
14	82	180°	55°	10	25	↑S ↓S	0,5	V
15	95	220°	83°	35	20	↑S ↓S	0,2	V
16	160	175°	70°	0	24	↑S ↓S		
17	160	75°	70°	0	24	↑S ↓S		
18	216	5°	85°	15	0	↑S ↓S		
19	237	228°	80°	14	0	↑S ↓S		
20	250	130°	85°	8,5	10,5	↑S ↓S		
21	251	185°	60°	8,5	10,5	↑S ↓S	0,1	V
22	307	245°	80°	20	3	↑S ↓S	0,5	V
23	315	180°	80°	5	0	↑S ↓S		
24	328	100°	85°	5	10	↑S ↓S		
25	331	180°	70°	20	7	↑S ↓S	0,5	V
26	346	85°	75°	20	3	↑S ↓S		
27	360	182°	80°	24	3	↑S ↓S	0,1	V
28	377	200°	89°	0	60	↑S ↓?		
29	388	120°	85°	0	15	↑S ↓?		

SCAN LINE 3 --- orientation N60°

Measure	Distance from zero	Dip	Azimuth	Length up (cm)	Length down (cm)	Termination	Aperture (mm)	Filling
1	14	40°	80°	13	6	↑S ↓S	0,1	O
2	38	180°	90°	15	10	↑S ↓S	0,1	O
3	55	270°	70°	39	25	↑S ↓S	0,3	O
4	68	80°	65°	1	15	↑F ↓S	0,2	V
5	70	110°	65°	35	14	↑S ↓S	0,1	O
6	100	90°	90°	15	14	↑S ↓S	0,2	O
7	102	195°	56°	18	14	↑S ↓S	0,1	O
8	110	255°	75°	5	25	↑S ↓S	0,2	O
9	120	255°	77°	6	13	↑S ↓R	0,2	O
10	140	300°	75°	7	23	↑S ↓S	0,2	O
11	144	110°	75°	8	11	↑S ↓S	0,1	O
12	160	40°	62°	6	14	↑S ↓S	0,15	O
13	180	60°	65°	6	15	↑S ↓S	0,1	C
14	216	270°	70°	2	18	↑S ↓S		
15	240	205°	90°	4	14	↑S ↓S	0,15	O
16	252	180°	80°	2	18	↑S ↓S	0,2	V
17	260	270°	60°					
18	286	270°	75°					
19	315	220°	75°	25	40	↑FA ↓FA	0,15	V
20	327	60°	70°	12	15	↑R ↓?	0,15	V
21	338	60°	60°	4	14	↑R ↓F	0,15	T

22	345	35°	60°	40	13	↑FA ↓F		T
23	358	170°	15°	9	6	↑F ↓F	0,3	O
24	362	90°	60°	10	15	↑F ↓F	0,1	V
25	370	30°	65°	45	50	↑FA ↓R		T
26	372	180°	55°	3	45	↑R ↓R	0,1	O
27	382	220°	65°	5	5	↑F ↓R	0,1	O
28	387	120°	60°	20	54	↑F ↓F	0,2	O
29	390	170°	59°	12	10	↑F ↓F	0,1	C
30	425	90°	90°	0	26	↑ ↓F	0,4	V
31	426	180°	86°	60	100	↑F ↓?	0,3	V
32	446	240°	50°	0	19	↑? ↓F		
33	506	190°	60°			↑ ↓		
34	520	180°	55°	10	9	↑F ↓F		
35	533	190°	58°	1	4	↑R ↓R	0,1	O
36	539	250°	61°	3	30	↑F ↓F		O
37	545	210°	62°	3	30	↑F ↓F		O
38	573	60°	59°	27	26	↑S ↓F	0,2	O
39	633	70°	90°	18	11	↑S ↓?	0,1	O
40	634	90°	90°	18	11	↑S ↓?	0,1	O
41	644	180°	90°	20	10	↑S ↓?	0,2	O
42	704	360°	90°	7	10	↑S ↓?	0,1	O
43	726	195°	75°	0	12	↑S ↓F	0,1	V
44	735	203°	89°	9	?	↑S ↓?		V
45	755	199°	80°	10	6,5	↑S ↓S		V
46	756	115°	89°	10	8	↑S ↓S		

47	775	196°	70°	12	7	↑S ↓S		
48	787	194°	80°	7	16	↑S ↓S	0,1	V
49	800	185°	85°	12	20	↑S ↓S	0,5	V
50	805	245°	85°	12	?	↑S ↓?		
51	850	174°	75°	10	15	↑S ↓S		
52	882	255°	65°	50	18	↑S ↓S		
53	905	118°	75°	42	19	↑S ↓S	0,2	V
54	910	185°	85°	40	18	↑S ↓S	0,2	V
55	952	182°	84°	37	18	↑S ↓S	0,2	V
56	993	209°	58°	22,5	35	↑S ↓FA	0,5	V
57	1003	210°	35°	3,5	20	↑S ↓FA	2	V
58	1009	45°	75°	5	6	↑F ↓F	0,1	V
59	1020	213°	88°					
60	1031	185°	85°	25	2	↑FA ↓S	0,5	V
61	1037	186°	70°	27	2	↑FA ↓S	1,5	V
62	1053	196°	65°	21	2	↑F ↓S	1,5	V
63	1059	360°	85°	12	1	↑S ↓F	0,5	V
64	1063	195°	86°	50	20	↑F ↓R	0,1	V
65	1075	207°	50°	16	12	↑F ↓F	0,1	V
66	1079	50°	80°	16	4,5	↑F ↓F	0,5	V
67	1087	50°	85°	8	3	↑S ↓F	0,1	V
68	1098	230°	89°	24	9	↑S ↓F	0,5	V
69	1101	350°	85°	4	10	↑S ↓F	0,1	V
70	1106	230°	80°	5	10	↑S ↓S	0,1	V
71	1113	170°	70°	6	6	↑S ↓S	0,1	V

72	1115	225°	80°	6	15	↑S ↓F	0,1	V
73	1120	340°	85°	10	5	↑S ↓?	0,1	V
74	1125	240°	85°	2,5	22	↑F ↓S	0,1	V
75	1140	350°	70°	9	2	↑S ↓?	0,5	V
76	1159	198°	89°	9	50	↑F ↓R	0,5	V
77	1170	352°	89°	6	65	↑F ↓S	0,1	V
78	1171	220°	75°	12	10	↑R ↓S	0,2	V
79	1173	170°	50°	10	20	↑F ↓S	0,1	V
	core							
80	1234	218°	60°	61	100	↑S ↓?	0,2	V
81	1239	220°	55°	7	8	↑S ↓S	0,1	V
82	1292	20°	80°	45	20	↑F ↓S	0,4	V
83	1298	180°	70°	10	7	↑F ↓R	0,1	V
84	1308	170°	45°	18	10	↑S ↓S	0,1	V
85	1313	20°	85°	9	12	↑F ↓S	0,1	V
86	1336	190°	50°	55	30	↑S ↓S	0,5	T
87	1349	260°	65°	40	18	↑S ↓?	0,5	T
88	1360	175°	60°	40	26	↑S ↓S	0,4	T

SCAN LINE 4 --- orientation N40°

Measure	Distance from zero	Dip	Azimuth	Length up (cm)	Length down (cm)	Termination	Aperture (mm)	Filling
1	21	10°	25°	45	20	↑FA ↓?	1	V
2	34	345°	82°	30	5	↑FA ↓?	3	O
3	39	345°	83°	13	10	↑S ↓?	0,1	V
4	52	190°	65°	5	20	↑F ↓?	0,1	V
5	55	205°	65°	1	20	↑S ↓?	0,1	T
6	62	205°	70°	3	13	↑S ↓F	0,1	T
7	71	190°	55°	6	10	↑S ↓?	0,1	T
8	220	180°	45°	20	100	↑FA ↓?		
9	225	10°	42°	10	?	↑F ↓?	0,2	T
10	230	182°	46°	10	50	↑R ↓?	0,15	T
11	253	190°	46°	40	100	↑FA ↓?	0,2	T
12	254	195°	50°	60	100	↑FA ↓?	0,2	T
13	258	220°	75°	20	5	↑F ↓F	0,2	T
14	261	35°	35°	15	5	↑F ↓F	0,1	V
15	270	200°	55°	60	8	↑FA ↓F	0,2	V
16	271	50°	40°	10	5	↑F ↓F	0,1	V
17	280	200°	60°	20	5	↑F ↓R	0,3	T
18	283	203°	85°	10	30	↑F ↓?	0,1	O
19	309	20°	80°	35	5	↑F ↓F	0,6	T
20	320	185°	50°	150	14	↑FA ↓F	0,3-2	T
21	323	175°	60°	150	150	↑FA ↓?	1	T

22	329	165°	50°	20	120	↑F ↓FA	1	O
23	357	182°	55°	220	25	↑FA ↓F	0,5	T
24	360	15°	35°	10	10	↑F ↓F	0,15	V
25	366	16°	35°	14	2	↑F ↓F	0,1	V
26	400	195°	62°	200	100	↑FA ↓FA	0,4	T
27	420	185°	52°	50	100	↑? ↓FA	0,1	V
28	425	195°	70°	25	50	↑F ↓FA	0,6	T
29	650	205°	70°	100	20	↑FA ↓F	0,3	T
30	658	195°	70°	13	5	↑F ↓?	0,1	T
31	663	200°	60°	30	5	↑F ↓?	0,2	T
32	668	200°	55°	10	2	↑R ↓F	0,15	T
33	687	200°	55°	3	8	↑F ↓R	0,15	V
34	693	185°	90°	4	15	↑F ↓?	0,1	V
35	698	195°	75°	4	8	↑F ↓R	0,15	T
36	703	196°	76°	15	10	↑F ↓R	0,15	T
37	716	235°	60°	16	10	↑F ↓?	0,1	T
38	723	215°	66°	5	10	↑F ↓?	0,1	T

SCAN LINE 5 --- orientation N40°

Measure	Distance from zero	Dip	Azimuth	Length up (cm)	Length down (cm)	Termination	Aperture (mm)	Filling
1	60	180°	70°					T
2	97	190°	70°	0	28	↑ ↓S	0,2	T
3	78	120°	90°	10	22	↑F ↓S	0,1	V
4	103	210°	70°	4	32	↑R ↓S	0,1	T
5	130	190°	35°	14	?	↑S ↓?	0,2	T
6	145	160°	50°	?	?	↑? ↓?		T

SCAN LINE 6 --- orientation N35°

Measure	Distance from zero	Dip	Azimuth	Length up (cm)	Length down (cm)	Termination	Aperture (mm)	Filling
1	18	210°	70°	13	19	↑F ↓F	0,15	V
2	24	192°	75°	35	10	↑R ↓S	0,2	V
3	38	185°	82°	10	9	↑F ↓S	0,1	O
4	51	35°	15°	0,5	0,5	↑FA ↓?	0,15	O
5	62	195°	70°	2	10	↑S ↓F	0,2	V
6	66	175°	85°	5	4	↑S ↓F	0,15	O
7	71	40°	65°	15	1	↑F ↓?	0,5	O
8	76	185°	76°	20	6	↑S ↓?	0,1	V
9	77	185°	80°	5	12	↑? ↓F	0,15	O

10	78	30°	90°	4	1	↑F ↓F	0,1	V
11	85	32°	55°	30	20	↑F ↓F	0,1	O
12	96	195°	75°	8	7	↑F ↓F	0,1	O
13	97	200°	75°	10	1	↑F ↓F	0,1	O
14	118	215°	80°	15	1	↑F ↓?	0,1	O
15	120	35°	15°	20	0,5	↑FA ↓?	0,15	O
16	142	200°	90°	2	4	↑F ↓?	1	O
17	150	255°	60°					
18	410	25°	76°	7	10	↑F ↓F	0,1	O
19	428	215°	75°	27	7	↑F ↓F	0,2	V
20	431	205°	75°	10	4	↑S ↓F	0,1	O
21	433	35°	70°	15	20	↑S ↓?	0,1	O
22	437	35°	70°	15	20	↑S ↓?	0,1	O
23	460	260°	80°	8	10	↑S ↓F	0,1	V
24	465	360°	30°					
25	488	220°	90°	40	9	↑F ↓F	2	V
26	506	195°	75°	40	25	↑F ↓F	2	V
27	511	23°	70°	40	4	↑S ↓S	0,2	V
28	517	175°	70°	10	20	↑F ↓?		
29	525	185°	90°	7	30	↑S ↓?	0,3	V
30	530	20°	20°					
31	550	10°	80°	18	35	↑F ↓?	0,4	O
32	558	45°	85°	200	35	↑? ↓?	0,3	O
33	566	35°	15°					
34	578	210°	90°	1	25	↑S ↓?	0,3	T

35	605	195°	75°	14	20	↑F ↓?	0,1	V
36	616	195°	60°	30	20	↑F ↓?	0,1	T
37	618	197°	70°	8	7	↑F ↓F	0,1	V
38	620	200°	88°	4	6	↑F ↓F	0,1	V
39	626	185°	75°	10	4	↑F ↓F	0,1	T
40	628	195°	65°	50	30	↑? ↓?	0,1	O
41	667	35°	75°	12	20	↑F ↓S	0,2	O
42	674	10°	75°	7	20	↑F ↓?	0,1	O
43	710	4°	85°	200	20	↑? ↓?	0,2	T

SCAN LINE 7 --- orientation N60°

Measure	**Distance from zero**	**Dip**	**Azimuth**	**Length up (cm)**	**Length down (cm)**	**Termination**	**Aperture (mm)**	**Filling**
1	6	180°	70°	5	10	↑F↓F	0,2	T
2	8	60°	90°	?	4	↑?↓F		T
3	40	210°	65°	12	7	↑S↓S		V
4	42	90°	90°	12	7	↑S↓S		T
5	48	190°	90°	?	2	↑?↓R		T
6	58	70°	70°	10	50	↑F↓?	0,1	T
7	70	210°	80°	?	50	↑?↓?	0,2	T
8	70	90°	90°	10	48	↑?↓?	0,2	T
9	105	180°	90°	?	3	↑?↓R		V

10	120	210°	70°	2	4	↑?↓R		V
11	140	90°	65°	?	3	↑?↓R	0,1	C
12	144	220°	90°	12	5	↑?↓R		T
13	160	270°	90°	2	37	↑?↓?		T
14	165	120°	80°	0	20	↑?↓?		T
15	234	70°	75°	40	55	↑?↓?	0,2	T
16	252	60°	25°	18	15	↑R↓R	0,2	T
17	278	70°	30°	5	10	↑R↓R	0,2	T
18	298	95°	73°	0	70	↑↓?		T

SCAN LINE 8--- orientation N50°

Measure	**Distance from zero**	**Dip**	**Azimuth**	**Length up (cm)**	**Length down (cm)**	**Termination**	**Aperture (mm)**	**Filling**
1	0	200°	85°					
2	20	110°	39°	20	10	↑F ↓F	0,1	V
3	57	120°	69°	10	30	↑F ↓?	0,5	A
4	180	180°	55°	33	51	↑S ↓?	1,5	T
5	214	360°	80°	27	19	↑S ↓R		
6	214	100°	85°	8	52	↑R ↓S		
7	260	275°	80°	200	80	↑? ↓?		T
8	295	260°	88°	33	15	↑F ↓?	0,5	V
9	298	119°	85°	10	4	↑F ↓F	0,1	V
10	306	325°	90°	46	30	↑F ↓?		T

11	312	285°	80°	40	4	↑S ↓F	0,5	T
12	320	213°	88°	32	10	↑R ↓?	0,1	V
13	332	214°	80°	16	30	↑F ↓F		T
14	340	118°	89°	16	31	↑F ↓F		
15	347	205°	85°	15	8	↑F ↓F		
16	352	115°	85°	18	28	↑F ↓F		T
17	362	215°	77°	11	4	↑F ↓F	0,1	V

SCAN LINE 9--- orientation N70°

Measure	**Distance from zero**	**Dip**	**Azimuth**	**Length up (cm)**	**Length down (cm)**	**Termination**	**Aperture (mm)**	**Filling**
1	40	220°	70°	200	50	↑? ↓?		V
2	47	220°	70°	60	30	↑F ↓F	0,1	V
3	49	200°	60°	10	1	↑F ↓R	0,1	V
4	57	200°	60°	27	2	↑R ↓R	0,1	V
5	60	260°	85°	33	10	↑F ↓R	0,1	V
6	64	270°	85°	62	2	↑F ↓?	1	V
7	76	260°	60°	0	13	↑ ↓F	0,1	V
8	80	220°	73°	36	60	↑F ↓?	0,5	V
9	84	230°	73°	34	15	↑F ↓F	0,1	V
10	93	240°	70°	10	2	↑R ↓?	0,1	V
11	100	250°	70°	17	1	↑R ↓R	0,1	V
12	117	210°	80°	30	0	↑F ↓	0,1	V

13	125	210°	70°	50	5	↑F ↓?	0,5	V
14	135	110°	70°	45	6	↑F ↓R	0,1	V
15	142	210°	90°	17	0	↑F ↓	0,1	V
16	147	100°	90°	27	0	↑? ↓	0,1	V
17	172	180°	90°	39	0	↑F ↓?	0,1	V

SCAN LINE 10--- orientation N30˚

Measure	**Distance from zero**	**Dip**	**Azimuth**	**Length up (cm)**	**Length down (cm)**	**Termination**	**Aperture (mm)**	**Filling**
1	0	40°	46°	12	7	↑F ↓F	0,1	V
2	23	220°	73°	20	36	↑F ↓S	0,2	V
3	32	244°	79°	85	120	↑S ↓?	1,5	T
4	53	220°	86°	38	22	↑S ↓S	0,2	V
5	57	23°	90°	39	20	↑S ↓S	0,1	V
6	69	220°	86°	2	33	↑F ↓F	0,1	V
7	73	207°	70°	21	15	↑S ↓?	0,1	V
8	75	234°	74°	23	120	↑S ↓?		T
9	81	223°	58°	41	120	↑F ↓?	0,1	T
10	100	234°	84°	9	30	↑F ↓S	0,1	V
11	104	220	73	24	32	↑S ↓S	0,1	V
12	130	214°	80°	21	54	↑S ↓F	0,3	T
13	132	187°	90°	48	33	↑R ↓F	0,1	V

14	141	244°	81°	14	60	↑S ↓F	0,5	V
15	149	213°	84°	13	1	↑S ↓F	0,5	V
16	152	260°	90°	12	6	↑S ↓F	0,1	V
17	155	66°	76°	14	11	↑S ↓F	0,1	V
18	156	18°	65°	12	4	↑S ↓F	0,1	V
19	158	266°	85°	12	11	↑S ↓F	0,5	V
20	162	20°	86°	10	22	↑S ↓F	1	V
21	173	190°	85°	110	120	↑S ↓?	1	T
22	187	24°	87°	8	20	↑S ↓F	0,3	V
23	217	37°	50°	3	24	↑F ↓F	0,1	V
24	230	193°	60°	120	67	↑S ↓S	0,3	T
25	248	220°	65°	20	33	↑S ↓S	0,1	V
26	255	26°	86°	13	33	↑F ↓S	0,1	V
27	272	210°	59°	47	30	↑R ↓S	0,1	V
28	292	215°	50°	30	19	↑S ↓F	0,1	V
29	309	204°	70°	21	70	↑S ↓S	0,1	T
30	311	30°	67°	67	100	↑F ↓?	2	T
31	330	220°	70°	20	60	↑S ↓F	0,5	V
32	336	207°	80°	200	100			
	Core							
33	354	241°	80°	17	15	↑S ↓R	0,5	V
34	361	245°	80°	12	19	↑F ↓R	0,1	V
35	376	216°	63°	53	21	↑F ↓R	0,5	V
36	380	37°	89°	16	30	↑S ↓F	0,1	V
37	382	207°	75°	16	11	↑S ↓S	0,1	V

38	391	185°	70°	15	1	↑S ↓R	0,1	V
39	401	195°	65°	70	5	↑F ↓F	0,1	V
40	422	235°	85°	50	10	↑F ↓S	0,1	V
41	424	290°	90°	15	10	↑S ↓S	2	V
42	442	35°	80°	12	55	↑F ↓S	0,1	V
43	460	225°	85°	200	60	↑FA ↓FA	4	T
44	479	25°	89°	140	76	↑FA ↓FA	0,5	T

SCAN LINE 11--- orientation N42°

Measure	**Distance from zero**	**Dip**	**Azimuth**	**Length up (cm)**	**Length down (cm)**	**Termination**	**Aperture (mm)**	**Filling**
1	21	120°	65°	8	16	↑R ↓R	0,5	T
2	34	200°	70°	8	9	↑R ↓F	0,3	T
3	37	170°	80°	3	23	↑R ↓?	0,1	T
4	41	180°	64°	11	5	↑F ↓F	0,3	T
5	44	40°	56°	11	17	↑F ↓R	0,5	T
6	45	190°	66°	12	1	↑F ↓F	0,5	T
7	48	220°	75°	8	9	↑R ↓R	0,1	T
8	109	180°	54°	40	21	↑R ↓?	0,1	T
9	115	260°	75°	30	20	↑R ↓?	0,3	T
10	134	173°	85°	80	26	↑R ↓?	0,5	T
11	139	200	77	40	5	↑F ↓R	0,2	T
12	185	220°	61°	10	11	↑R ↓F	0,3	T

13	194	119°	70°	29	8	↑R ↓F	0,4	T
14	196	60°	58°	2	30	↑F ↓F	0,5	T
15	206	160°	56°	19	6	↑F ↓F		T
16	218	40°	57°	14	26	↑F ↓F	0,4	T
17	233	190°	80°	10	0	↑R ↓F		T
18	244	210°	62°	16	1	↑F ↓F	0,4	T
19	246	170°	40°	40	9	↑R ↓F	0,7	T

SCAN LINES FROM THE PAVEMENT OF THE QUARRY

Measure	**Distance from zero (cm)**	**Measure**	**Distance from zero (cm)**	**Measure**	**Distance from zero (cm)**
1	6	1	2,5	1	10
2	8,5	2	4	2	12
3	13	3	9,5	3	15
4	14	4	10,5	4	16
5	15	5	11,5	5	22
6	17	6	17	6	25
7	19	7	22,5	7	30
8	22	8	23,4	8	40
9	27	9	26,8	9	45
10	32	10	34		
11	38	11	38		

12	43,5	12	44
13	48	13	48
14	54	14	49
15	59	15	53
16	60	16	73
17	65,5	17	85
18	68	18	88
19	71	19	94
20	78	20	99
21	82	21	103
		22	108
		23	109
		24	118,5
		25	125

Measure	**Distance from zero (cm)**	**Measure**	**Distance from zero (cm)**	**Measure**	**Distance from zero (cm)**
1	6,5	1	8	1	17
2	15	2	12	2	26
3	24	3	20	3	31
4	33	4	25,5	4	34
5	39	5	28,5	5	43
6	40	6	31	6	52
7	41	7	39	7	54

8	42
9	43
10	48,5
11	51
12	55

8	46
9	47
10	51
11	54
12	70
13	79
14	80
15	89,5
16	96
17	98
18	107

8	56,5
9	65
10	73
11	76
12	84

Measure	**Distance from zero (cm)**
1	3
2	10
3	13
4	13,2
5	18
6	21
7	22,5
8	27

Measure	**Distance from zero (cm)**
1	1
2	5
3	6
4	13
5	20
6	22
7	29
8	32

Measure	**Distance from zero (cm)**
1	13
2	30
3	40
4	42
5	45
6	48
7	60
8	79

9	28	9	38	9	89
10	46	10	46,5	10	100
11	51	11	54	11	107
12	65	12	60	12	114
13	69	13	69	13	122
14	72	14	72	14	134
15	74	15	78	15	136
16	77	16	81		
17	81	17	84		
18	84	18	87		
19	85	19	88		
20	88	20	93		
21	91	21	94		
22	94	22	105		
23	95,5	23	111		
24	97	24	128		
25	98	25	132		
26	100	26	137		
27	101	27	144		
28	108	28	148		
29	110	29	157		
30	116	30	166		
31	119	31	168		
32	120	32	173		

Table 9. PFLOTRAN CARD 1—Steady state conditions

```
#========================== flow mode =========================================


SIMULATION
  SIMULATION_TYPE SUBSURFACE
  PROCESS_MODELS
    SUBSURFACE_FLOW flow
      MODE GENERAL
      OPTIONS
        ISOTHERMAL
        TWO_PHASE_ENERGY_DOF TEMPERATURE
        GAS_COMPONENT_FORMULA_WEIGHT 44.0095D0
        MAXIMUM_PRESSURE_CHANGE 5.0D5
        ITOL_SCALED_RESIDUAL 1.d-5
        MAX_ITERATION_BEFORE_DAMPING 20
      /
    /
  /
  CHECKPOINT
     PERIODIC TIMESTEP 2 d
     TIMES d  6. 8. 10. 12. 14. 16. 18. 20.
  /
END


SUBSURFACE
```

```
#=============================== discretization ==========================================
GRID
  TYPE STRUCTURED
  NXYZ 59 19 9
  BOUNDS
    0.d0 0.d0 0.d0
    30.d0 10.d0 5.d0
  /
END

#================================ solver options ==========================================
NEWTON_SOLVER FLOW

/

LINEAR_SOLVER FLOW  !default convergence criteria by PFLOTRAN
/

#================================ data sets ================================================
DATASET perm_fieldX
  FILENAME ./props.h5
  HDF5_DATASET_NAME PermeabilityX
/

DATASET perm_fieldY
  FILENAME ./props.h5
  HDF5_DATASET_NAME PermeabilityY
/

DATASET perm_fieldZ
```

```
  FILENAME ./props.h5
  HDF5_DATASET_NAME PermeabilityZ
/

DATASET porosity
  FILENAME ./props.h5
  HDF5_DATASET_NAME Porosity
/

#===================== fluid properties ===========================
FLUID_PROPERTY
  PHASE LIQUID
  DIFFUSION_COEFFICIENT 0.d-0
END

FLUID_PROPERTY
  PHASE GAS
  DIFFUSION_COEFFICIENT 0.d-0
END

EOS WATER
  DENSITY EXPONENTIAL 996.629 101320.d0 4.45d-10
  VISCOSITY CONSTANT 8.5077d-4
  ENTHALPY CONSTANT 1.8890d6
/

EOS GAS
  VISCOSITY CONSTANT 16.1d-6
/
#====================== material properties =========================
```

```
MATERIAL_PROPERTY soil
 ID 1
 CHARACTERISTIC_CURVES SF1
 POROSITY DATASET porosity
 TORTUOSITY 1.
 ROCK_DENSITY 2650.d0
 THERMAL_CONDUCTIVITY_DRY 0.5
 THERMAL_CONDUCTIVITY_WET 2.
 HEAT_CAPACITY 830.
 SOIL_COMPRESSIBILITY_FUNCTION BRAGFLO
 BULK_COMPRESSIBILITY 1.d-8
 SOIL_REFERENCE_PRESSURE 101320.d0
 PERMEABILITY
   ANISOTROPIC
   DATASET perm_field
 /
END

#========================= saturation functions ============================
CHARACTERISTIC_CURVES SF1
 SATURATION_FUNCTION BROOKS_COREY
         SMOOTH
   LAMBDA 1.0121D0
   ALPHA  1.142D-6
   LIQUID_RESIDUAL_SATURATION 0.088D0
   MAX_CAPILLARY_PRESSURE 1.D8
 /
 PERMEABILITY_FUNCTION BURDINE
   LAMBDA 1.0121D0
   LIQUID_RESIDUAL_SATURATION 0.088D0
```

```
 /
  PERMEABILITY_FUNCTION BURDINE_BC_GAS
    LAMBDA 1.0121D0
    LIQUID_RESIDUAL_SATURATION 0.088D0
    GAS_RESIDUAL_SATURATION    1.D-5
 /
END

#========================== output options ===================================
OUTPUT
  TIMES d 1.e-6 1.e-5 1.e-4 1.e-3 1.e-2 1.e-1 0.5 1. 2. 3. 4. 5. 6. 7. 8. 9. 10. 12. 14. 16. 18. 19. 19.25
19.5 19.75 20. \
  20.25 20.5 20.75 21. 22. 24. 26. 28. 30. 35. 40. 45. 50.

  FORMAT HDF5
  VARIABLES
    TEMPERATURE
    LIQUID_PRESSURE
    GAS_PRESSURE
    AIR_PRESSURE
    GAS_SATURATION
    LIQUID_MOLE_FRACTIONS
    GAS_MOLE_FRACTIONS
    LIQUID_ENERGY PER_VOLUME
    GAS_ENERGY PER_VOLUME
    GAS_DENSITY
  /

#========================== times ============================================
TIME
```

```
  FINAL_TIME 50.d0 d
  INITIAL_TIMESTEP_SIZE 1.d-2 d
  MAXIMUM_TIMESTEP_SIZE 1.d0 d
/
#======================== regions ========================================
REGION all
  COORDINATES
    0.d0 0.d0 0.d0
    30.d0 10.d0 5.d0
  /
END

REGION top
  FACE TOP
  COORDINATES
    0.d0 0.d0 5.d0
    30.d0 10.d0 5.d0
  /
END

REGION bottom
  FACE BOTTOM
  COORDINATES
    0.d0 0.d0 0.d0
    30.d0 10.d0 0.d0
  /
END

REGION east
  FACE EAST
```

```
  COORDINATES
    30.d0 0.d0 0.d0
    30.d0 10.d0 5.d0
  /
END

REGION west
  FACE WEST
  COORDINATES
    0.d0 0.d0 0.d0
    0.d0 10.d0 5.d0
  /
END

REGION north
  FACE NORTH
  COORDINATES
    0.d0 10.d0 0.d0
    30.d0 10.d0 5.d0
  /
END

REGION south
  FACE SOUTH
  COORDINATES
    0.d0 0.d0 0.d0
    30.d0 0.d0 5.d0
  /
END
```

```
#=========================== flow conditions ==================================
FLOW_CONDITION 1
  TYPE
    GAS_PRESSURE dirichlet
    LIQUID_SATURATION dirichlet
    TEMPERATURE dirichlet
  /
  GAS_PRESSURE 1.01325e+05
  LIQUID_SATURATION 9.999900e-01
  TEMPERATURE 25.d0
END

FLOW_CONDITION atmosphere
   TYPE
    GAS_PRESSURE dirichlet
    LIQUID_SATURATION dirichlet
    TEMPERATURE dirichlet
  /
  GAS_PRESSURE 1.01325e+05
  LIQUID_SATURATION 9.999900e-01
  TEMPERATURE 25.d0
END

FLOW_CONDITION bottom
   TYPE
    GAS_PRESSURE dirichlet
    LIQUID_SATURATION dirichlet
    TEMPERATURE dirichlet
   /
   GAS_PRESSURE 1.53905e+05
```

```
   LIQUID_SATURATION 9.999900e-01
   TEMPERATURE 25.d0
END
#=========================== condition couplers ==============================
INITIAL_CONDITION
  FLOW_CONDITION 1
  REGION all
END

BOUNDARY_CONDITION
  FLOW_CONDITION atmosphere
  REGION top
END

BOUNDARY_CONDITION
  FLOW_CONDITION bottom
  REGION bottom
END
#=========================== stratigraphy couplers ===========================
STRATA
  MATERIAL soil
  REGION all
/
END_SUBSURFACE
```

Table 10. PFLOTRAN CARD 2 – CO$_2$ injection

```
#========================== flow mode ========================================


SIMULATION
 SIMULATION_TYPE SUBSURFACE
 PROCESS_MODELS
  SUBSURFACE_FLOW flow
   MODE GENERAL
   OPTIONS
    ISOTHERMAL
    TWO_PHASE_ENERGY_DOF TEMPERATURE
    GAS_COMPONENT_FORMULA_WEIGHT 44.0095D0
    MAXIMUM_PRESSURE_CHANGE 5.0D5
    ITOL_SCALED_RESIDUAL 1.d-5
    MAX_ITERATION_BEFORE_DAMPING 20



   /
  /
 /

 RESTART restart.chk 0.d0

 /
END
SUBSURFACE



#========================== discretization ===================================
GRID
```

```
  TYPE STRUCTURED
  NXYZ 59 19 9
  BOUNDS
    0.d0 0.d0 0.d0
    30.d0 10.d0 5.d0
  /
END

#=========================== solver options ===================================
NEWTON_SOLVER FLOW
/

LINEAR_SOLVER FLOW
/

#=========================== data sets ========================================
DATASET perm_fieldX
  FILENAME ./props.h5
  HDF5_DATASET_NAME PermeabilityX
/

DATASET perm_fieldY
  FILENAME ./props.h5
  HDF5_DATASET_NAME PermeabilityY
/

DATASET perm_fieldZ
  FILENAME ./props.h5
  HDF5_DATASET_NAME PermeabilityZ
/
```

```
DATASET porosity
  FILENAME ./props.h5
  HDF5_DATASET_NAME Porosity
/

#======================== fluid properties ================================
FLUID_PROPERTY
  PHASE LIQUID
  DIFFUSION_COEFFICIENT 0.d-0
END

FLUID_PROPERTY
  PHASE GAS
  DIFFUSION_COEFFICIENT 0.d-0
END

EOS WATER
  DENSITY EXPONENTIAL 996.629 101320.d0 4.45d-10
  VISCOSITY CONSTANT 8.5077d-4
  ENTHALPY CONSTANT 1.8890d6
/

EOS GAS
  VISCOSITY CONSTANT 16.1d-6
/
#========================== material properties =============================
MATERIAL_PROPERTY soil
  ID 1
  CHARACTERISTIC_CURVES SF1
```

```
  POROSITY DATASET porosity
  TORTUOSITY 1.
  ROCK_DENSITY 2650.d0
  THERMAL_CONDUCTIVITY_DRY 0.5
  THERMAL_CONDUCTIVITY_WET 2.
  HEAT_CAPACITY 830.
  SOIL_COMPRESSIBILITY_FUNCTION BRAGFLO
  BULK_COMPRESSIBILITY 1.d-8
  SOIL_REFERENCE_PRESSURE 101320.d0
  PERMEABILITY
    ANISOTROPIC
    DATASET perm_field
  /
END

#========================= saturation functions ============================

CHARACTERISTIC_CURVES SF1
  SATURATION_FUNCTION BROOKS_COREY
	SMOOTH
    LAMBDA 1.0121D0
    ALPHA  1.142D-6
    LIQUID_RESIDUAL_SATURATION 0.088D0
    MAX_CAPILLARY_PRESSURE 1.D8
  /
  PERMEABILITY_FUNCTION BURDINE
    LAMBDA 1.0121D0
    LIQUID_RESIDUAL_SATURATION 0.088D0
  /
  PERMEABILITY_FUNCTION BURDINE_BC_GAS
```

```
    LAMBDA 1.0121D0
    LIQUID_RESIDUAL_SATURATION 0.088D0
    GAS_RESIDUAL_SATURATION    1.D-5
  /
  TEST
/

#========================= output options ==================================
OUTPUT
  TIMES d 1.e-6 1.e-5 1.e-4 1.e-3 1.e-2 1.e-1 0.5 1. 2. 3. 4. 5. 6. 7. 8. 9. 10.

  FORMAT HDF5
  PERIODIC_OBSERVATION TIMESTEP 1
  VARIABLES
    TEMPERATURE
    LIQUID_PRESSURE
    GAS_PRESSURE
    AIR_PRESSURE
    GAS_SATURATION
    LIQUID_MOLE_FRACTIONS
    GAS_MOLE_FRACTIONS
    LIQUID_SATURATION
    GAS_ENERGY PER_VOLUME
    GAS_DENSITY

   /
/
#========================= times ==========================================
TIME
  FINAL_TIME 10. d
```

```
  INITIAL_TIMESTEP_SIZE 1.d-2 d
  MAXIMUM_TIMESTEP_SIZE 1.d0 d
/

#========================= regions ==========================================
REGION all
  COORDINATES
    0.d0 0.d0 0.d0
    30.d0 10.d0 5.d0
  /
END

REGION top
  FACE TOP
  COORDINATES
    0.d0 0.d0 5.d0
    30.d0 10.d0 5.d0
  /
END

REGION bottom
  FACE BOTTOM
  COORDINATES
    0.d0 0.d0 0.d0
    30.d0 10.d0 0.d0
  /
END

REGION east
  FACE EAST
```

```
  COORDINATES
    30.d0 0.d0 0.d0
    30.d0 10.d0 5.d0
  /
END

REGION west
  FACE WEST
  COORDINATES
    0.d0 0.d0 0.d0
    0.d0 10.d0 5.d0
  /
END

REGION north
  FACE NORTH
  COORDINATES
    0.d0 10.d0 0.d0
    30.d0 10.d0 5.d0
  /
END

REGION south
  FACE SOUTH
  COORDINATES
    0.d0 0.d0 0.d0
    30.d0 0.d0 5.d0
  /
END
```

```
REGION well
  COORDINATES
        8.d0 5.d0 2.d0
        8.d0 5.d0 2.d0
  /
END

REGION obs1
  COORDINATES
        7.5d0 5.d0 3.5d0
        7.5d0 5.d0 3.5d0
  /
END

#=========================== observation points =============================
OBSERVATION obs1
  REGION obs1
  AT_CELL_CENTER
  VELOCITY
END

#=========================== flow conditions ================================
FLOW_CONDITION 1
  TYPE
    GAS_PRESSURE dirichlet
    LIQUID_SATURATION dirichlet
    TEMPERATURE dirichlet
  /
  GAS_PRESSURE 1.01325e+05
  LIQUID_SATURATION 9.999900e-01
```

```
  TEMPERATURE 25.d0  FIE
END

FLOW_CONDITION well
  TYPE
    RATE mass_rate
  /
  RATE 0.d0 6.d-4 0.d0  kg/s kg/s MW    # CO2 injection rate test 2=6.d-5
/

#=========================== condition couplers ===============================
INITIAL_CONDITION
  FLOW_CONDITION 1
  REGION all
END

SOURCE_SINK well
 FLOW_CONDITION well
  REGION well
/

#=========================== stratigraphy couplers ============================
STRATA
  MATERIAL soil
  REGION all
/
END_SUBSURFACE
```

Bibliography

Agosta, F., 2008. Fluid flow properties of basin-bounding normal faults in platform carbonates, Fucino Basin, central Italy. Geol. Soc. London, Spec. Publ. 299, 277 LP-291.

Agosta, F., Alessandroni, M., Antonellini, M., Tondi, E., Giorgioni, M., 2010. From fractures to flow: A field-based quantitative analysis of an outcropping carbonate reservoir. Tectonophysics 490, 197–213. https://doi.org/10.1016/J.TECTO.2010.05.005

Agosta, F., Alessandroni, M., Tondi, E., Aydin, A., 2010. Oblique normal faulting along the northern edge of the Majella Anticline, central Italy: Inferences on hydrocarbon migration and accumulation. J. Struct. Geol. 32, 1317–1333. https://doi.org/10.1016/j.jsg.2010.10.007

Andersson, J., and B.D., 1987. Conditional simulations of fluid flow in three-dimensional networks of discrete fractures. Water Resour. Res. 23(10), 1876–1886.

Andersson, J., Shapiro, A.M., Bear, J., 1984. A Stochastic Model of a Fractured Rock Conditioned by Measured Information. Water Resour. Res. 20, 79–88. https://doi.org/10.1029/WR020i001p00079

Annunziatellis, A., Beaubien, S.E., Bigi, S., Ciotoli, G., Coltella, M., Lombardi, S., 2008a. Gas migration along fault systems and through the vadose zone in the Latera caldera (central Italy): Implications for CO2 geological storage. Int. J. Greenh. Gas Control 2, 353–372. https://doi.org/10.1016/J.IJGGC.2008.02.003

Annunziatellis, A., Beaubien, S.E., Bigi, S., Ciotoli, G., Coltella, M., Lombardi, S., 2008b. Gas migration along fault systems and through the vadose zone in the Latera caldera (central Italy): Implications for CO2 geological storage. Int. J. Greenh. Gas Control 2, 353–372. https://doi.org/10.1016/J.IJGGC.2008.02.003

Antonellini, M., Aydin, A., 1994. Effect of faulting on fluid flow in porous sandstones: Petrophysical properties. Aapg Bull. - AAPG BULL 78, 355–377.

Antonellini, M., Petracchini, L., Billi, A., Scrocca, D., 2014. First reported occurrence of deformation bands in a platform limestone, the Jurassic Calcare Massiccio Fm., northern Apennines, Italy. Tectonophysics 628, 85–104. https://doi.org/10.1016/J.TECTO.2014.04.034

Aydin, A., 2000. Fractures, faults, and hydrocarbon entrapment, migration and flow. Mar. Pet. Geol. 17, 797–814.

Aydin, A., Borja, R.I., Eichhubl, P., 2006. Geological and mathematical framework for failure modes in granular rock. J. Struct. Geol. 28, 83–98. https://doi.org/10.1016/J.JSG.2005.07.008

Aydin, A., Schultz, R.A., 1990. Effect of mechanical interaction on the development of strike-slip faults with echelon patterns. J. Struct. Geol. 12, 123–129. https://doi.org/10.1016/0191-8141(90)90053-2

Bai, H., Montési, L.G.J., Behn, M.D., 2017. MeltMigrator: A MATLAB-based software for modeling three-dimensional melt migration and crustal thickness variations at mid-ocean ridges following a rules-based approach. Geochemistry, Geophys. Geosystems 18, 445–456. https://doi.org/10.1002/2016GC006686

Barenblatt, G.I., Zheltov, I.P., and Kochina, I.., 1960. Basic concepts inthe theory of seepage of homogeneous liquids in fissured rocks. J. Appl.Math. Mech 24, 1286–1303.

Barth, G.A., Mutter, J.C., 1996. Variability in oceanic crustal thickness and structure: Multichannel seismic reflection results from the northern East Pacific Rise. J. Geophys. Res. Solid Earth 101, 17951–17975. https://doi.org/10.1029/96JB00814

Bastesen, E., Braathen, A., 2010. Extensional faults in fine grained carbonates – analysis of fault core lithology and thickness–displacement relationships. J. Struct. Geol. 32, 1609–1628. https://doi.org/10.1016/j.jsg.2010.09.008

Batiza, R., Niu, Y., 1992. Petrology and magma chamber processes at the East Pacific Rise ∼ 9°30′N. J. Geophys. Res. 97, 6779. https://doi.org/10.1029/92JB00172

Batiza, R., Vanko, D., 1984. Petrology of Young Pacific Seamounts. J. Geophys. Res. Solid Earth 89, 11235–11260. https://doi.org/10.1029/JB089iB13p11235

Berg, S.S., Skar, T., 2005. Controls on damage zone asymmetry of a normal fault zone: outcrop analyses of a segment of the Moab fault, SE Utah. J. Struct. Geol. 27, 1803–1822. https://doi.org/10.1016/j.jsg.2005.04.012

Berkowitz, B., Balberg, I., 1993. Percolation theory and its application to groundwater hydrology. Water Resour. Res. 29, 775–794. https://doi.org/10.1029/92WR02707

Bigi, S., Battaglia, M., Alemanni, A., Lombardi, S., Campana, A., Borisova, E., Loizzo, M., 2013. CO2 flow through a fractured rock volume: Insights from field data, 3D fractures representation and fluid flow modeling. Int. J. Greenh. Gas Control 18, 183–199. https://doi.org/10.1016/J.IJGGC.2013.07.011

Billi, A., Salvini, F., Storti, F., 2003. The damage zone-fault core transition in carbonate rocks: implications for fault growth, structure and permeability. J. Struct. Geol. 25, 1779–1794. https://doi.org/10.1016/S0191-8141(03)00037-3

Brown, S.R., Bruhn, R.L., 1998. Fluid permeability of deformable fracture networks. J. Geophys. Res. Solid Earth 103, 2489–2500. https://doi.org/10.1029/97JB03113

Bruhn, R.L., Parry, W.T., Yonkee, W.A., Thompson, T., 1994. Fracturing and hydrothermal alteration in normal fault zones. pure Appl. Geophys. 142, 609–644. https://doi.org/10.1007/BF00876057

Cacas, M. C., E. Ledoux, G. de Marsily, A. Barbreau, P. Calmels, B. Gaillard, and R.M., 1990. Modeling fracture flow with a stochastic discrete fracture network: Calibration and validation: 2, The transport model. Water Resour. Res. 26, 491–500.

Caine, J., Evans, J., B. Forster, C., 1996. Fault zone architecture and permeability structure. Geology 24, 1025–1028.

Cappa, F., Rutqvist, J., 2011. Impact of CO $_2$ geological sequestration on the nucleation of earthquakes. Geophys. Res. Lett. 38, n/a-n/a. https://doi.org/10.1029/2011GL048487

Carbotte, S., Macdonald, K., 1992. East Pacific Rise 8°–10°30′N: Evolution of ridge segments and discontinuities from SeaMARC II and three-dimensional magnetic studies. J. Geophys. Res. 97, 6959. https://doi.org/10.1029/91jb03065

Carbotte, S.M., Smith, D.K., Cannat, M., Klein, E.M., 2016. Tectonic and magmatic segmentation of the Global Ocean Ridge System: a synthesis of observations. Geol. Soc. London, Spec. Publ. 420, 249–295. https://doi.org/10.1144/SP420.5

Casabianca, D., Bosence, D., Beckett, D., 2002. Reservoir potential of cretaceous platform-margin breccias, central italian apennines. J. Pet. Geol. 25, 179–202. https://doi.org/10.1111/j.1747-5457.2002.tb00003.x

Casnedi, R., 1983. Hydrocarbon-Bearing Submarine Fan System of Cellino Formation, Central Italy. Am. Assoc. Pet. Geol. Bull. 67.

Cello, G., Tondi, E., Micarelli, L., Invernizzi, C., 2001. Fault zone fabrics and geofluid properties as indicators of rock deformation modes. J. Geodyn. 32, 543–565. https://doi.org/https://doi.org/10.1016/S0264-3707(01)00047-3

Chester, F.M., Logan, J.M., 1986. Implications for mechanical properties of brittle faults from observations of the Punchbowl fault zone, California. pure Appl. Geophys. 124, 79–106. https://doi.org/10.1007/BF00875720

Childs, C., Nicol, A., Walsh, J.J., Watterson, J., 1996. Growth of vertically segmented normal faults. J. Struct. Geol. 18, 1389–1397. https://doi.org/10.1016/S0191-8141(96)00060-0

Childs, C., Sylta, Ø., Moriya, S., Walsh, J.J., Manzocchi, T., 2002. A method for including the capillary properties of faults in hydrocarbon migration models. Nor. Pet. Soc. Spec. Publ. 11, 127–139. https://doi.org/10.1016/S0928-8937(02)80011-X

Ciotoli, G., Etiope, G., Guerra, M., Lombardi, S., Duddridge, G.A., Grainger, P., 2005. Migration of gas injected into a fault in low-permeability ground. Q. J. Eng. Geol. Hydrogeol. 38, 305–320. https://doi.org/10.1144/1470-9236/03-058

Cordery, M.J., Morgan, J.P., 1993. Convection and melting at mid-ocean ridges. J. Geophys. Res. Solid Earth 98, 19477–19503. https://doi.org/10.1029/93JB01831

Cordery, M.J., Morgan, J.P., 1992. Melting and mantle flow beneath a mid-ocean spreading center. Earth Planet. Sci. Lett. 111, 493–516. https://doi.org/10.1016/0012-821X(92)90199-6

Daines, M.J., Kohlstedt, D.L., 1997. Influence of deformation on melt topology in peridotites. J. Geophys. Res. Solid Earth 102, 10257–10271. https://doi.org/10.1029/97JB00393

Dershowitz, W., & La Pointe, P., 1994. Discrete Fracture Approaches for Oil and Gas Applications. Am. Rock Mech. Assoc.

Dershowitz, W., G. Lee, and T.F., 2004. FracWorks XP Discrete Fracture Modeling Software, User Documentation. Redmond. Redmond, WA, Golder.

Dershowitz, W.S., 1984. Rock joint systems, Ph.D. thesis, Mass. Inst. of Technol., Cambridge.

Dershowitz, W.S., Einstein, H.H., 1987. Three Dimensional Flow Modeling In Jointed Rock

Masses.

Dershowitz, W.S., Fidelibus, C., 1999. Derivation of equivalent pipe network analogues for three-dimensional discrete fracture networks by the boundary element method. Water Resour. Res. 35, 2685–2691. https://doi.org/10.1029/1999WR900118

Donzelli, G., 1969. Studio geologico della Maiella. , report, 49 pp., Univ. degli Stud. G. D’Annunzio, Chieti, Italy.

Downey, , 1984. Evaluating seals for hydrocarbon accumulation. AAPG Bull. 68.

Duguid, J.O., Lee, P.C.Y., 1977. Flow in fractured porous media. Water Resour. Res. 13, 558–566. https://doi.org/10.1029/WR013i003p00558

Endo, H.K., Long, J.C.S., Wilson, C.R., Witherspoon, P.A., 1984. A Model for Investigating Mechanical Transport in Fracture Networks. Water Resour. Res. 20, 1390–1400. https://doi.org/10.1029/WR020i010p01390

Faulkner, D.R., Mitchell, T.M., Jensen, E., Cembrano, J., 2011. Scaling of fault damage zones with displacement and the implications for fault growth processes. J. Geophys. Res. Solid Earth 116, n/a--n/a. https://doi.org/10.1029/2010JB007788

Fisher, Q., Knipe, R., 1998. Fault sealing processes in siliciclastic sediments. Geol. Soc. London, Spec. Publ. 147, 117–134.

Fletcher, R.C., Pollard, D.D., 1981. Anticrack model for pressure solution surfaces. Geology 9, 419–424.

Fornari, D.J., Gallo, D.G., Edwards, M.H., Madsen, J.A., Perfit, M.R., Shor, A.N., 1989. Structure and topography of the Siqueiros transform fault system: Evidence for the development of intra-transform spreading centers. Mar. Geophys. Res. 11, 263–299. https://doi.org/10.1007/BF00282579

Fornari, D.J., Perfit, M.R., Allan, J.F., Batiza, R., 1988a. Small-scale heterogeneities in depleted mantle sources: near-ridge seamount lava geochemistry and implications for mid-ocean-ridge magmatic processes. Nature 331, 511–513. https://doi.org/10.1038/331511a0

Fornari, D.J., Perfit, M.R., Allan, J.F., Batiza, R., Haymon, R., Barone, A., Ryan, W.B.F., Smith, T., Simkin, T., Luckman, M.A., 1988b. Geochemical and structural studies of the

Lamont seamounts: seamounts as indicators of mantle processes. Earth Planet. Sci. Lett. 89, 63–83. https://doi.org/10.1016/0012-821X(88)90033-7

Forsyth, D.W., W., D., 2013. Geophysical Constraints on Mantle Flow and Melt Generation Beneath Mid-Ocean Ridges, in: Mantle Flow and Melt Generation at Mid-Ocean Ridges. (1992), Geophys. Monogr. Ser., Vol. 71, Edited by J. P. Morgan, D. K. Blackman, and J. M. Sinton, Pp. 1-65, AGU, Washington, D. C. pp. 1–65. https://doi.org/10.1029/GM071p0001

Fox, P.J., and Gallo, D.G., 1984. A tectonic model for ridge-transform-ridge plate boundaries: Implications for the structure of oceanic lithosphere. Tectonophysics 316, 205–242.

Gale, A., Dalton, C.A., Langmuir, C.H., Su, Y., Schilling, J.-G., 2013. The mean composition of ocean ridge basalts. Geochemistry, Geophys. Geosystems 14, 489–518. https://doi.org/10.1029/2012GC004334

Ghisetti, F., Vezzani, L., 2002. Normal faulting, extension and uplift in the outer thrust belt of the central Apennines (Italy): role of the Caramanico fault. Basin Res. 14, 225–236. https://doi.org/10.1046/j.1365-2117.2002.00171.x

Gilmour, H.M.P., Billaux, D., Long, J.C.S., 1986. Models for calculating fluid flow in randomly generated three-dimensional networks of disc-shaped fractures: Theory and design of FMG3D, DISCEL, and DIMES.

Graham Wall, B.R., Girbacea, R., Mesonjesi, A., Aydin, A., 2006. Evolution of fracture and fault-controlled fluid pathways in carbonates of the Albanides fold-thrust belt. Am. Assoc. Pet. Geol. Bull. 90, 1227–1249. https://doi.org/10.1306/03280604014

Gregg, P., Hebert, L., Montési, L., Katz, R., 2012. Geodynamic Models of Melt Generation and Extraction at Mid-Ocean Ridges. Oceanography 25, 78–88. https://doi.org/10.5670/oceanog.2012.05

Gregg, P.M., Behn, M.D., Lin, J., Grove, T.L., 2009. Melt generation, crystallization, and extraction beneath segmented oceanic transform faults. J. Geophys. Res. 114. https://doi.org/10.1029/2008jb006100

Gregg, P.M., Lin, J., Behn, M.D., Montesi, L.G., 2007. Spreading rate dependence of gravity anomalies along oceanic transform faults. Nature 448, 183–187.

https://doi.org/10.1038/nature05962

Gudmundsson, A., Simmenes, T.H., Larsen, B., Philipp, S.L., 2010. Effects of internal structure and local stresses on fracture propagation, deflection, and arrest in fault zones. J. Struct. Geol. 32, 1643–1655. https://doi.org/10.1016/J.JSG.2009.08.013

Hebert, L.B., Montesi, L.G., 2010. Crustal thickness variations at oceanic ridge segment and transform faults: implications for three-dimensional melt extraction pathways. Am. Geophys. Union, Fall Meet. 2010, Abstr. #OS24A-04.

Hebert, L.B., Montési, L.G.J., 2011. Melt extraction pathways at segmented oceanic ridges: Application to the East Pacific Rise at the Siqueiros transform. Geophys. Res. Lett. 38, n/a-n/a. https://doi.org/10.1029/2011gl047206

Hékinian, R., Bideau, D., Hébert, R., Niu, Y., 1995. Magmatism in the Garrett transform fault (East Pacific Rise near 13°27′S). J. Geophys. Res. Solid Earth 100, 10163–10185. https://doi.org/10.1029/94JB02125

Herbert E. Huppert, 1986. The intrusion of fluid mechanics into geology. J. Fluid Mech 173, 557–594.

Hudson, J.A., La Pointe, P.R., 1980. Printed circuits for studying rock mass permeability. Int. J. Rock Mech. Min. Sci. Geomech. Abstr. 17, 297–301. https://doi.org/10.1016/0148-9062(80)90812-8

Hudson, J. (John A.., Harrison, J.P., 2005. Engineering rock mechanics : an introduction to the principles. Pergamon.

Hyman, J., Karra, S., Makedonska, N., Gable, C., L. Painter, S., Viswanathan, H., 2015. DFNWORKS: A discrete fracture network framework for modeling subsurface flow and transport. Comput. Geosci. 84, 10–19.

Hyman, J.D., Gable, C.W., Painter, S.L., Makedonska, N., 2014. Conforming Delaunay Triangulation of Stochastically Generated Three Dimensional Discrete Fracture Networks: A Feature Rejection Algorithm for Meshing Strategy. SIAM J. Sci. Comput. 36, A1871–A1894. https://doi.org/10.1137/130942541

IEAGHG. Fault Permeability Study. IEAGHG report 2016, n.d.

Jackson, C.P., Hoch, A.R., Todman, S., 2000. Self-consistency of a heterogeneous continuum porous medium representation of a fractured medium. Water Resour. Res. 36, 189–202. https://doi.org/10.1029/1999WR900249

Jeanne, P., Guglielmi, Y., Cappa, F., Rinaldi, A.P., Rutqvist, J., 2014. The effects of lateral property variations on fault-zone reactivation by fluid pressurization: Application to CO2 pressurization effects within major and undetected fault zones. J. Struct. Geol. 62, 97–108. https://doi.org/10.1016/J.JSG.2014.01.017

Jha, B., Juanes, R., 2014. Coupled multiphase flow and poromechanics: A computational model of pore pressure effects on fault slip and earthquake triggering. Water Resour. Res. 50, 3776–3808. https://doi.org/10.1002/2013WR015175

Jourde, H., Flodin, E.A., Aydin, A., Durlofsky, L.J., Wen, X.H., 2002. Computing permeability of fault zones in eolian sandstone from outcrop measurements. Am. Assoc. Pet. Geol. Bull. 86, 1187–1200. https://doi.org/10.1306/61EEDC4C-173E-11D7-8645000102C1865D

Katz, Richard F, S.M.& H.B., 2006. The dynamics of melt and shear localization in partially molten aggregates. Nature 442, 676–679.

Katz, R.F., 2010. Porosity-driven convection and asymmetry beneath mid-ocean ridges. Geochemistry, Geophys. Geosystems 11, n/a-n/a. https://doi.org/10.1029/2010GC003282

Keating, E., Newell, D., Stewart, B., Capo, R., Pawar, R., 2014. Further Insights Into Interconnections between the Shallow and Deep Systems from a Natural CO2 Reservoir Near Springerville, Arizona, U.S.A. Energy Procedia 63, 3195–3201. https://doi.org/10.1016/J.EGYPRO.2014.11.344

Kent, G.M., Harding, A.J., Orcutt, J.A., 1993. Distribution of magma beneath the East Pacific Rise between the Clipperton Transform and the 9°17′N Deval from forward modeling of common depth point data. J. Geophys. Res. Solid Earth 98, 13945–13969. https://doi.org/10.1029/93JB00705

Kim, Y.-S., Sanderson, D.J., 2010. Inferred fluid flow through fault damage zones based on the observation of stalactites in carbonate caves. J. Struct. Geol. 32, 1305–1316. https://doi.org/10.1016/J.JSG.2009.04.017

Kinzler, R.J., Grove, T.L., 1992a. Primary magmas of mid-ocean ridge basalts 1.

Experiments and methods. J. Geophys. Res. 97, 6885. https://doi.org/10.1029/91JB02840

Kinzler, R.J., Grove, T.L., 1992b. Primary magmas of mid-ocean ridge basalts 2. Applications. J. Geophys. Res. 97, 6907. https://doi.org/10.1029/91JB02841

Klein, E.M., Langmuir, C.H., 1987. Global correlations of ocean ridge basalt chemistry with axial depth and crustal thickness. J. Geophys. Res. 92, 8089. https://doi.org/10.1029/JB092iB08p08089

Klitgord, K.D., Mammerickx, J., 1982. Northern East Pacific Rise: Magnetic anomaly and bathymetric framework. J. Geophys. Res. Solid Earth 87, 6725–6750. https://doi.org/10.1029/JB087iB08p06725

Knipe, R.J., Jones, G., Fisher, Q.J., 1998. Faulting, fault sealing and fluid flow in hydrocarbon reservoirs: an introduction. Geol. Soc. London, Spec. Publ. 147, vii LP-xxi.

Koudina, N., R. Gonzalez Garcia, J.-F. Thovert, and P.M.A., 1998. Permeability of three-dimensional fracture networks. Phys. Rev. E 57, 4466 – 4479.

Lampert, S.A., Lowrie, W., Hirt, A.M., Bernoulli ’, D., Mutti, M., 1997. Magnetic and sequence stratigraphy of redeposited Upper Cretaceous limestones in the Montagna della Maiella, Abruzzi, Italy. Earth Planet. Sci. Lett. 150, 79–93.

Lei, X., Huang, D., Su, J., Jiang, G., Wang, X., Wang, H., Guo, X., Fu, H., 2017. Fault reactivation and earthquakes with magnitudes of up to Mw4.7 induced by shale-gas hydraulic fracturing in Sichuan Basin, China. Sci. Rep. 7, 7971. https://doi.org/10.1038/s41598-017-08557-y

Lichtner, P., G. Hammond, C. Lu, S. Karra, G. Bisht, B. Andre, R. Mills, and J.K., 2015. PFLOTRAN user manual: A massively parallel reactive flow and transport model for describing surface and subsurface processes. Tech. Rep. LA-UR-15-20403, Los Alamos Natl. Lab., Los Alamos, N. M.

Long, J. C. S., J. S. Remer, C. R. Wilson, and P.A.W., 1982. Porous media equivalents for networks of discontinuous fractures 18, 645–658.

Lu, J., Cook, P.J., Hosseini, S.A., Yang, C., Romanak, K.D., Zhang, T., Freifeld, B.M., Smyth, R.C., Zeng, H., Hovorka, S.D., 2012. Complex fluid flow revealed by monitoring CO $_2$ injection in a fluvial formation. J. Geophys. Res. Solid Earth 117. https://doi.org/10.1029/2011JB008939

Lunn, R.J., Shipton, Z.K., Bright, A.M., 2008. How can we improve estimates of bulk fault zone hydraulic properties? Geol. Soc. London, Spec. Publ. 299, 231–237. https://doi.org/10.1144/SP299.14

Luther, G., Gartman, A., Yücel, M., Madison, A., Moore, T., Nees, H., Nuzzio, D., Sen, A., Lutz, R., Shank, T., Fisher, C., 2012. Chemistry, Temperature, and Faunal Distributions at Diffuse-Flow Hydrothermal Vents: Comparison of Two Geologically Distinct Ridge Systems. Oceanography 25, 234–245. https://doi.org/10.5670/oceanog.2012.22

Macdonald, K.C., Fox, P.J., Miller, S., Carbotte, S., Edwards, M.H., Eisen, M., Fornari, D.J., Perram, L., Pockalny, R., Scheirer, D., Tighe, S., Weiland, C., Wilson, D., 1992. The East Pacific Rise and its flanks 8--18{\textdegree} N: History of segmentation, propagation and spreading direction based on SeaMARC II and Sea Beam studies. Mar. Geophys. Res. 14, 299–344. https://doi.org/10.1007/BF01203621

Madsen, J.A., Detrick, R.S., Mutter, J.C., Buhl, P., Orcutt, J.A., 1990. A two- and three-dimensional analysis of gravity anomalies associated with the East Pacific Rise at 9°N and 13°N. J. Geophys. Res. Solid Earth 95, 4967–4987. https://doi.org/10.1029/JB095iB04p04967

Magde, L.S., and D.W.S., 1997. Magde, L.S., and D.W. Sparks. 1997. Three-dimensional mantle upwelling, melt generation, and melt migration beneath segment slow spreading ridges. J. Geophys. Res. 102, 20571–20583.

Magde, L.S., Sparks, D.W., Detrick, R.S., 1997. The relationship between buoyant mantle flow, melt migration, and gravity bull’s eyes at the Mid-Atlantic Ridge between 33°N and 35°N. Earth Planet. Sci. Lett. 148, 59–67. https://doi.org/10.1016/S0012-821X(97)00039-3

Manzocchi, T., Childs, C., J. WALSH, J., 2010. Faults and Fault Properties in Hydrocarbon Flow Models. Geofluids 10, 94–113.

Marchegiani, L., Van Dijk, J.P., Gillespie, P.A., Tondi, E., Cello, G., 2006. Scaling properties of the dimensional and spatial characteristics of fault and fracture systems in the Majella Mountain, central Italy. Geol. Soc. London, Spec. Publ. 261, 113 LP-131.

Maryška, J., Vohralík, M., Severýn, O., Císařová, K., 2004. modelling of groundwater flow in fractured rock: theoretical approach and practical applications.

Matthäi, S.K., Belayneh, M., 2004. Fluid flow partitioning between fractures and a permeable rock matrix. Geophys. Res. Lett. 31, n/a-n/a. https://doi.org/10.1029/2003GL019027

McGrath, A.G., Davison, I., 1995. Damage zone geometry around fault tips. J. Struct. Geol. 17, 1011–1024. https://doi.org/10.1016/0191-8141(94)00116-H

Mckenzie, D., n.d. The Generation and Compaction of Partially Molten Rock.

Menard, H.W., 1967. Extension of Northeastern-Pacific Fracture Zones. Science (80-.). 155, 72 LP-74.

Menard, H.W., Fisher, R.L., 1958. Clipperton Fracture Zone in the Northeastern Equatorial Pacific. J. Geol. 66, 239–253. https://doi.org/10.1086/626502

Metz, B., Davidson, O., Coninck, H. de, Loos, M., (eds.), L.M., 2005. IPCC special report on carbon dioxide capture and storage.

Miller, S. A., C. Collettini, L. Chiaraluce, M. Cocco, M. Barchi, and B.J.P.K., 2004. Aftershocks driven by a high-pressure CO2 source at depth. Nature 427.

Montési, L.G.J., Behn, M.D., 2007. Mantle flow and melting underneath oblique and ultraslow mid-ocean ridges. Geophys. Res. Lett. 34, L24307. https://doi.org/10.1029/2007GL031067

Moore, T.S., Shank, T.M., Nuzzio, D.B., Luther, G.W., 2009. Time-series chemical and temperature habitat characterization of diffuse flow hydrothermal sites at 9°50′N East Pacific Rise. Deep Sea Res. Part II Top. Stud. Oceanogr. 56, 1616–1621. https://doi.org/10.1016/j.dsr2.2009.05.008

Morgan, J.P., Forsyth, D.W., 1988. Three-dimensional flow and temperature perturbations due to a transform offset: Effects on oceanic crustal and upper mantle structure. J. Geophys. Res. 93, 2955. https://doi.org/10.1029/JB093iB04p02955

Mustapha, H., Mustapha, K., 2007. A New Approach to Simulating Flow in Discrete Fracture Networks with an Optimized Mesh. SIAM J. Sci. Comput. 29, 1439–1459. https://doi.org/10.1137/060653482

Nagle, A. N., R. C. Pickle, A. E. Saal, E. H. Hauri, and D.W.F., 2007. Volatiles in basalts from intra-transform spreading centers: Implications for melt migration models. Eos Trans. AGU Fall Meet. Suppl., Abstr. DI43A-05 88(52).

Nelson, R.A., 2001. Geologic analysis of naturally fractured reservoirs. Gulf Professional Pub.

Neuman, S.P., 2005. Trends, prospects and challenges in quantifying flow and transport through fractured rocks. Hydrogeol. J. 13, 124–147. https://doi.org/10.1007/s10040-004-0397-2

Nicol, A., Seebeck, H., Field, B., McNamara, D., Childs, C., Craig, J., Rolland, A., 2017. Fault Permeability and CO2 Storage. Energy Procedia 114, 3229–3236. https://doi.org/10.1016/J.EGYPRO.2017.03.1454

Niu, Y., Batiza, R., 1993. Chemical variation trends at fast and slow spreading mid-ocean ridges. J. Geophys. Res. Solid Earth 98, 7887–7902. https://doi.org/10.1029/93JB00149

Niu, Y., Batiza, R., 1991. An empirical method for calculating melt compositions produced beneath mid-ocean ridges: Application for axis and off-axis (seamounts) melting. J. Geophys. Res. Solid Earth 96, 21753–21777. https://doi.org/10.1029/91JB01933

Niu, Y., Batiza, R., 1997. Trace element evidence from seamounts for recycled oceanic crust in the Eastern Pacific mantle. Earth Planet. Sci. Lett. 148, 471–483. https://doi.org/10.1016/S0012-821X(97)00048-4

Niu, Z., Li, Q., Wei, X., Li, X., Li, X., 2017. Numerical simulation of a hidden fault at different stages of evolution in a carbon dioxide-enhanced saline water recovery site. J. Pet. Sci. Eng. 154, 367–381. https://doi.org/10.1016/J.PETROL.2017.04.039

Noir, J., E. Jacques, S. Bekri, P. M. Adler, P. Tapponier, and G.C.P.K., 1997. Fluid flow triggered migration of events in the 1989 Dobi earthquake sequence of central Afar. Geophys. Res. Lett 24, 2335 – 2338.

Oda, M., Y. Hatsuyama, and Y.O., 1987. Numerical experiments on permeability tensor and its application to jointed granite at Stripa Mine, Sweden. J. Geophys. Res 8037–8048.

Oda, M., 1985. Permeability tensor for discontinuous rock masses. Géotechnique 35, 483–495. https://doi.org/10.1680/geot.1985.35.4.483

Odling, N. E., S. D. Harris, and R.J.K., 2004. Permeability scaling properties of fault damage zones in siliclastic rocks. J. Struct. Geol. 26, 1727 – 1747.

Orsini, P., Cantucci, B., Quattrocchi, F., 2014. ScienceDirect Large-scale numerical modelling of CO 2 injection and containment phases for an Italian near-coast reservoir using PFLOTRAN. Energy Procedia 51, 334–343. https://doi.org/10.1016/j.egypro.2014.07.040

Pablo Canales, J., Detrick, R.S., Toomey, D.R., Wilcock, W.S.D., 2003. Segment-scale variations in the crustal structure of 150–300 kyr old fast spreading oceanic crust (East Pacific Rise, 8°15′N–10°5′N) from wide-angle seismic refraction profiles. Geophys. J. Int. 152, 766–794.

Pacala, S., Socolow, R., 2004. Stabilization wedges: solving the climate problem for the next 50 years with current technologies. Science 305, 968–72. https://doi.org/10.1126/science.1100103

Painter, S., Gable, C., Makedonska, N., Hyman, J., Hsieh, T.-L. Bui, Q., Liu, H.H., Birkholzer, J., 2012. Fluid Flow Model Development for Representative Geologic Media. Los Alamos National Laboratory. Los Alamos Natl. Lab. LAUR-12-26878. FCRD-UFD-2013-000058.

Panza, E., Sessa, E., Agosta, F., Giorgioni, M., 2017. Discrete Fracture Network modelling of a hydrocarbon-bearing, oblique-slip fault zone: Inferences on fault-controlled fluid storage and migration properties of carbonate fault damage zones. Mar. Pet. Geol. 89.

Parmentier, E.M., Forsyth, D.W., 1985. Three-dimensional flow beneath a slow spreading ridge axis: A dynamic contribution to the deepening of the Median Valley toward fracture zones. J. Geophys. Res. Solid Earth 90, 678–684. https://doi.org/10.1029/JB090iB01p00678

Parsons, B., 1981. The rates of plate creation and consumption. Geophys. J. Int. 67, 437–448. https://doi.org/10.1111/j.1365-246X.1981.tb02759.x

Patacca, E., Scandone, P., Di Luzio, E., Cavinato, G.P., Parotto, M., 2008. Structural architecture of the central Apennines: Interpretation of the CROP 11 seismic profile from the Adriatic coast to the orographic divide. Tectonics 27, n/a-n/a. https://doi.org/10.1029/2005TC001917

Peacock, D., 2002. Propagation, interaction and linkage in normal fault systems. Earth-

Science Rev. 58, 121–142.

Perfit, M., Wanless, V.D., Ridley, W.I., Klein, E., Smith, M., Goss, A., Hinds, J., Kutza, S., Fornari, D., 2012. Lava Geochemistry as a Probe into Crustal Formation at the East Pacific Rise. Oceanography 25, 89–93. https://doi.org/10.5670/oceanog.2012.06

Perfit, M.R., Fornari, D.J., Ridley, W.I., Kirk, P.D., Casey, J., Kastens, K.A., Reynolds, J.R., Edwards, M., Desonie, D., Shuster, R., Paradis, S., 1996. Recent volcanism in the Siqueiros transform fault: picritic basalts and implications for MORB magma genesis. Earth Planet. Sci. Lett. 141, 91–108. https://doi.org/10.1016/0012-821X(96)00052-0

Phipps Morgan, J., Parmentier, E.M., Lin, J., 1987. Mechanisms for the origin of mid-ocean ridge axial topography: Implications for the thermal and mechanical structure of accreting plate boundaries. J. Geophys. Res. Solid Earth 92, 12823–12836. https://doi.org/10.1029/JB092iB12p12823

Pizzi, A., Falcucci, E., Gori, S., Galadini, F., Messina, P., Di Vincenzo, M., Esestime, P., Giaccio, B., Pomposo, G., Sposato, A., 2010. Active faulting in the Maiella Massif (central Apennines, Italy). GeoActa Spec. Publ. 3.

Pockalny, R.A., Fox, P.J., Fornari, D.J., Macdonald, K.C., Perfit, M.R., 1997. Tectonic reconstruction of the Clipperton and Siqueiros Fracture Zones: Evidence and consequences of plate motion change for the last 3 Myr. J. Geophys. Res. Solid Earth 102, 3167–3181. https://doi.org/10.1029/96JB03391

POLLARD, D.D., AYDIN, A., 1988. Progress in understanding jointing over the past century. GSA Bull. 100, 1181–1204.

Prince, R.A., Forsyth, D.W., 1988. Horizontal extent of anomalously thin crust near the Vema Fracture Zone from the three-dimensional analysis of gravity anomalies. J. Geophys. Res. Solid Earth 93, 8051–8063. https://doi.org/10.1029/JB093iB07p08051

Pruess, K., C. Oldenburg, and G.M., 1999. TOUGH2 user’s guide, Version 2.0. Lawrence Berkeley Lab. Rep. LBL-43134, Berkeley, Calif.

Pruess, Karsten, and Narasimhan, T.N., n.d. A practical method for modeling fluid and heat flow in fractured porous media. Soc. Pet. Eng. J. 25, 14–26.

Pruess, K., García, J., 2002. Multiphase flow dynamics during CO2 disposal into saline aquifers. Environ. Geol. 42, 282–295. https://doi.org/10.1007/s00254-001-0498-3

Ravaux, J., Zbinden, M., Voss-Foucart, M.F., Compare, P., Goffinet, G., Gaill, F., 2003. Comparative degradation rates of chitinous exoskeletons from deep-sea environments. Mar. Biol. 143, 405–412. https://doi.org/10.1007/s00227-003-1086-8

Robinson, B.A., Tester, J.W., 1984. Dispersed fluid flow in fractured reservoirs: An analysis of tracer-determined residence time distributions. J. Geophys. Res. Solid Earth 89, 10374–10384. https://doi.org/10.1029/JB089iB12p10374

Robinson, P., 1984. Connectivity, flow and transport in network models of fractured media, Ph.D. thesis, Oxford Univ., Oxford, U. K.

Rusciadelli, G., Viandante, M.G., Calamita, F., Cook, A.C., 2005. Burial-exhumation history of the central Apennines (Italy), from the foreland to the chain building: thermochronological and geological data. Terra Nov. 17, 560–572. https://doi.org/10.1111/j.1365-3121.2005.00649.x

Rustichelli, A., Tondi, E., Agosta, F., Cilona, A., Giorgioni, M., 2012. Development and distribution of bed-parallel compaction bands and pressure solution seams in carbonates (Bolognano Formation, Majella Mountain, Italy). J. Struct. Geol. 37, 181–199. https://doi.org/10.1016/J.JSG.2012.01.007

Rutqvist, J., Birkholzer, J., Cappa, F., Tsang, C.-F., 2007. Estimating maximum sustainable injection pressure during geological sequestration of CO2 using coupled fluid flow and geomechanical fault-slip analysis. Energy Convers. Manag. 48, 1798–1807. https://doi.org/https://doi.org/10.1016/j.enconman.2007.01.021

S. Allan, U., 1989. Model for Hydrocarbon Migration and Entrapment Within Faulted Structures. Am. Assoc. Pet. Geol. Bull. 73, 803–811.

Scheirer, D.S., Macdonald, K.C., 1995. Near-axis seamounts on the flanks of the East Pacific Rise, 8°N to 17°N. J. Geophys. Res. Solid Earth 100, 2239–2259. https://doi.org/10.1029/94JB02769

Sciasciani, V., E. Tavarnelli, and F.C., 2002. The interaction of extensional and contractional deformations in the outer zones of the Central Apennines, Italy. J. Struct. Geol 24(10), 1647–1658.

Searle, R., 1984. Gloria survey of the east pacific rise near 3.5°S: Tectonic and volcanic characteristics of a fast spreading mid-ocean rise. Tectonophysics 101, 319–344. https://doi.org/10.1016/0040-1951(84)90119-7

Shapiro, S.A., Huenges, E., Borm, G., 1997. Estimating the crust permeability from fluid-injection-induced seismic emission at the KTB site. Geophys. J. Int. 131, F15–F18. https://doi.org/10.1111/j.1365-246X.1997.tb01215.x

Shaw, A.M., Behn, M.D., Humphris, S.E., Sohn, R.A., Gregg, P.M., 2010. Deep pooling of low degree melts and volatile fluxes at the 85°E segment of the Gakkel Ridge: Evidence from olivine-hosted melt inclusions and glasses. Earth Planet. Sci. Lett. 289, 311–322. https://doi.org/10.1016/j.epsl.2009.11.018

Shen, Y., Forsyth, D.W., 1995. Geochemical constraints on initial and final depths of melting beneath mid-ocean ridges. J. Geophys. Res. Solid Earth 100, 2211–2237. https://doi.org/10.1029/94JB02768

Sibson, R.H., 1990. Conditions for fault-valve behaviour. Geol. Soc. London, Spec. Publ. 54, 15 LP-28.

SIBSON, R.H., 1977. Fault rocks and fault mechanisms. J. Geol. Soc. London. 133, 191. https://doi.org/10.1144/gsjgs.133.3.0191

Sisavath, S., et al., 2003. A simple model for deviations from the cubic law for a fracture undergoing dilation or closure. Pure Appl. Geophys 160, 1009–1022.

Smith, L., Schwartz, F.W., 1984. An Analysis of the Influence of Fracture Geometry on Mass Transport in Fractured Media. Water Resour. Res. 20, 1241–1252. https://doi.org/10.1029/WR020i009p01241

Smith, S.A.F., Di Toro, G., Kim, S., Ree, J.-H., Nielsen, S., Billi, A., Spiess, R., 2013. Coseismic recrystallization during shallow earthquake slip. Geology 41, 63–66.

Snow D.T., 1965. A parallel plate model of fractured permeable media. University of California, Berkeley.

Sparks, D.W., Parmentier, E.M., 1993. The Structure of Three-Dimensional Convection Beneath Oceanic Spreading Centres. Geophys. J. Int. 112, 81–91. https://doi.org/10.1111/j.1365-246X.1993.tb01438.x

Sparks, D.W., Parmentier, E.M., 1991. Melt extraction from the mantle beneath spreading centers. Earth Planet. Sci. Lett. 105, 368–377. https://doi.org/http://dx.doi.org/10.1016/0012-821X(91)90178-K

Sperrevik, S., Gillespie, P.A., Fisher, Q.J., Halvorsen, T., Knipe, R.J., 2002. Empirical estimation of fault rock properties. Nor. Pet. Soc. Spec. Publ. 11, 109–125. https://doi.org/10.1016/S0928-8937(02)80010-8

Spiegelman, M., 1993. Melting and melt movement in the Earth - Physics of melt extraction: theory, implications and applications. Philos. Trans. R. Soc. London. Ser. A Phys. Eng. Sci. 342, 23 LP-41.

Spiegelman, M., McKenzie, D., 1987. Simple 2-D models for melt extraction at mid-ocean ridges and island arcs. Earth Planet. Sci. Lett. 83, 137–152.

Standish, J.J., Sims, K.W.W., 2010. Young off-axis volcanism along the ultraslow-spreading Southwest Indian Ridge. Nat. Geosci. 3, 286–292. https://doi.org/10.1038/ngeo824

Svensson, U., 2001. A continuum representation of fracture networks. Part I: Method and basic test cases. J. Hydrol. 250, 170–186. https://doi.org/10.1016/S0022-1694(01)00435-8

Tadokoro, K., M. Ando, K. Sato, T. Yamada, T. Okuda, H. Katao, and K.K., 2001. Development of an observation system for ocean bottom crustal deformation by means of acoustic ranging-GPS link. J. Geogr 110, 355–361.

Talwani, P., Chen, L., Gahalaut, K., 2007. Seismogenic permeability, k_s. J. Geophys. Res. 112, B07309. https://doi.org/10.1029/2006JB004665

Tondi, E., Antonellini, M., Aydin, A., Marchegiani, L., Cello, G., 2006. The role of deformation bands, stylolites and sheared stylolites in fault development in carbonate grainstones of Majella Mountain, Italy. J. Struct. Geol. 28, 376–391. https://doi.org/10.1016/J.JSG.2005.12.001

Turcotte, D.L., Schubert, G., Turcotte, D.L., n.d. Geodynamics.

Vecsei, A., D. Sanders, D. Bernoulli, G. P. Eberli, and J.S.P., 1998. Cretaceous to Miocene sequence stratigraphy and evolution of the Maiella carbonate platform margin, Italy. Mesozoic Cenozoic Seq. Stratigr. Eur. Basins, Spec. Publ. Soc. Econ. Paleontol. Miner.

60, 53–54.

Vecsei, A., 1991. Aggradation und Progradation eines Karbonatplattform-Randes: Kreide bis Mittleres Tertiar der Montagna della Maiella, Abruzzen. Mitt. Geol. Inst. Eidg. Tech. Hochsch. Univ. Zurich 294, 169.

Vecsei, A., Sanders, D.G.., 1999. Facies analysis and sequence stratigraphy of a Miocene warm-temperate carbonate ramp, Montagna della Maiella, Italy. Sediment. Geol. 123, 103–127. https://doi.org/10.1016/S0037-0738(98)00079-7

Walsh, J.., Bailey, W.., Childs, C., Nicol, A., Bonson, C.., 2003. Formation of segmented normal faults: a 3-D perspective. J. Struct. Geol. 25, 1251–1262. https://doi.org/10.1016/S0191-8141(02)00161-X

Wang, X., Cochran, J.R., Barth, G.A., 1996. Gravity anomalies, crustal thickness, and the pattern of mantle flow at the fast spreading East Pacific Rise, 9°–10°N: Evidence for three-dimensional upwelling. J. Geophys. Res. Solid Earth 101, 17927–17940. https://doi.org/10.1029/96JB00194

Warren, J. E., & Root, P.J., 1963. The Behavior of Naturally Fractured Reservoirs. Soc. Pet. Eng.

White, R.S., 1992. Magmatism during and after continental break-up. Geol. Soc. London, Spec. Publ. 68, 1–16. https://doi.org/10.1144/GSL.SP.1992.068.01.01

Wibberley, C.A.J., Yielding, G., Di Toro, G., 2008. Recent advances in the understanding of fault zone internal structure: a review. Geol. Soc. London, Spec. Publ. 299, 5 LP-33.

Yielding, G., Freeman, B., Needham, D.T., 1997. Quantitative fault seal prediction. Am. Assoc. Pet. Geol. Bull. 81, 897–917.

Zyvoloski, G.A., Robinson, B.A., Viswanathan, H.S., 2008. Generalized dual porosity: A numerical method for representing spatially variable sub-grid scale processes. Adv. Water Resour. 31, 535–544. https://doi.org/10.1016/J.ADVWATRES.2007.11.006

Zyvoloski G. A, 2007. FEHM: A control volume finite element code for simulating subsurface multi-phase multi-fluid heat and mass transfer. Los Alamos Unclassif. Rep. LA-UR- 07-3359.